NOTICE

The quality of this microform is heavily dependent upon the quality of the original thesis submitted for microfilming. Every effort has been made to ensure the highest quality of reproduction possible.

If pages are missing, contact the university which granted the degree.

Some pages may have indistinct print especially if the original pages were typed with a poor typewriter ribbon or if the university sent us an inferior photocopy.

Reproduction in full or in part of this microform is governed by the Canadian Copyright Act, R.S.C. 1970, c. C-30, and subsequent amendments.

AVIS

La qualité de cette microforme dépend grandement de la qualité de la thèse soumise au microfilmage. Nous avons tout fait pour assurer une qualité supérieure de reproduction.

S'il manque des pages, veuillez communiquer avec l'université qui a conféré le grade.

La qualité d'impression de certaines pages peut laisser à désirer, surtout si les pages originales ont été dactylographiées à l'aide d'un ruban usé ou si l'université nous a fait parvenir une photocopie de qualité inférieure.

La reproduction, même partielle, de cette microforme est soumise à la Loi canadienne sur le droit d'auteur, SRC 1970, c. C-30, et ses amendements subséquents.

Canada

UNIVERSITY OF ALBERTA
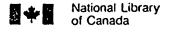
PHOTOTHERMAL CONDUCTIVITY MODULATION

BY

$\copyright$ Robert McLaren

A THESIS

SUBMITTED TO THE FACULTY OF GRADUATE STUDIES AND

RESEARCH IN PARTIAL FULFILLMENT OF THE REQUIREMENTS FOR

THE DEGREE OF

Doctor Of Philosophy

DEPARTMENT OF CHEMISTRY
EDMONTON, ALBERTA
FALL, 1991

Canada

UNIVERSITY OF ALBERTA

RELEASE FORM

NAME OF AUTHOR :   ROBERT MCLAREN

TITLE OF THESIS :   PHOTOTHERMAL CONDUCTIVITY MODULATION

DEGREE :   DOCTOR OF PHILOSOPHY

YEAR THIS DEGREE GRANTED : 1991

Permission is hereby granted to the University of Alberta Library to reproduce single copies of this thesis and to lend or sell such copies for private, scholarly or scientific research purposes.

The author reserves all other publication and other rights in association with the copyright in the thesis, and except as hereinbefore provided neither the thesis nor any substantial portion thereof may be printed or otherwise reproduced in any material form whatever without the author's prior written permission.

_____

NRC
INSTITUTE FOR ENVIRONMENTAL CHEMISTRY
OTTAWA, CANADA
K1A 0R6

July 19, 1991

UNIVERSITY OF ALBERTA

FACULTY OF GRADUATE STUDIES AND RESEARCH

The undersigned certify that they have read, and recommend to the Faculty of

Graduate Studies and Research for acceptance, a thesis entitled

PHOTOTHERMAL CONDUCTIVITY MODULATION

submitted by

Robert McLaren

in partial fulfillment of the requirements for the degree of

Doctor of Philosophy

_____
Dr. N.J. Dovichi (supervisor)

_____
Dr. B. Kratochvil

_____
Dr. G. Horlick

_____
Dr. J.E. Bertie

_____
Dr. Franck-Dept. of Physics

_____
Dr. E.P.C. Lai (external examiner)
Dept. of Chemistry
Carleton University, Ottawa.

July 15, 1991

iii

To my parents

ABSTRACT

A new photothermal method for absorptivity, thermal property and electrical property measurements of liquids and solids is described in this thesis. Photothermal Conductivity Modulation (PCM), unlike other photothermal techniques, relies on the measurement of an electrical property of the sample to probe the laser-based absorbance phenomena. Heat deposited in the sample by non-radiative relaxation of excited state species directly affects the electrical conductivity of the sample.

In solution, conductance of ions is extremely temperature sensitive, forming the basis of a sensitive method for making absorbance measurements in nanoliter volumes or less. A model was developed to describe the temporal behavior of the signal. The model was compared to experiment with respect to all variables. The best absorbance detection limit in solution was 6×10^{-6}, measured across a 76-μm path length.

PCM has been applied to the characterization of high temperature superconducting materials. The large change in resistance of a superconductor at its transition temperature generates a signal that is proportional to the differential resistivity, $d\rho/dT$. Collection of the signal as a function of beam position as the laser is scanned across the sample generates images of the resistive properties of superconducting samples. Spatially resolved measurements of the transition temperature can be made. Lead and antimony substitution in the Bi-Sr-Ca-Cu-O superconducting system was explored. Lead was found to stabilize the 2223 superconducting phase better than antimony in these materials. Transition temperatures above 110-K were not found with Sb substitution, in contrast to recent reports. PCM was used to separate the 2223 resistive transition of polycrystalline samples into two

v

components, one that is current sensitive and the other not. The current sensitivity in the low temperature component was attributed to the critical current effect for intergranular regions. Identification of regions of high current density by PCM imaging was demonstrated. Local measurements of the differential resistivity of inhomogeneous samples are also presented.

PCM imaging of a superconducting thin film, $YBa_2Cu_3O_{7-y}$, revealed inhomogeneities in the transition temperature across the film. Maximum signals are associated with cleavage lines of the substrate, where disturbance of the epitaxial structure of the film is expected to occur.

ACKNOWLEDGEMENTS

It is with mixed feelings that I have prepared this thesis. While it represents the culmination of my graduate work here at the University of Alberta, its preparation forecasts my eventual leaving of Edmonton and the many fine people with whom I have worked and become friends during my stay here. Many of these people have given me help and support during the course of my work. I would like express my gratitude to them all, in particular the following:

Norm Dovichi, my supervisor, for his help, guidance, and most of all, his never ending encouragement. His excellence in science is second only to his admirable human qualities, patience, respect and of course, humour. I no longer frown.

Chemistry faculty members with whom I have been associated, especially those who have taught me, including the members of my examining committee, Dr. B. Kratochvil, Dr. G. Horlick and Dr. J.E. Bertie, for always answering when I had a question. I am no longer ignorant.

The excellent support staff too numerous to mention, members of the electronics shop, machine shop, glass blowing shop, secretarial staff and George Braybrook of the Entomology SEM lab, for their skill and helpfulness with the apparently insurmountable problems that have arisen during the course of my work. I no longer doubt.

Dr. Peter Grant of the National Research Council in Ottawa, for supplying the superconducting thin film for Chapter 6. I am no longer ohmless.

TABLE OF CONTENTS

LIST OF FIGURES

LIST OF TABLES

LIST OF PLATES

SYMBOLS AND ABBREVIATIONS

A	- absorbance
A_η	- viscosity constant
A_f	- thermal modulation factor
A	- optical absorption length
b	- path length
B	- frequency bandwidth
B	- Beta function
C	- concentration
C_p	- heat capacity
C_{dl}	- double layer capacitance
d	- distance
D	- thermal diffusivity
e	- electron charge
E	- energy (of laser pulse)
E^o	- standard cell potential
E_{pp}	- electric field in a parallel plate capacitor
E^*	- viscous activation energy
$\vec{E}$	- electric field vector
erf	- error function
f	- modulation frequency (optical)
f	- frictional coefficient
F	- carrier frequency (electrical)
F	- Farad
I	- current
I	- intensity (optical)
I_c	- critical current
I_o	- incident intensity (corrected for losses)
ΔI_{imp}	- impulse response function
ΔI_{step}	- step response function
$\Delta I_{sw(n)}^{on}$	- square wave response function (n^{th} period, laser on)
$\Delta I_{sw(n)}^{off}$	- square wave response function (n^{th} period, laser off)

IEEE	- IEEE-488-1978 instrumentation data bus
J_c	- critical current density
k	- thermal conductivity
K	- dielectric constant of medium
K_s	- solvent constant (for TMEC)
K_w	- autoprotolysis constant of water
M	- molarity
N	- Avogadro's number
P	- power (laser)
P_o	- incident power
$P(t)$	- optical excitation function
PCM	- photothermal conductivity modulation
q	- charge
Q	- reaction quotient
r	- electrode radius
r	- reflectance
r_i	- radius of ionic species
rms	- root mean square
R	- resistance
R	- molar gas constant
R	- ratio of electrode radius to electrode separation (r/L)
R_{el}	- electrolytic resistance
$R(t)$	- response function
t	- time
t_c	- time constant (solution or electrical)
T	- absolute temperature
T	- transmission
T_c	- transition temperature (of a superconductor)
TMEC	- thermal modulation of electrical conductivity
TEM_{oo}	- guassian mode of a laser beam
vol	- volume (of electrolytic resistor)
V	- voltage
x,y,z	- spatial coordinates, z is laser beam axis
z_c	- confocal distance (of a laser beam)
z_i	- ionic charge number
Z	- error function parameter (Eq. 3.13)

β	- absorption coefficient
β	- fractional distance between electrodes
χ	- magnetic susceptibility
ε	- molar absorptivity
ε_0	- permittivity of free space
η	- viscosity
η_0	- static thermal healing length
η_ω	- dynamic thermal healing length (thermal diffusion length)
ϕ	- fluidity
Φ	- degenerate hypergeometric function
κ	- hypergeometric function parameter (Eq. 3.13)
λ	- wavelength of light
ν	- volume between inner leads in four probe arrangement.
ω	- spot size of laser
ω	- angular frequency
ω_0	- spot size at the beam waist
Ω	- ohms (resistance)
ρ	- density
ρ	- resistivity
σ	- surface charge density
σ	- standard deviation (noise)
σ^2	- variance
τ	- volume element (for integration)
τ	- time in half a chopping period

CHAPTER 1

INTRODUCTION

"And the atoms that compose this radiance do not travel as isolated individuals but linked and massed together"

— 'De Rerum Naturae', Lucretius

1.1 INTRODUCTION

The laser has become a very common optical source in the laboratory since its first demonstration by Theodore H. Maiman in 1960 [1]. Since that first emission of coherent radiation from a ruby rod, the laser has found many applications in chemistry and physics [2]. Most of these applications utilize the unique properties of laser radiation: high radiance, spectral purity, high directionality, and coherence [3,4].

For example, because of its high radiance and spectral purity, the laser has all but replaced the mercury arc source in Raman spectroscopy, making this method more feasible in a variety of chemical applications. The high radiance and spectral purity properties of the laser are also pivotal for the "laser cooling" of atoms and ions to sub-millikelvin temperatures [5,6]. Cooling of these species allows high resolution spectroscopic measurements to be made. Temporal coherence has allowed the generation of ultrafast femtosecond laser pulses, which can follow the reactions of small chemical intermediates and probe the properties of semiconductors [7-9]. Furthermore, the high directionality of the laser, a direct result of coherence and the laser cavity design, is exploited in remote sensing techniques such as LIDAR (LIght Detection And Ranging) and DIAL (DIfferential Absorption Lidar). These techniques are being used to map changes in the polar ozone holes [10], and to give spatially resolved measurements of atmospheric pollutants [11,12].

Other applications of laser radiation rely on its spatial coherence. This property stems from the process of stimulated emission that occurs in the laser cavity. Einstein first proposed this process in which one photon "tickles" an excited state species, causing the transition to a lower energy

level. This transition causes simultaneous emission of a second photon of identical frequency, phase and direction. With amplification, the resulting laser radiation consists of identical photons that appear to originate from a point source. This spatial coherence of the radiation allows the beam to be focused to very small spot sizes; $\lambda/2$ is the limit for this spot size.

The ability to focus a beam to very small dimensions without significant losses makes the laser an attractive source for a wealth of other applications. The high irradiance produced in a focused beam can result in nonlinear optical phenomena with sufficient efficiency to compete with linear phenomena. With pulsed lasers, the peak irradiance also can be sufficient to surpass the damage threshold of a material. With more intensity, laser ablation can be used to vaporize small amounts of solid samples. The laser intensity can be varied to control the amount of excitation and ionization in the resulting plume, which can be further analyzed by a subsequent process.

An excellent example to illustrate these ideas is the highly selective technique, pulsed laser desorption in supersonic beam mass spectroscopy with resonant two-photon ionization [13,14]. In this technique, the high irradiance of a pulsed laser ablates a small amount of solid sample with the production of mainly neutral parent molecules in the plume. A supersonic jet produces a very cold molecular beam that carries the molecules to the ionization region. The high irradiance of a second pulsed tunable dye laser, suitably delayed, performs selective two-photon ionization of the molecules, which are then mass analyzed.

A focused laser beam is useful not only for its high irradiance, but also for the very small volumes and surface areas that it can probe. This high spatial resolution analysis can be done with relative ease because of the high directionality of the laser. Two 1-inch mirrors with two angular degrees of freedom each, a microscope objective and a translation stage are all that are required to focus ~87% of the laser's power to a 1-μm spot anywhere on an optical table. The laser is thus an ideal tool for microanalysis [15] and is used as a source for numerous nondestructive methods of analysis. Among these, and of particular interest in this thesis, is a class of methods based upon photothermal phenomena, for analysis in gases, liquids and solids [16,17].

This thesis presents a new photothermal technique for non-destructive analysis, Photothermal Conductivity Modulation (PCM). In solution, this method was originally named Thermal Modulation of Electrical Conductivity (TMEC). In Chapter 2, sensitive absorbance measurements in solution by TMEC are discussed. In Chapter 3, development of a theoretical model and a more detailed characterization of TMEC for solution absorbance measurements is given. In Chapter 4, differential resistivity measurement and imaging of bulk polycrystalline high-temperature superconducting samples are discussed. Measurements on $Bi_2Sr_2Ca_2Cu_3O_x$ high-Tc superconductors with Pb and Sb substitution are discussed in Chapter 5. Finally, this method is applied to the imaging of a thin film superconductor, $YBa_2Cu_3O_{7-x}$ in Chapter 6. Conclusions are given in Chapter 7.

1.2 PHOTOTHERMAL METHODS

To understand photothermal methods, it is necessary to have a basic understanding of the photophysical excitation and relaxation processes of
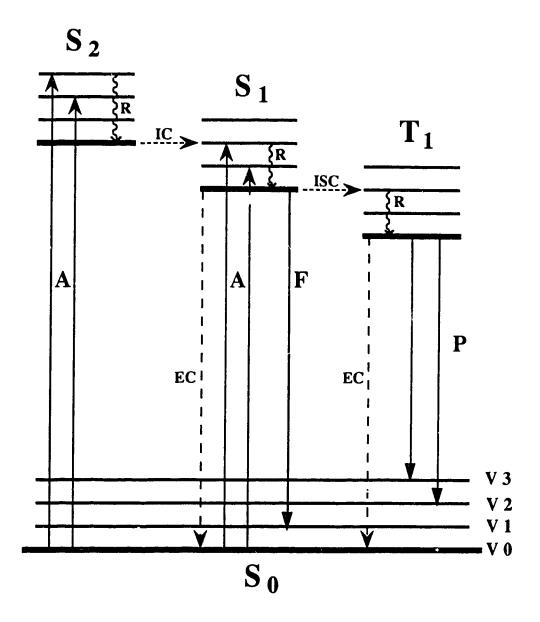
Figure 1.1   Jablonski energy level diagram for a generic molecule.

A   - absorbance   IC   - internal conversion

F   - fluorescence   ISC   - intersystem crossing

P   - phosphorescence   EC   - external conversion

                                 R   - vibrational relaxation

molecular species. The Jablonski energy diagram of Figure 1.1 illustrates these processes for a generic molecule with a ground electronic state, S_0, two singlet excited states, S_1 and S_2, and a triplet excited state, T_1. Each electronic state has vibrational levels associated with it.

Excitation to an excited singlet state ($S_0 \rightarrow S_1, S_2$. . .) can occur via optical absorption by the molecule. The absorbance process is measured indirectly in conventional absorbance spectrometry by monitoring the attenuation of a beam through the sample. In the excited state, the molecule rapidly undergoes vibrational relaxation to the lowest vibrational level of the state. This vibrational energy is lost to thermal or vibrational motion of the molecules in the surrounding medium. From higher electronic states, non-radiative internal conversion occurs for all but a few molecular species. In this process, a nonradiative transition from the lower vibrational level of the upper electronic state to an upper vibrational level of a lower electronic state occurs. Vibrational relaxation in this lower state occurs very quickly. Internal conversion and vibrational relaxation are very efficient processes. In solution, the molecule usually converts to the lowest vibrational level of the first excited singlet state very rapidly, 10^{-11} to 10^{-10} seconds, regardless of the initial transition. All excess energy is lost to the surroundings as heat.

The molecule can relax from the first singlet state in one of three ways. In fluorescence, the transition to the ground state ($S_1 \rightarrow S_0$) occurs with emission of a photon. Since the emission of this photon follows directly from the initial absorbance of a photon, fluorescence can give an indirect measure of the absorption of a sample. The advantages of fluorescence detection have been well documented [18]. Indeed, the sensitivity of fluorimetry is difficult to surpass. Single atom and single molecule detection

have already been achieved in gases and liquids respectively [19-21]. A second radiative method of relaxation is via phosphorescence. This process requires an initial intersystem crossing $(S_1 \rightarrow T_1)$ followed by vibrational relaxation. The phosphorescence transition $(T_1 \rightarrow S_0)$, being spin forbidden, has a long lifetime $(10^{-4} \rightarrow 10^4$ seconds) and is less common than fluorescence.

The third and most common method of relaxation is via external conversion. This is a radiationless process in which the molecule makes the transition to the ground state by giving up its excess energy to surrounding molecules during collisions. This energy eventually takes the form of heat as the surroundings come to equilibrium.

Photothermal methods, often termed calorimetric methods, are concerned with the measurement of heat that is produced by radiationless processes, vibrational relaxation and external conversion. Because these processes are more common than relaxation by luminescence, photothermal phenomena, in principle, can provide more universal methods of detection. The emission of heat by the molecule via a radiationless route must follow from initial absorption of a photon. Thus photothermal methods, like fluorescence and phosphorescence, can be used for the measurement of absorbance.

Various methods can be used to measure the emission of heat in the sample. These can be classified into direct methods, which attempt to measure the heat directly, and indirect methods, which measure some property of the sample that changes with temperature. Table 1.1 lists various photothermal methods and the principle of the measurement.

Table 1.1   Photothermal methods

Method	Description	Ref.
Photoacoustic Spectroscopy (Optoacoustic, Thermoacoustic)	the thermally induced change in density of the sample results in acoustic wave generation either in the sample or the surrounding medium, which are detected with a microphone or a piezoelectric transducer.	22-24
Thermo-optical Spectroscopies	the thermally induced change in refractive index of the sample or surrounding medium is probed with a second laser.	25,26
Photothermal Radiometry	laser induced heating is detected with infrared detectors or cameras.	27,28
Other direct calorimetric methods	the photothermal heating is monitored with a pyroelectric calorimeter, a resistance thermometer or a thermocouple.	29-32
Photothermal Conductivity Modulation	thermally induced electrical conductivity (or resistance) changes are monitored by direct conductance or resistance measurements of the sample.	33-35
Photoinductive imaging	thermally induced resistance changes are detected by the change in the impedance of an eddy current coil detector.	36
Photothermal STM	absorption measurements of nm resolution are made by monitoring the STM signal in the area of a laser modulated region of sample the sample material and detector tip, being composed of different materials, behave as a thermocouple.	37

Despite the many methods of detection, all photothermal techniques have some features in common. The temperature change associated with non-radiative relaxation is usually very small (μK to 1-K) compared to the ambient temperature. For this reason, pulsed or modulated optical sources are used almost exclusively to allow noise reduction techniques such as averaging or phase sensitive detection to be employed. With modulated or pulsed excitation, the heat source in the sample is transient. For pulsed lasers, analysis of the signal is made in the time domain. For cw lasers, modulation at a single frequency allows frequency domain analysis, while multifrequency modulation (FM) allows both time and frequency domain analysis [38].

The sample can be characterized by the wavelength dependent optical absorption coefficient, β (λ), which determines the rate of attenuation of the optical beam intensity, I, through the sample.

$$I = I_o\, e^{-\beta b} \tag{1.1}$$

I_o is the incident intensity and b is the path length through the sample. The optical absorption length, A (λ), is simply the inverse of the optical coefficient,

$$A\ (\lambda) = \frac{1}{\beta(\lambda)} \tag{1.2}$$

It represents the distance at which the intensity through the sample is attenuated by a factor of e^{-1}. This distance can be tens of nanometers in solids, hundreds of meters in transparent liquids and kilometers in optical fibers. The heat generated in the sample from absorption diffuses to regions of lower temperature. For modulated sources, the periodic thermal waves that are
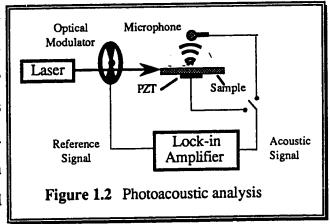
' generated have a characteristic distance over which their effects can be felt, η_ω, the thermal diffusion length (or dynamic thermal healing length),

$$\eta_\omega = \sqrt{\frac{D}{\pi f}} \qquad\qquad (1.3)$$

where D is the thermal diffusivity of the material and f is the modulation frequency. The thermal waves are damped by a factor of e^{-1} at a distance η_ω from the thermal source. The detector must either be placed within one thermal diffusion length of the laser source spot or one must rely on another physical phenomena to transport the signal to the detector. An acoustic wave accomplishes this task in photoacoustic spectroscopy. In all photothermal methods, the measured signal depends both on the generation and transport of heat near the excitation source. For this reason, these methods can, in principle, provide information about the absorptivity, β, and thermal diffusivity, D, of the sample material.

Figure 1.2 Photoacoustic analysis
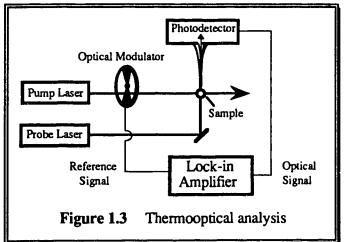
The most well developed photothermal methods are photoacoustic spectroscopy [22-24] and thermooptical spectroscopies [25,26]. In photoacoustic spectroscopy, Figure 1.2, a beam incident on, or through, the sample causes thermal expansion of the material. This periodic expansion and contraction generates an acoustic wave that can travel through the sample or the surrounding medium to the acoustic transducer. Either a piezoelectric transducer, coupled directly to the sample, or a microphone is utilized for detection of the acoustic wave. Photoacoustic spectroscopy can be used for the

study of the absorbance or thermal properties of gaseous [16], liquid [22], solid and thin film samples [17], both opaque and transparent. Depth profiling, the measurement of features below the surface that may not be optically visible, can be done in the frequency domain or the time domain [39].

Thermooptical spectrometries [25,26] use a probe laser to measure the thermal perturbation induced by absorption of a pump laser. The laser is a desirable probe tool in these methods since it can interact with the heated region within the critical distance of one thermal diffusion length, . . . often only a few micrometers. The measured phenomenon is a refractive index (RI) gradient that results from the change in RI with temperature. The refractive index gradient can act as a lens that: defocuses [40,41], deflects [42], or refracts [43] the probe beam in thermal lens, photothermal deflection, and mirage techniques respectively.

Figure 1.3 Thermooptical analysis

The refractive index change induced by heating also causes a change in optical path length that can be measured using interferometric methods [44,45]. The strength of the thermal lens and the change in optical path length is proportional to the heat deposited in the medium, which in turn is proportional to the absorptivity of the sample. Thus, thermooptical methods can be used to measure the absorbance of highly transparent liquids.

In some thermooptical methods, one laser accomplishes both production and probing of the refractive index gradient. More commonly, a second probe beam of lower intensity is used for this purpose, as shown in

Figure 1.3. Some photothermal methods exist that contain properties of both photoacoustic and thermooptical techniques. A beam deflection technique that depends on heat induced surface buckling has been applied to the study of solids [46]. In this technique, a pump laser focused on the sample heats a region on the surface. Thermal expansion of the material causes the surface to expand and buckle at that point. A probe laser is focused onto the surface at the same point and the reflection off the surface is monitored with a photodetector. The absorptivity of the material determines the degree of surface buckling and thus affects the amount of beam deflection from the surface.

The other photothermal methods listed in Table 1.1 are not as well developed but deserve some attention in the future. The direct photothermal methods include photothermal radiometry [27,28], which uses infrared imaging of the sample, and those methods that employ a thermal transducer for temperature measurement [29-32]. A rather new and intriguing technique is photothermal scanning tunneling microscopy (STM), which is capable of making absorbance measurements with atomic scale resolution [37]. This method is based upon conventional STM but with the addition of a modulated pump laser that illuminates the thermally thin sample from below. The sample and STM 'tip' are in contact only through their electron orbital overlap. Since the tip and sample are made of different materials, the overlap behaves as a thermocouple. The periodic heating from absorption by the sample induces an ac component on the STM current signal. The amplitude of the modulation gives a measure of the absorbance of the sample.

Photothermal conductivity modulation, the topic of this thesis, is an indirect photothermal method. In this method, a pump beam excites the sample while its conductivity is 'probed' with ac or dc current. The conductivity is probed by two-electrode conductance measurements in solution, or by four probe resistance measurements on solids. The electrical probes are the detector for this method. PCM is unlike thermooptical methods, where detection within a distance η_ω is necessary, or photoacoustic spectroscopy, which relies on acoustic waves for information transmission. Instead, electrical waves efficiently carry information from the excitation region to the detector. The signal represents the properties of the material within one thermal diffusion length of the excitation beam even though detection occurs at a distance that is orders of magnitude larger than η_ω. Like other photothermal methods, absorptivity and thermal diffusivity can be measured, as will be demonstrated in this thesis. In addition, information on the electrical properties of the sample can be measured because of the nature of the measurement.

Recently, another photothermal method that relies on a change in sample conductivity with temperature has been published, photoinductive imaging [36]. In this technique, eddy-current detection of the laser induced thermal waves is done with the use of a printed circuit board sensor, which hovers above the solid sample surface. The sensor consists of two differential eddy current coils, fabricated on the sensor board. A hole in the board, at the center of one coil, allows the focused beam to impinge on the surface below. The change in conductivity of the sample produces a change in the impedance of the coil. Demodulation of the differential impedance signal gives the photoinductive signal. This method has been demonstrated for

absorbance imaging on metal films and defect detection in metal alloys. The method has not yet been applied to measurements on superconductors.

1.3 SUPERCONDUCTIVITY

Superconductivity was discovered in 1911 by Heike Kamerlingh Onnes, a Dutch physicist, while making resistance measurements on mercury metal at liquid helium temperatures. At 4.2K, the resistance of the Hg wire suddenly dropped to zero, prompting Onnes to write [47],

> " The experiment left no doubt about the disappearance of the resistance of mercury. Mercury has passed into a new state, which because of its extraordinary electrical properties may be called the superconductive state."

Since that initial discovery, twenty six elements have been found to be superconducting [48], as well as numerous alloys.

Three properties of the superconductive state can be given. The first property is the absence of a measurable DC electrical resistance. Currents can be established in superconducting loops which do not decay over a period of years. Second, a superconductor can behave as a perfect diamagnet. It does not allow a magnetic field to uniformly penetrate its interior, providing that the field is not too large. In the presence of a magnetic field, screening currents are set up on the surface of the material that create an equal but opposite magnetic field, resulting in a net field of zero inside. Third, there is an energy gap of width 2Δ in the electron energy levels centered about the Fermi energy.

Several critical limits exist for the superconductive state: T_c, the critical temperature (or transition temperature); H_c (T), the critical magnetic field and J_c (T), the critical current density. Above these limits, superconductivity is

lost and the sample reverts to its normal state. The critical temperature is important for applications of superconductors. It dictates the type of cooling that is necessary to keep a material in the superconductive state. Just as important is the critical magnetic field, since common uses of these materials require exposure to large fields. In this respect, superconductors are classified into two types. For Type I superconductors, there is no penetration of magnetic flux in the sample for an applied field $H<H_c$. Above H_c, the whole sample reverts to the normal state. For Type II superconductors, two critical fields exist, H_{c1} and H_{c2}. A type II superconductor behaves as a type I superconductor for $H<H_{c1}$; no magnetic flux penetration occurs. Above H_{c2}, the total sample reverts to the normal state. But for $H_{c1}<H<H_{c2}$, a mixed state exists in which some regions are superconducting and some are not. Partial magnetic flux penetration occurs in the form of thin filaments. Around each filament is a vortex of screening current. Each vortex encloses one magnetic flux quantum, or fluxoid, Φ_0.

$$\Phi_0 = \frac{hc}{2e} = 2.069 \times 10^{-7} \text{ gauss-cm}^{-2} \tag{1.4}$$

Type II superconductors can have much higher critical field limits, $>10^5$ gauss, because of their ability to allow magnetic flux penetration. Critical fields are temperature dependent, falling to zero at the transition temperature of the material.

Critical currents are related to critical fields simply through the association of a magnetic field with a current. As the current through a material is increased, so does the magnetic field, until such point that the critical field is reached and the superconductive state is destroyed. For

practical applications, critical current densities of greater than 10^5 A/cm^2 are usually required.

The theory of superconductivity was not developed until almost 50 years after the initial discovery. The microscopic theory of superconductivity was presented by Bardeen, Cooper and Schrieffer in 1957 [49], for which they won the Nobel Prize. Their theory is generally refered to as the BCS theory. Superconductivity requires a net attraction between electrons. While the electrostatic force between electrons is repulsive, the ionic motion of a phonon in association with the electron movement can result in a net attraction of electrons that have a small energy separation. 'Cooper pairs' are formed as a result of this electron-phonon interaction. The Cooper pairs that form condense into a single state. The coherent movement of the electrons form a macroscopic quantum state in which current can flow through the crystal lattice without dissipation.

1.4 HIGH TEMPERATURE SUPERCONDUCTIVITY

The beginning of the age of high temperature superconductivity began in 1986 with a report of possible high-Tc superconductivity in the Ba-La-Cu-O system by Bednorz and Müller [50]. Onsets of superconductivity at temperatures greater than 30K were reported, higher than the previous record of T_c=23.3K for Nb$_3$Ge. Chu et al. increased the onset temperature of superconductivity to 52K in this system by applying hydrostatic pressure [51].

Early in 1987, Wu et al. reported superconductivity at 93K in the Y-Ba-Cu-O system [52]. This superconductor, now known as YBa$_2$Cu$_3$O$_{7-y}$, or 123, is the most best characterized of the new high-T_c superconductors. It has an orthorhombic structure with two nonequivalent Cu positions [53]. One of

the Cu positions forms CuO chains while the other forms CuO_2 layers, the latter of which are believed to be critical for superconductivity. The rare earth, Y, is not essential for superconductivity. Various substitutions for this element have been reported that yield transition temperatures above 77K [54-57]. Many unsubstantiated claims of superconductivity at 155K, 160K, and 240K were reported in this system in 1987 [58-60]. The $YBa_2Cu_3O_{7-y}$ material is oxygen sensitive; reversible loss of oxygen by heat treatment forms the insulator, $YBa_2Cu_3O_6$. This material is also sensitive to moisture in the atmosphere, which will necessitate protection of some sort for future applications [61,62].

In 1988, Maeda et al discovered superconductivity above 100-K in the Bi-Sr-Ca-Cu-O system [63]. Superconductivity was also found in the related Tl-Ba-Ca-Cu-O system [64]. The two systems can be represented by the general formula $A_mB_2Ca_{n-1}Cu_nO_{m+2n+2}$, with A= Bi or Tl, B= Sr or Ba, m= 1 or 2 and n=1,2,3,4. The transition temperature is seen to increase with the number of CuO_2 sheets in the crystal structure [65], which are crucial to superconductivity just as with the 123 superconductor. The highest transition temperature to date is 125K in the Tl-Ba system [66] and 110K in the Bi-Sr system [63].

Because of the toxicity of Tl, the Bi-Sr system has received slightly more attention than the Tl-Ba system. The 110-K phase (2223 phase) of the Bi-Sr-Ca-Cu-O system, being the highest nontoxic transition temperature superconductor has received much attention. This phase was somewhat difficult to prepare in a pure form. It has been found that Pb substitution for Bi stabilizes this phase in bulk samples [67-69].

REFERENCES

(1)   T.H. Maiman, R.H. Hoskins, I.J. D'Haenens, C.K. Asawa and V. Evtuhov, *Phys. Rev.* **123**, 1151 (1961).

(2)   D.L. Andrews, *"Lasers in Chemistry"*, second edition, Springer-Verlag, Berlin (1990).

(3)   J.D. Ingle and S.R. Crouch, *"Spectrochemical Analysis"* , Prentice-Hall, New Jersey (1988).

(4)   *"Optics Guide 4"* , Melles Griot (1988).

(5)   D.J. Wineland and W.M. Itano, *Physics Today* **40**, 34 (1987).

(6)   C.N. Cohen-Tannoudji and W.D. Phillips, *Physics Today* **43**, 33 (1990).

(7)   A.H. Zewail, R.B. Bernstein, *Chem. & Eng. News* **66**, 24 (1988).

(8)   P.A. Hackett, *Can. Chem. News.* **40**, 9 (1988).

(9)   D.H. Auston, *Physics Today* **43**, 46 (1990).

(10) R.N. Dubinsky, *Lasers and Optronics* **8**, 45 (1989).

(11) C.T. Troy, *Photonics Spectra* **21** , 66 (1987).

(12) H. Edner, K. Fredriksson, A. Sunesson, S. Svanberg, L. Unéus, and W. Wendt, *Appl. Opt.* **26**, 4330 (1987).

(13) J. Grotemeyer, U. Boesl, K. Walter and E.W. Schlag, *Org. Mass. Spectr.* **21**, 645 (1986).

(14) B. Tembreull and D.M. Lubman, *Anal. Chem.* **58**, 1299 (1986).

(15) N.J. Dovichi, *Rev. Sci. Instrum.* **61**, 3653 (1990).

(16) P. Hess, Ed., *"Photoacoustic, Photothermal and Photochemical Processes in Gases"*, Topics in Current Physics **46**, Springer-Verlag, Berlin (1989).

(17) P. Hess, Ed., *"Photoacoustic, Photothermal and Photochemical Processes at Surfaces and in Thin Films"*, Topics in Current Physics **47**, Springer-Verlag, Berlin (1989).

(18) E.S Yeung and M.J. Sepaniak, *Anal. Chem.* **52**, 1465A (1987).

(19) C.L. Pan, J.V. Prodan, W.M. Fairbank and C.Y. She, *Opt. Lett.* **5**, 459 (1980).

(20) D.C. Nguyen, R.A. Keller, J.H. Jett and J.C. Martin, *Anal. Chem.* **59**, 2158 (1987).

(21) E.B. Shera, N.K. Seitzinger, L.M. Davis, R.A. Keller and S.A. Soper, *Chem. Phys. Lett.* **174**, 553 (1990).

(22) D. Betteridge and P.J. Meylor, *CRC Crit. Rev. Anal. Chem.* **14**, 267 (1984).

(23) E.P.C. Lai, B.L. Chan, M. Hadjmohammadi, *Appl. Spect. Rev.* **21**, 179 (1985).

(24) A.C. Tam, *Rev. Mod. Phys.* **58**, 381 (1986).

(25) N.J. Dovichi, *CRC Crit. Rev. Anal. Chem.* **17**, 357 (1987).

(26) N.J. Dovichi, *Prog. Analyt. Spectrosc.* **11**, 179 (1988).

(27) A.C. Tam in *"Photoacoustic, Photothermal and Photochemical Processes at Surfaces and in Thin Films"*, P. Hess, Ed.,Springer-Verlag, Berlin (1989) pg. 157.

(28) Y.Q. Wang, P.K. Kuo, L.D. Favro, and R.L. Thomas in *"Photoacoustic and Photothermal Phenomena II"*, J.C. Murphy (Ed.), Springer-Verlag, Berlin (1990) pg. 24.

(29) J. H. Coufal, R.K. Grygier, D.E. Horne, J.E. Fromm, *J. Vac. Sci. Technol. A.* **5**, 2875 (1987).

(30) R. Zenobi, J.H. Hahn, R.N. Zare, *Chem. Phys. Lett.* **150**, 361 (1988).

(31) G.C. Brilmyer and A.J. Bard, *Anal. Chem.* **52**, 685 (1980).

(32) K. Tanaka, R. Satoh, and A. Odajima, *Jpn. J. Appl. Phys.* **22**, 592 (1983).

(33) R. McLaren and N.J. Dovichi, *Anal. Chem.* **60**, 730 (1988).

(34) R. McLaren and N.J. Dovichi, *Can. J. Chem.* **67**, 1178 (1989).

(35) R. McLaren and N.J. Dovichi, *J. Appl. Phys.* **68**, 4882 (1990).

(36) J.C. Moulder, D.N. Rose, D.C. Bryk, and J.S. Siwicki, in *"Photoacoustic and Photothermal Phenomena II"*, J.C. Murphy (Ed.), Springer-Verlag, Berlin (1990) pg. 91.

(37) J.M.R. Weaver, L.M. Walpita, H.K. Wickramasinghe, *Nature* **342**, 783 (1989).

(38) A. Mandelis in *"Photoacoustic, Photothermal and Photochemical Processes at Surfaces and in Thin Films"*, P. Hess, Ed.,Springer-Verlag, Berlin (1989) pg. 211.

(39) I.P. Vickery, *Prog. Analyt. Spectrosc.* **11**, 1 (1988).

(40) C. Hu, J.R. Whinnery, *Appl. Opt.* **12**, 72 (1973).

(41) T.G. Nolan, W.A. Weimer, N.J. Dovichi, *Anal. Chem.* **56**, 1704 (1984).

(42) W.B. Jackson, N.M. Amer, A.C. Bocarra, D. Fournier, *Appl. Opt.* **20**, 1333 (1981).

(43) A.C. Bocarra, D. Fournier, and J. Bodaz, *Appl. Phys. Lett.* **36**, 136 (1980).

(44) J. Stone, *J. Opt. Soc. Am.* **62**, 327 (1972).

(45) S.D. Woodruff and E.S. Yeung, *Anal. Chem.* **54**, 1174 (1982).

(46) M.A. Olmstead, N.M. Amer, S. Kohn, D. Fournier, and A.C. Boccara, *Appl. Phys. A.* **32**, 141 (1983).

(47) taken from V.D. Hunt, *"Superconductivity Sourcebook"*, John Wiley and Sons Inc., New York (1989).

(48) N.W. Ashcroft and N.D. Mermin, *"Solid State Physics"*, Saunders College, Philadelphia, (1976).

(49) J. Bardeen, L.N. Cooper and J.R. Schreiffer, *Phys. Rev. B.* **108**, 1175 (1957).

(50) J.G. Bednorz and K.A. Müller, *Z. Phys. B.* **64**,189 (1986).

(51) C.W. Chu, P.H. Hor, R.L. Meng, L. Gao and Z.J. Huang, *Science* **235**, 567 (1987).

(52) M.K. Wu, J.R. Ashburn, C.J. Torng, P.H. Hor, R.L. Meng, L. Gao and Z.J. Huang, Y. Q. Wang and C.W. Chu, *Phys. Rev. Lett.* **58**, 908 (1987).

(53) K. Schwarz, *Mikrochim. Acta.* **2**, 149 (1990).

(54) D.W. Murphy, S. Sunshine, R.B. van Dover, R.J. Cava, B. Batlogg, S.M. Zahurak and L.F. Schneemeyer, *Phys. Rev. Lett.* **58**, 1888 (1987).

(55) P.H. Hor, R.L. Meng, Y. Q. Wang, L. Gao, Z.J. Huang, J. Bechtold, K.Forster and C.W. Chu, *Phys. Rev. Lett.* **58**, 1891 (1987).

(56) J.P. Franck, J. Jung and M.A.-K. Mohamed, *Phys. Rev. B* **36**, 2308 (1987).

(57) J. Jung, J.P. Franck, W.A. Miner and M.A.-K. Mohamed, *Phys. Rev. B* **37**, 7510 (1988).

(58) S.R. Ovshinsky, R.T. Young, D.D. Allred, G. DeMaggio and G.A. Van der Leeden, *Phys. Rev. Lett.* **58**, 2579 (1987).

(59) X. Cai, R. Joynt and D.C. Larbalestier, *Phys. Rev. Lett.* **58**, 2798 (1987).

(60) J.T. Chen, L.E. Wenger, C.J. McEwan and E.M. Logothetis, *Phys. Rev. Lett.* **58**, 1972 (1987).

(61) N.P. Bansal and A.L. Sandkuhl, *Appl. Phys. Lett.* **52**, 323 (1988).

(62) N. Naito, J. Kafalas, L. Jachim and M. Downey, *J. Appl. Phys.* **67**, 3521 (1990).

(63) H. Maeda, Y. Yoshiaki, M. Fukutomi, and T. Asano, *Jpn. J. Appl. Phys.* **27**, L209 (1988).

(64) M.A. Subramanian, C.C. Torardi, J. Gopalakrishnan, P.L. Gai, J.C. Calabrese, T.R. Askew, R.B. Flippen and A.W. Sleight, *Science* **242**, 249 (1988).

(65) P. Haldar, K. Chen, B. Maheswaran, A. Roig-Janicki, N.K. Jaggi, R.S. Markiewicz and B.C. Giessen, *Science* **241**, 1198 (1988).

(66) S.S.P. Parkin, V.Y. Lee, A.I. Nazal, R. Savoy, T.C. Huang, G. Gorman, R. Beyers, *Phys. Rev. B.* **38**, 6531 (1988).

(67) S.M. Green, C. Jiang, Y. Mei, H.L. Luo, and C. Politis, *Phys. Rev. B.* **38**, 5016 (1988).

(68) H.K. Liu, S.X. Dou, N. Savvides, J.P. Zhou, N.X. Tan, A.J. Bourdillon, M. Kviz and C.C. Sorrell, *Physica C* **157**, 93 (1989).

(69) M. Pissas, D. Niarchos, C. Christides and M. Anagnostou, *Supercond. Sci. Technol.* **3**, 128 (1990).

CHAPTER 2

ABSORBANCE MEASUREMENTS

BY LASER-INDUCED

THERMAL MODULATION OF

ELECTRICAL CONDUCTIVITY

" Do not bodies and light act mutually upon one another; that is to say, bodies upon light in emitting, reflecting, refracting and inflecting it, and light upon bodies for heating them, and putting their parts into a vibrating motion wherein heat consists?"

— Isaac Newton, *'Opticks'*, (1730)

2.1 INTRODUCTION[*]

The determination of absorbance has remained a very powerful and important technique in qualitative and quantitative analysis. Spectral variations in absorbance are used to infer the structure of the analyte and Beer's law is used to relate absorbance with analyte concentration. Conventionally, absorbance (A) is determined from the transmission (T) of a sample,

$$A = \varepsilon bC = -\log T = \log \frac{P_0}{P}$$

(2.1)

where ε is the molar absorptivity of the sample, b is path length, C is analyte concentration, P_0 is the incident light power and P is the transmitted light power. For very weakly absorbing analyte, Beer's law may be approximated with a power series expansion,

$$A = \frac{P_0/P - 1}{2.303} = \frac{\Delta P}{2.303P}$$

(2.2)

where $\Delta P = P_0 - P$ is the measured difference between the incident and transmitted light power. Equation 2.2 shows that for weak solutions, the absorbance determination depends on the measurement and subtraction of two large signals. The detection limit is thus ultimately limited by the noise in the measurement source. This represents a situation where a very high background limits the analytical determination. This knowledge alone has been a motivating factor in the search for alternate methods of absorbance measurement where the background is eliminated.

To improve absorbance detection limits, it is advantageous to detect signals associated with photophysical processes that occur after absorbance. The best known method in this respect is, of course, laser induced fluorescence. The state-of-the-art detection limit for fluorescence, 8.9×10^{-14}M rhodamine-6G in a 30-μm diameter sample stream [1], corresponds to an absorbance detection limit of 1.7×10^{-11} across the stream diameter. The improvement in absorbance detection limit using fluorescence measurements is a direct consequence of the elimination of the noise associated with the excitation beam; fluorescence measurements are made in the dark. The best analogy that demonstrates this improved detection by elimination of light noise is the observation that most amateur astronomers prefer to work at night; the stars are more easily observed in the absence of sunlight. Unfortunately, fluorescence is of limited utility since few molecules possess significant quantum yield of fluorescence [2].

To improve absorbance detection limits for molecules with insignificant quantum yield, it is possible to make an indirect absorbance measurement in another way; one can detect the temperature rise associated with the nonradiative relaxation of optically excited analyte molecules. A class of high sensitivity absorbance techniques has been developed based upon measurement of this temperature rise. Most of these techniques rely on some property of the solvent having a measurable temperature coefficient. Examples of such techniques include photoacoustic spectroscopy [3], which depends on a change in density of the solvent with temperature, and thermooptical methods, which rely on a change in refractive index with temperature [4].

Inspection of a table of physical properties of solvents reveals many properties that change with temperature. For example, the surface tension, sound velocity and dielectric constant of many liquids have temperature coefficients ranging from one to five parts per thousand per degree Kelvin at room temperature [5]. Viscosity is very temperature sensitive with relative changes of 1 to 3% per Kelvin for a range of solvents. Water has a temperature coefficient of viscosity of 2.5% per Kelvin at room temperature, almost three orders of magnitude higher than the temperature coefficient of refractive index.

At first glance, thermal measurements of viscosity would appear to be a formidable challenge. Viscosity is conventionally measured by the flow rate through a calibrated tube, by a concentric tube viscometer, or by the velocity of a falling dense sphere through the liquid [6]. Yet, viscosity also is related to several physical properties of solutions. In particular, the electrical conductivity of a solution is proportional to the velocity at which ions migrate under the influence of the force from an electric field. In turn, this velocity is inversely proportional to the viscosity of the solution. Therefore, the thermal coefficient of electrical conductivity is equivalent to the thermal coefficient of viscosity. Thermal modulations of electrical conductivity, induced by the optical absorbance of an analyte in solution, can be used as an indirect and sensitive measurement of absorbance.

In this chapter, a preliminary report is given that describes measurements of absorbance by laser-induced thermal modulation of electrical conductivity (TMEC). The principle of the measurement is simple. A chopped laser beam illuminates the volume of liquid between two small

electrodes that are used to measure the conductivity of the solution. When the laser is on, absorbance by analyte molecules causes a temperature increase between the electrodes. The viscosity of the solution decreases, ions move faster and the current through the solution increases. The reverse happens during the off portion of the chopping cycle; the solution between the electrodes cools and the current decreases again. The minute heating and cooling induced by the chopped laser beam impose an ac component upon the current. The amplitude of this ac component gives an indirect measurement of the absorbance of the solution.

2.2 EXPERIMENTAL

A block diagram of the preliminary instrument for TMEC is presented in Figure 2.1. The apparatus was constructed on a 3-ft. by 4-ft. optical breadboard. The optical source was a 4-mW helium-neon laser at 632.8nm. The intensity of this beam was modulated with a variable frequency mechanical chopper. A beam splitter directed a small fraction (ca. 5%) of the beam onto a reference photodiode. The remaining portion of the beam was focused into the detector cell with an 18×, 10-mm focal length microscope objective. A 1-mm aperture was placed after the lens in the beam path to reduce the amount of scattered light illuminating the electrodes in the sample cell.

The detector cell was designed primarily for ease of construction. The electrodes were constructed from 32-gauge copper insulated wire, 0.2-mm diameter. A length of wire was twisted and formed into a loop. The loop of wire was slit, producing a 0.24-mm gap between the two electrodes. The loop was subsequently fixed with epoxy to the inside of a glass capillary tube (3-mm
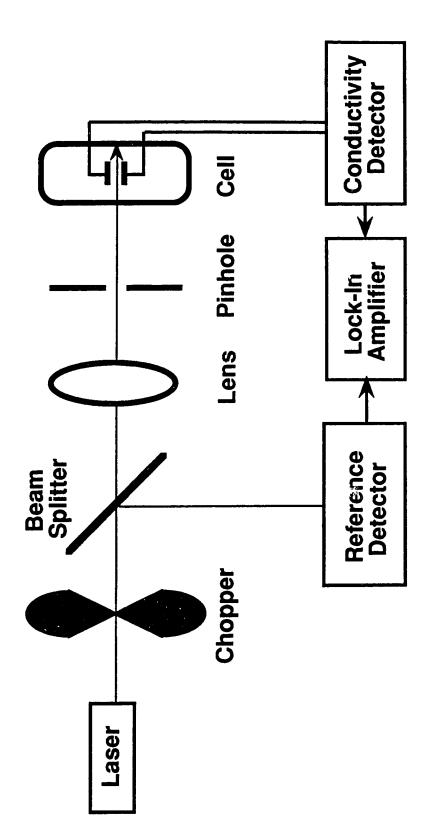
Figure 2.1 Experimental set-up used for preliminary absorbance measurements by TMEC.

i.d.), which served as the sample cell. The bottom of the capillary was connected to a drain tube for ease of sample introduction and replacement. The capillary was mounted vertically on a three axis micrometer translation system to allow convenient positioning with respect to the laser beam waist.

The electronics associated with the conductivity detector are shown in Figure 2.2. A function generator applied a variable frequency signal across the electrodes in the sample cell. The signal amplitude was monitored with a digital multimeter. The applied signal was ac-coupled with a 0.47-μf capacitor to avoid any complicating electrochemical effects that might be incurred by any dc bias voltage. The current through the cell was amplified with a current-to-voltage convertor constructed from an LF351 JFET operational amplifier with a 270-kΩ feedback resistor in parallel with a 5-pf capacitor.

The ac voltage measured at •A in the circuit is proportional to the conductivity of the sample solution. The remaining portion of the circuit acts as a half wave rectifier and low pass filter to demodulate and smooth the conductivity signal for presentation to the lock-in amplifier at •B. In essence, a low frequency conductivity modulation due to laser induced heating between the electrodes is induced upon the high frequency carrier wave voltage. A two-phase lock-in amplifier operating with a 3-sec. time constant measured the amplitude of the laser induced conductivity modulation. The reference signal was generated from the reference photodiode, whose output was amplified with a current-to-voltage converter similar to that described above.
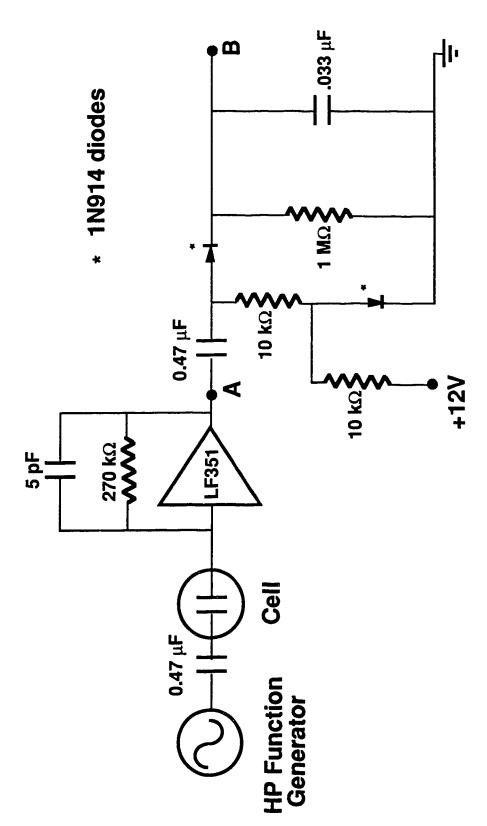
Figure 2.2 Electronics for measuring conductivity of solution in the sample cell. Output "B" is fed to the lock-in amplifier to detect the laser induced conductivity modulation amplitude. The function generator supplies a 20-kHz carrier wave.

The beam waist was located in the gap between the electrodes to minimize the background signal associated with stray light striking the electrodes. This alignment was accomplished by inspection of the beam profile on a white background approximately a meter past the sample cell. To align the system, the electrodes first were centered about the beam axis some distance past the beam waist. This step ensured that the electrodes were centered vertically with respect to the beam axis. The electrodes were then translated toward the lens until the beam profile revealed no interaction with the electrodes. The conductivity detector was first characterized by calibration against an aqueous NaCl solution. In the thermal modulation experiments, methylene blue was utilized as the absorbing species. Mixed 90/10 water/methanol (v/v) solvents were used. The methanol was used to minimize any adsorption of the methylene blue upon the capillary walls. Typically the solutions were made a constant 0.05M NaCl, with the salt performing the function of current conduction. The solutions were filtered with 0.22-μm filters before use to minimize any light scatter upon the electrodes.

2.3 RESULTS AND DISCUSSION

The instrument was first characterized with respect to conventional conductivity measurements. The conductivity of a series of NaCl solutions was measured using a 20-kHz carrier frequency. The conductivity of the solution was linearly related to salt concentration (r >0.9999 n=7), from 0.001-M up to a salt concentration of 0.05-M. Loading of the voltage source, which had an output impedance of 625-Ω, occurred at higher salt concentrations leading to negative deviations from linearity. The conductivity also was investigated as a function of carrier wave voltage for a 0.05-M NaCl solution and a 0.05-M NaCl/10^{-5} M methylene blue solution.

The signal was linearly related to carrier wave voltage up to 3-V rms for both solutions. The positive curvature observed at higher voltages is believed to be due to resistive heating of the solution between the electrodes. Recall that heating of a solution leads to a decrease in the viscosity of the solution and an increase in the conductivity. A carrier wave voltage of 2-Vrms was employed for all subsequent experiments.

Last, the variation in signal with carrier wave frequency was investigated. In conventional resistivity measurements an ac frequency of 1 to 3-kHz is typically used [7,8]. In the present set-up with small area electrodes, a faster 20-kHz wave was needed to overcome the large impedance due to the double-layer capacitance. At higher frequencies, stray capacitance and inductance in the circuit become a significant source of current.

To characterize TMEC, the laser induced signal was measured as a function of laser chopping frequency. Figure 2.3 presents the signal as a function of the modulation frequency for a 0.05M NaCl blank solution and a 0.05-M NaCl/2.5×10^{-5} methylene blue absorbing solution. The signal decreases rapidly with an increase in chopping frequency when the cell is filled with the relatively high concentration dye solution. This roll-off at higher frequencies is typical of other thermooptical phenomena, particularly thermal lens measurements [9,10]. The rate of decrease of signal with chopping frequency is interesting. Consideration of the expected 5-μm laser beam waist size produced by the 10-mm focal length lens leads to an expected thermal time constant of about 4-ms. Instead, the rapid decrease in signal is consistent with the thermal time constant of a much larger solvent volume. This suggests that it is necessary to heat most of the solution between the electrodes to obtain a significant TMEC signal.
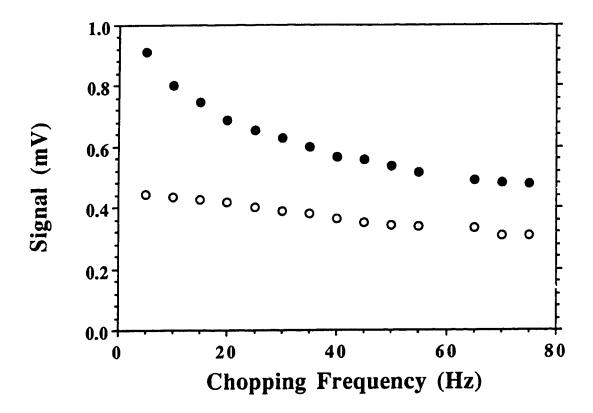
Figure 2.3   Chopping frequency dependence of the thermally modulated
conductivity signal. The open circles are the background signal of a dye
free solution. The filled circles are the signals obtained with a
2.5×10^{-5}M methylene blue solution. Uncertainties in the data are the
same size as the circles. Noisy signals at 60-Hz were measured due to
line frequency interference.

A significant background signal was obtained with the transparent blank solution. The signal was several orders of magnitude larger than what would be expected from absorbance of the water solvent alone. The background signal is attributable to scattered laser light reaching the electrodes. Evidence for this statement is the large increase in background signal, by several orders of magnitude, when the laser cell is translated so as to have an electrode directly illuminated with the laser beam. Copper has a very high thermal conductivity and therefore translates heat generated by stray light absorbance back into the region between the electrodes very efficiently. An increase in the background was also observed for unfiltered solutions, presumably due to an increase in scattered light reaching the electrodes.

The modulation frequency data shows that the magnitude of the TMEC signal and the signal to background ratio are larger at lower chopping frequencies. Signal-to-noise was optimum at a low modulation frequency of 10-Hz, which was used for construction of a calibration curve. Several solutions of varying methylene blue concentration were made by serial dilution from a 3×10^{-4} M stock solution. The solutions were made to a constant 0.05-M NaCl concentration. Figure 2.4 presents a plot of the calibration curve. The signal is linear from the detection limit, 3σ, of 3×10^{-7} M to at least 10^{-5} M (R>0.999). A negative deviation from linearity is apparent at higher concentrations. There are two sources of this deviation. The first source is an attenuation of the laser power reaching the electrodes at higher dye concentrations due to absorbance between the capillary wall and the electrodes. This effect has been observed for other thermooptical techniques [10,14]. The attenuation factor is simply the transmittance of the solution in
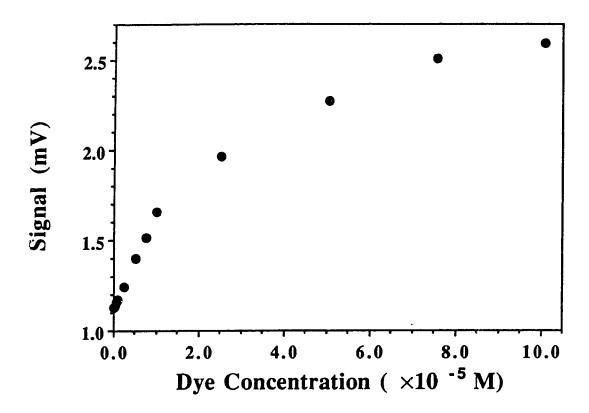
Figure 2.4 TMEC calibration curve for 0.05M NaCl/methylene blue dye solutions using a chopping frequency of 10-Hz. The detection limit is 3×10^{-7}M dye, or $\varepsilon C = 0.012\text{cm}^{-1}$ in a 200-μm path length.

the path between the wall and the electrode. The transmittance may be easily calculated by rearrangement of Beer's law; Eq 2.1,

$$T = \frac{P}{P_0} = 10^{-\epsilon b C}$$

(2.3)

For the measured path length of 0.54-mm between the capillary wall and the electrode axis, and using equation 2.3, it was found that this attenuation of the laser power does not account for all the negative deviation from linearity at the higher concentrations. The second source of the deviation is the self association of methylene blue in solution to form dimers and trimers at higher concentrations [11-13]. This self association changes the optical absorbance spectrum of the dye and decreases the molar absorptivity of the solutions at higher concentrations for the helium-neon wavelength.

The detection limit of 3×10^{-7} M methylene blue can be used to give a more meaningful detection limit in terms of the absorptivity-concentration product, $\epsilon C = 0.012$ cm^{-1}, using the value of $\epsilon = 4 \times 10^4$ M^{-1}cm^{-1} at 633nm [11,14]. This detection limit was achieved in a path length given by the electrode diameter, 200-μm, and a volume of only 8-nL. The absorbance at the detection limit is $A = 2.4 \times 10^{-4}$, comparable to the performance of a commercial absorbance spectrometer.

2.4 CONCLUSIONS

With these preliminary TMEC measurements, absorbance detection limits similar to those of other thermooptical measurements in water were observed. The sensitivity of the measurement is high because of the large temperature coefficient of viscosity for water. On the other hand, there are several factors that lead to a reduction in the precision of the measurement.

The most obvious factor is the large background signal associated with illumination of the electrodes by scattered laser light. The noise associated with the background limits the lowest detectable signal. Minimization of the background signal will result in noise reduction and improved detection limits. Scattered laser light can be reduced by improving the laser beam quality, improving the cell design to minimize retroreflections, and changing the electrode material to platinum, which has a lower absorptivity than copper. Another potential solution is to use an electrodeless conductivity detector [15], although it would present a great challenge to miniaturize such a detector to the scales needed for TMEC measurements.

Applications of a TMEC detector can be found wherever sensitive absorbance measurements in small volumes must be made, especially in aqueous solutions. Absorbance detection using TMEC in capillary liquid chromatography and capillary zone electrophoresis are obvious possibilities. Conductivity detection has recently been applied to capillary zone electrophoresis using miniaturized electrode configurations [16,17]. It should be possible to introduce a laser beam between the electrodes for simultaneous absorbance and conductivity detection in capillary zone electrophoresis.

Additional sensitivity for the TMEC signal may be possible by taking advantage of the shift in equilibrium with temperature for weak acids at room temperature. The acid dissociation constant of typical acids such as carbonic acid, boric acid, and phosphoric acid undergo relative changes of 0.5-2.5% per Kelvin [5]. Even the autoprotolysis constant of water, K_w, changes by 6-8% per degree at room temperature. With such species in solution, a temperature rise would cause increased conductivity through an increase in the number of ions in solution. This conductivity increase would

be in addition to that resulting from the decreased viscosity of the solution. It may be possible to double the sensitivity of the TMEC measurement by suitable choice of buffer, combining both ionization and viscosity temperature dependence of the solvent system.

TMEC forms the first example of a potentially large class of absorbance measurement techniques based upon thermal modulation of electrochemical processes. For example, the potential of a half-cell, E, given by the Nernst equation

$$E = E^o - \frac{RT}{nF} \ln Q$$

(2.4)

undergoes a relative change with temperature that is proportional to the absolute temperature, T. In this equation, E^o is the half cell potential with all species in their standard state, R is the molar gas constant, n is the number of electrons involved in the half reaction, F is the Faraday, and Q is the reaction quotient. The relative change with temperature at room temperature would be about 0.3% per Kelvin, roughly comparable to other thermooptical techniques. Either the absorbance associated with colored species in solution or adsorbed directly upon the electrode could produce the thermally modulated signal. Application with microelectrodes could result in high precision, low volume measurements of both absorbance and electrochemical activity.

REFERENCES

(1)   N.J. Dovichi, J.C. Martin, J.H.Jett, M. Trkula, R.A. Keller,
      Anal. Chem. **56**, 348 (1984).

(2)   T. Hirschfeld, *Appl. Spectrosc.* **31**, 238 (1977).

(3)   D. Betteridge, A.J. Bard, *CRC Crit. Rev. Anal. Chem.* **14**, 267 (1984).

(4)   N.J. Dovichi, *CRC Crit. Rev. Anal. Chem.* **17**, 357 (1987).

(5)   CRC Handbook of Chemistry and Physics, 63rd Edition; R.C. Weast, Ed.;
      CRC Press: Boca Raton, Florida (1982).

(6)   A. Adamson, *A Textbook of Physical Chemistry* , 2nd ed.,
      Academic Press, New York (1979).

(7)   J. Braunstein and G.D. Robbins, *J. Chem. Ed.* **48**, 52 (1971).

(8)   J.T. Stock, *Anal. Chem.* **56**, 561A (1984).

(9)   N.J. Dovichi, J.M. Harris, *SPIE-Int. Soc. Opt. Eng.* **288**, 372 (1981).

(10) T.G. Nolan, W.A. Weimer, N.J. Dovichi, *Anal. Chem.* **56**, 1704 (1984).

(11) E.H. Braswell, *J. Phys. Chem.* **88**, 3653 (1984).

(12) E. Rabinowhich, L.F. Epstein, *J. Am. Chem. Soc.* **63**, 69 (1941).

(13) E.H. Braswell, *J. Phys. Chem.* **72**, 2477 (1968).

(14) G.C. Wetsel and S.A. Stotts, *Appl. Phys. Lett.* **42**, 931 (1983).

(15) R.Shaw, T.S. Light, *ISA Trans.* **21**, 63 (1982).

(16) X.H. Huang, T.K. Pang, M.J. Gordon, R.N. Zare, *Anal. Chem.* **59**, 2747
      (1987).

(17) F.E.P. Mikkers, F.M. Everaerts, Th.P.E.M. Verheggen, *J. Chromatogr.* **169**,
      1 (1979).

CHAPTER 3

CHARACTERIZATION OF

THERMAL MODULATION OF ELECTRICAL

CONDUCTIVITY

A DETAILED STUDY

"Do not worry about your difficulties in mathematics; I can assure you that mine are still greater"

— Albert Einstein

3.1 INTRODUCTION[1]

Photothermal techniques produce high sensitivity absorbance determinations by local measurement of the energy deposited within a sample following absorbance of light. This energy may be detected directly by measurement of the temperature rise in the sample [1] or indirectly by measurement of some physical property of the solvent that changes with temperature. In this latter class of techniques, the properties of solvents that have been exploited for absorbance measurements are: density in photoacoustic spectroscopy [2], refractive index in photothermal techniques [3], and viscosity in thermal modulation of electrical conductivity (TMEC) - the subject of interest in this chapter [4].

A preliminary report outlined the principles of small volume absorbance measurements using TMEC [4]. Briefly reviewing, conductance of ions in solution is inversely proportional to the viscosity, a physical property of the liquid that limits the velocity of those ions. Small changes in the temperature of a liquid will result in relatively large changes in the conductance of the solution. This is a fact that plagues accurate conductance measurements, but one that is taken advantage of in TMEC. The temperature sensitivity of conductivity originates from the large temperature coefficient of viscosity for most liquids.

Conductance measurements in TMEC are made using miniature electrodes with an electrode spacing just large enough to allow passage of a focussed laser beam. The modulated laser beam periodically deposits heat

into the small volume of solution between the electrodes if an absorbing species is present. The heating and cooling of the solution that occurs causes a modulation in the current through the solution. The amplitude of this modulation is proportional to the absorbance of the solution and can be measured using a lock-in amplifier.

Small volume absorbance measurements are of importance in a number of fields, including detection for chromatographic [5] and electrophoretic [6] separation of biological materials. Smaller capillaries are used in these separations to improve the separation efficiency; detection is difficult using conventional absorbance measurements because of the short path length. On-column detection schemes are necessary to keep extra-column bandbroadening to a minimum, motivating the developments of pathlength independent absorbance techniques. TMEC is a technique in this class, where sensitivity can actually increase when the detection volume is decreased. It thus has the potential for application to detection in capillaries.

This chapter presents a detailed study of thermal modulation of electrical conductivity, in both theory and experiment. The theory describes the form and magnitude of the TMEC signal as a function of the electrode dimensions, current, laser power and spot size, carrier frequency, modulation frequency, absorbance and physical properties of the solvent. The theory is compared to experiment to verify some of the predictions.

3.2 THEORY

In this section, a model is presented for TMEC. The coordinate system used in the model is presented in Figure 3.1 A gaussian laser beam (TEM$_{00}$), aligned along the Z-axis, intersects the cylindrical electrolytic resistor defined by the radius of the electrodes, r, and the distance between them, L. Normally the beam is aligned to intersect the center of the resistor, although it may be favourable for an intersection closer to one electrode under certain conditions (see Results & Discussion). A derivation is presented in this section to describe the change in the current through the electrolytic resistor induced by the pulsed laser beam, the impulse response function. This function can then be used to describe the change in current due to any arbitrary excitation waveform. The response functions due to step excitation and infinite square wave excitation functions are described.

3.2.1 The Impulse Response Function

The current through a cylindrical homogeneous resistor is derived by calculating the current density in the resistor due to the movement of ions. The ions have a particular ion mobility [7] and are subjected to a force from the electric field present in the resistor. Ignoring the complications from ion-ion forces, the current has been derived.

$$I = \sum_i \frac{M_i N z_i^2 e^2 \pi r^2 V}{6\pi\eta r_i L}$$

(3.1)

M_i is the molarity of the ith ionic species, z_i is the ionic charge number, r_i is the radius of the ion, e is the electron charge, N is Avogadro's number, V is
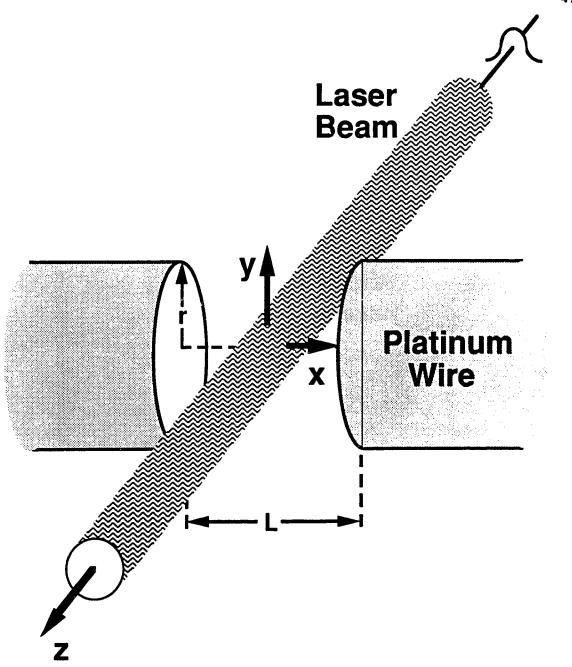
Figure 3.1   Interaction of the laser beam with a cylindrical electrolytic resistor

the voltage applied to the electrodes, η is the viscosity of the medium, r is the radius of the resistor and L is its length. The summation is over the current carrying ionic species in the solution. The current through a thermally non-homogeneous resistor can be described by a weighted average of the current in small volume elements of the resistor,

$$I = \frac{\displaystyle\int_{vol} I(x,y,z)\, d\tau}{\displaystyle\int_{vol} d\tau}$$

(3.2)

where the integral is evaluated over the cylindrical resistor volume. With the assumption that only the viscosity changes with temperature, and knowing the resistor volume, $vol = \pi r^2 L$, the current is given by

$$I = \sum_i \frac{M_i N z_i^2 e^2 V}{6\pi r_i L^2} \int_{vol} \frac{1}{\eta(x,y,z)}\, d\tau$$

(3.3)

where $\eta(x,y,z)$ is the local viscosity of the solution at a point. Equation 3.3 converges to Equation. 3.1 for a homogeneous viscosity between the electrodes. The thermally induced current change, ΔI, is then given by differentiating with respect to temperature. Over the small temperature rise induced by the laser, the viscosity and its first derivative with respect to temperature are assumed to be constant. Collecting variables and simplifying,

$$\Delta I = \frac{\partial I}{\partial T} \times \Delta T = \frac{I}{vol}\left(\frac{-1}{\eta}\frac{d\eta}{dT}\right)\int_{vol} \Delta T\, d\tau$$

(3.4)

The current change is proportional to the integrated temperature rise, ΔT, over the resistor volume. The temperature rise excited by a pulsed gaussian

TEM$_{00}$ laser within a homogeneous absorbing sample has previously been derived [8]. In the coordinate system of Figure 3.1, the temperature rise is given by

$$\Delta T_{impulse}(x,y,t) = \frac{2.303 E \varepsilon C}{2\pi k t_c (1 + 2t/t_c)} \exp\left[\frac{-2(x^2+y^2)}{\omega^2 (1+2t/t_c)}\right]$$

(3.5)

where E is the energy of the laser pulse, ε is the molar absorptivity of the absorbing analyte with concentration C, k is the thermal conductivity of the solvent, ω is the spot size of the beam, t is the time after the pulse and t_c is the time constant of the solvent,

$$t_c = \frac{\omega^2 \rho C_p}{4k}$$

(3.6)

Here, ρ is the solvent density and C_p is its heat capacity. The impulse response of the current, $\Delta I_{impulse}$, is then given by substituting Eq. 3.5 into Eq. 3.4. Using the resistor center as the origin, the temperature field-resistor overlap integral of Eq. 3.4 is easiest worked out using circular cylindrical coordinates with the resistor cylinder defining the geometry. In this case, x=x, y=$\zeta\cos\varphi$ and z=$\zeta\sin\varphi$ where ζ is the radial distance from the resistor axis and φ is the circular angle. The integral becomes

$$\int_{vol} \Delta T_{impulse} \, d\tau = \frac{2.303 E \varepsilon C}{2\pi k t_c (1+2t/t_c)} \int_{-L/2}^{+L/2} \int_0^r \int_0^{2\pi} \zeta \exp\left[\frac{-2(x^2+ \zeta^2\cos^2\phi)}{\omega^2(1+2t/t_c)}\right] d\varphi \, d\zeta \, dx$$

(3.7)

The integration with respect to x is separable and yields an error function of the following form.

$$\int_{-L/2}^{+L/2} \exp\left[\frac{-2x^2}{\omega^2(1+2t/t_c)}\right] dx = \left[\frac{\pi\omega^2(1+2t/t_c)}{2}\right]^{1/2} \text{erf}[Z]$$ (3.8)

The variable Z will be defined below. The remaining double integral is solved first with respect to ζ [9]. The remaining integral with respect to φ is a sum. Each term of the sum cannot be integrated separately because of divergence. A single integration by parts with dv = $1/\cos^2\varphi$, and μ equal to the remainder of the integrand can be followed by the substitution $f = \cos^2\varphi$ to give

$$\int_0^r \int_0^{2\pi} \zeta \exp\left[\frac{-2\zeta^2\cos^2\phi}{\omega^2(1+2t/t_c)}\right] d\phi \, d\zeta = 2r^2 \int_0^1 f^{-1/2}(1-f)^{1/2} \exp[-\kappa f] \, df$$ (3.9)

where κ is a variable defined below. The solution to this definite integral is the product of a Beta function, B, and a degenerate hypergeometric function, Φ [10].

$$\int_0^1 f^{-1/2}(1-f)^{1/2} \exp[-\kappa f] \, df = B(3/2,1/2)\,\Phi(1/2,2;-\kappa)$$ (3.10)

Using the Gamma function definition of a Beta function [11], it can be shown that B(3/2,1/2) = $\pi/2$. The solution to Eq. 3.7 may then be substituted into Eq. 3.4 to give a final expression for the impulse response of the current through the resistor induced by the laser beam.

$$\Delta I_{impulse} = \frac{4.606E\varepsilon C\,I}{\sqrt{2\pi}\,\omega L\,(1+2t/t_c)^{1/2}}\left[\frac{-1}{\rho C_p\eta}\frac{d\eta}{dT}\right]\text{erf}[Z]\,\Phi(1/2,2;-\kappa)$$ (3.12)

$$Z = \left[\frac{L^2}{2\omega^2(1+2t/t_c)}\right]^{1/2} \qquad \kappa = \frac{2r^2}{\omega^2(1+2t/t_c)}$$ (3.13)

The hypergeometric function has an infinite series solution of the following form

$$\Phi(1/2, 2; -\kappa) = 1 + \sum_{n=1}^{\infty} \frac{(-1)^n (2n-1)!! \; \kappa^n}{n! \; (n+1)! \; 2^n}$$

(3.14)

To establish a reference, it is convenient to evaluate the impulse response function, Eq. 3.12, at the small spot limit. First, one assumes that the spot size of the laser is smaller than the dimensions of the electrode so that the cross section of the laser beam as it intersects the electrolytic resistor is totally contained within the resistor dimensions, $\omega < L$ and $\omega < r$. Second, the time after the excitation impulse is assumed to be short enough such that the beam's expanding temperature field, Eq. 3.5, is also confined to the resistor volume. These two assumptions make up the 'small-spot limit' approximation.

Invoking the small spot approximation, the temperature field/resistor volume integral of Eq. 3.4 can be solved by integrating Eq. 3.5 with respect to x and y from $-\infty$ to $+\infty$. The integration in the z-direction is 'physically separable'. It can be accounted for simply by multiplying the result by the resistor path length through which the beam must travel, 2r, the electrode diameter. With the substitution, $x^2 + y^2 = R^2$, one obtains the following,

$$\int_{vol} \Delta T_{impulse} \, d\tau = 2r \times \int_{R=0}^{R=\infty} 2\pi R \times dR \times \Delta T_{impulse}(R,t)$$

$$= \frac{4.606 r E \varepsilon C}{\rho C_p}$$

(3.15)

where a definite integral has been used to obtain the solution to the integral. Substitution of the integral solution into Eq. 3.4 gives the final form of the impulse response function in the small spot approximation.

$$\Delta I \begin{array}{c} \text{impulse} \\ \text{small spot} \end{array} = \frac{4.606\,E\varepsilon Cl}{\pi rL} \left(\frac{-1}{\rho C_p \eta}\,\frac{d\eta}{dT} \right) \qquad (3.16)$$

This function is independent of time, a simple statement of conservation of energy. The temperature field may expand in the resistor, redistributing the laser pulse energy. But while that field is confined to the resistor volume, the volume integral of the temperature change must remain constant.

The relative impulse response function per unit pulse energy, $\Delta I / IE$, has been calculated from Eqs. 3.12 - 3.14 for some typical experimental conditions and is shown in Figure 3.2. Each curve represents a different spot size. The small spot limit calculated from Eq. 3.16 is also shown on the diagram as a horizontal line. Each curve decreases with time after the laser pulse at t=0 as the heat is conducted away from the region of the resistor, eventually converging to zero at large t. Looking at each curve at t=0, it is apparent that the response function approaches the small spot limit as the spot size becomes smaller. This response verifies the two conditions necessary for the validity of the small spot approximation: small ω and small t.
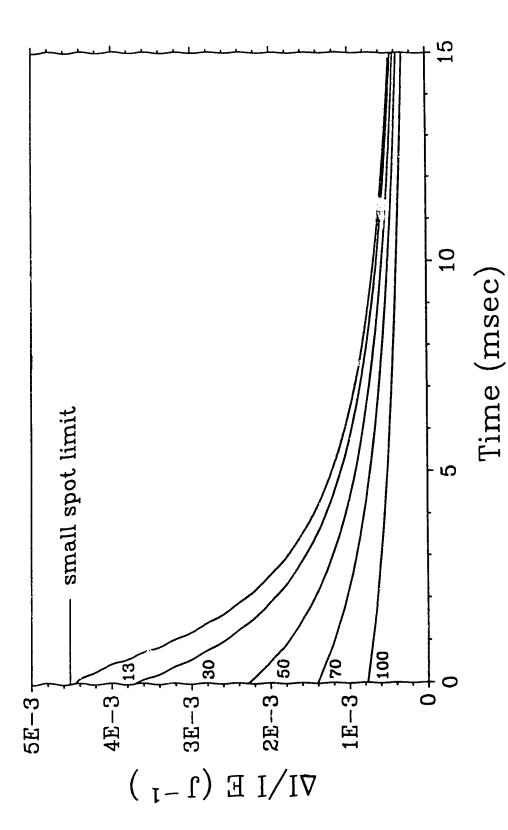
Figure 3.2 Impulse response function calculated from theory using typical experimental conditions. Each curve was calculated using a different spot size, which are labelled in descending order in micrometers. Experimental constants : L = 50-μm; r = 38-μm; εC = .001m-1

Various approximations have been made in the derivation of the impulse response of Eq. 3.12. and Eq. 3.16. These are listed below:

i)   The ions and absorbing analyte are homogeneously distributed between the electrodes.

ii)   In the derivation of the current of Eq. 3.1, Stokes's approximation has been invoked for the frictional coefficient of a particle moving through a viscous medium: $f = 6\pi\eta r_i$ [7]. This approximation assumes a spherical particle of radius r_i.

iii) The electric field, B, between the electrodes is assumed uniform and of magnitude given by:

$E = V/L$ - inside the cylindrical resistor volume

$E = 0$ - elsewhere

This approximation is invalid generally, but has been adopted for conceptual and mathematical simplicity. An equation has been derived to describe the magnitude of the electric fields in a cylindrical resistor and is presented in Appendix A.

iv)   The voltage drop across the double layer capacitance is assumed to be zero. A sufficiently high ac frequency produces a negligible voltage drop by eliminating the double layer impedance.

v)   The spot size of the laser is assumed constant over the length of the beam's intersection with the resistor. Calculations show that under the experimental conditions employed in this study, the variation of the beam spot size over the interaction region is less than 2%.

51
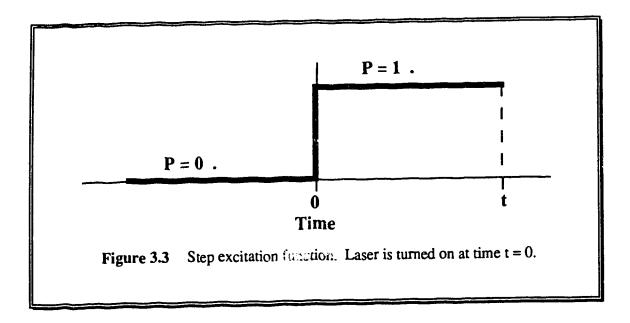
vi) The effects of heat sinks such as quartz windows and platinum wires have been ignored.

vii) The background signal associated with scattered laser light striking the electrodes is ignored.

viii) The ac frequency used for the conductivity measurement is low enough such that Eq. 3.1 is valid.

3.2.2 The Square Wave Response

The impulse response function, Eq. 3.12, describes the change in current through the electrolytic resistor as a function of time after an impulse of light from a pulsed laser excitation source. To obtain the response function, R(t), for an arbitrary excitation waveform, P(t), it is necessary to convolute the impulse response function, I(t), with that excitation waveform. The convolution integral [11,13] is given below.

$$ R(t) = \int_{-\infty}^{\infty} P(t') \, I(t-t') \, dt' $$

(3.17)
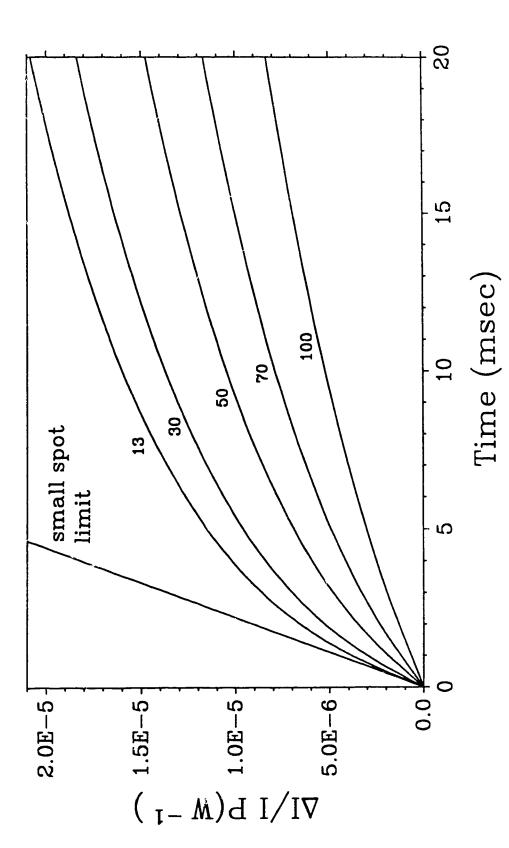
In the experiment, a chopped cw laser is used. The excitation function can be approximated by an infinite square wave with 50% duty cycle. Before solving the convolution integral using the infinite square wave, it is necessary to define the response function for a step excitation waveform. Figure 3.3 shows the step excitation waveform. The cw-laser is turned on at time t=0 and the response is calculated at time, t.

Figure 3.3   Step excitation function. Laser is turned on at time t = 0.

The step response is given by

$$\Delta I_{step}(t) = \int_{-\infty}^{\infty} \Delta I_{imp}(t\text{-}t') \, P(t') \, dt' = \int_{0}^{t} \Delta I_{imp}(t\text{-}t') \, dt' = \int_{0}^{t} \Delta I_{imp}(u) \, du \tag{3.18}$$
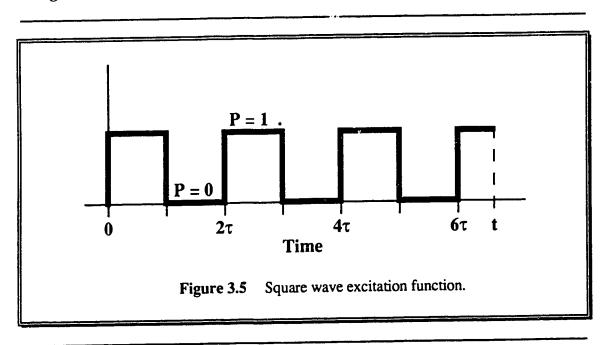
where ΔI_{imp} is given by Eq. 3.12. A simple analytic solution to this integral could not be found and therefore, numerical integration was used. The trapezoidal approximation [12] was used in the integration program that was written. Figure 3.4 shows the step function response for typical experimental conditions. Again, each curve represents a different spot size. The small spot limit step response in the figure was obtained by substituting Eq. 3.16 into 3.18. It represents a limit in which heat flow from the resistor region is not allowed. The step function shows a slow convergence of the laser induced current change to some steady state at large t. At this steady state limit, the absorbed laser power is equal to the heat flow out of the resistor. As $t \rightarrow 0$ and $\omega \rightarrow 0$, the step function approaches the small spot limit.

Figure 3.4 Step response function calculated from theory using typical experimental conditions. Each curve was calculated using a different spot size, which are labelled in descending order. Experimental constants : L = 50-μm; r = 38-μm; εC = .001m-1

As mentioned previously, the infinite square wave excitation function is an approximation to the chopped cw laser excitation. The approximation is in the transition regions, where the straight edge of the rotary chopper passes through the gaussian laser beam. The approximation is a good one under the experimental conditions used in this study. The transition width (13.5 - 86.5%) in time, based upon the beam spot size (0.8-mm) and the chopper radius (50-mm - 2 blade chopper) is only 0.25% of the chopping period.

The square wave excitation function, Figure 3.5, defines the limits of integration for the solution to the convolution integral. The period is 2τ.

Figure 3.5   Square wave excitation function.
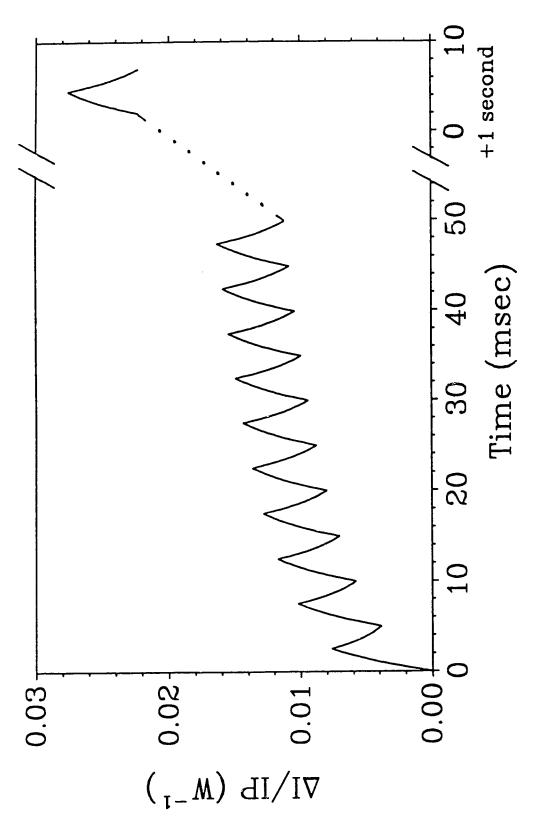
The square wave response function can be divided into two parts, the response during the 'on' (P=1) portion of the nth chopping cycle, $\Delta I^{on}_{sw(n)}$, and the response during the 'off' (P=0) portion of the nth cycle, $\Delta I^{off}_{sw(n)}$. The former is given by the following,

$$\Delta I^{on}_{sw(n)}(t) = \int_{-\infty}^{\infty} \Delta I_{imp}(t\text{-}t')\, P(t')dt' = \sum_{m=0}^{n\text{-}2} \int_{2m\tau}^{(2m+1)\tau} \Delta I_{imp}(t\text{-}t')dt' + \int_{2(n\text{-}1)\tau}^{t} \Delta I_{imp}(t\text{-}t')dt'$$

$$= \sum_{m=0}^{n\text{-}2} \int_{t\text{-}(2m+1)\tau}^{t\text{-}2m\tau} \Delta I_{imp}(u)du + \int_{0}^{t\text{-}2(n\text{-}1)\tau} \Delta I_{imp}(u)du$$

$$= \sum_{m=0}^{n\text{-}2} \left[\int_{0}^{t\text{-}2m\tau} \Delta I_{imp}(u)du - \int_{0}^{t\text{-}(2m+1)\tau} \Delta I_{imp}(u)du \right] + \int_{0}^{t\text{-}2(n\text{-}1)\tau} \Delta I_{imp}(u)du$$

$$= \sum_{m=0}^{n\text{-}1} \Delta I_{step}(t\text{-}2m\tau) - \sum_{m=0}^{n\text{-}2} \Delta I_{step}(t\text{-}(2m+1)\tau) \qquad (2n\text{-}2)\tau \le t < (2n\text{-}1)\tau$$

$$(3.19)$$

In the last line, Eq. 3.18 was used to express the square wave response in terms of a series of step responses. The 'off' portion of the square wave response can be derived in a similar way and is given by

$$\Delta I^{off}_{sw(n)}(t) = \sum_{m=0}^{n\text{-}1} \left[\Delta I_{step}(t\text{-}2m\tau) - \Delta I_{step}(t\text{-}(2m+1)\tau) \right] \qquad (2n\text{-}1)\tau \le t < 2n\tau$$

$$(3.20)$$

The infinite square wave response is obtained by allowing n to approach infinity in Eqs. 3.19 and 3.20. In practice, these equations were solved numerically with n made sufficiently large for convergence. The square wave impulse response, representing the relative change in current through the electrolytic resistor per unit laser power, has been calculated and plotted in Figure 3.6 for the first 10 periods of a 200-Hz excitation function. The function shows a 200-Hz modulation in the current, superimposed on a slowly varying dc current offset. The dc component of the function arises from the slow rise in the bulk temperature of the solution between the electrodes. A finite time is needed for the dc component to reach equilibrium, approximately the same time it takes for the step response function to converge, Figure 3.4.

Figure 3.6 Square wave response function calculated from theory for the first 10 periods and the 200th period of the 200-Hz excitation waveform.

Experimental constants : L = 50-μm; r = 38-μm;   εC = 1m-1

56
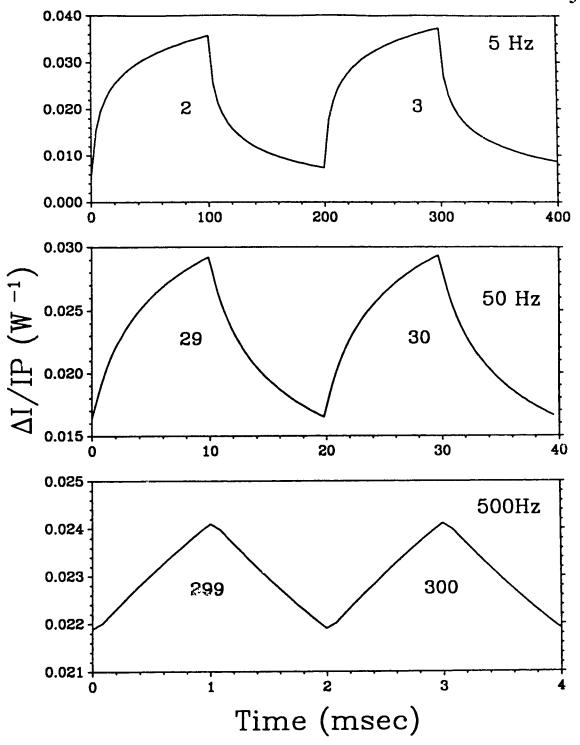
Figure 3.7 Square wave response function calculated from theory for 5-Hz, 50-Hz, and 500-Hz modulation frequencies. The period number is labelled for each wave, each corresponding to about 0.6-seconds after t = 0. Experimental parameters : L = 50-μm, r = 38-μm, ϵC = 1m^{-1}.

The ac component of the square wave response function corresponds to the signal that is measured experimentally. The shape and amplitude of the ac component are expected to be a function of frequency. In Figure 3.7, the transition from a 'square-like' response at 5-Hz to a 'triangle-like' response at 500 Hz is evident. The system behaves as a low pass filter.

2.3 Theoretical Predictions

Based upon the preceding theory, several observations can be made regarding the square wave response function. The signal is predicted to be proportional to a number of parameters: laser power, current and the absorptivity-concentration product of the analyte species. The last of these is important for any quantitative method; the signal is predicted to be linearly related to the analyte concentration.

The signal is also a function of the physical properties of the solvent: density, heat capacity, thermal conductivity and the temperature coefficient of viscosity, $(-1/\eta) \, d\eta/dT$. These parameters appear in brackets in the two impulse equations, Eq. 3.12 and Eq. 3.16. The signal is proportional to this solvent constant, $K_s = [(-\eta \rho C_p)^{-1} d\eta/dT]$. The solvent constant, Table 3.1, varies by a factor of three for the solvents tabulated there. Interestingly, water has a solvent constant that is within a factor of two of the best solvent that could be found, ethanol. Of course, the low dielectric constant of most organic liquids prevents the preparation of ionic solutions in the pure solvent. Properties of the solvent also appear in the time constant, t_c, which does not translate through the convolution integrals, Eq. 3.19 and 3.20, in a linear fashion. Strictly speaking then, the signal is not directly proportional to the solvent constant unless experimental conditions are such that the

small spot limit is valid. Those validating conditions are a small spot size and a high chopping frequency when a chopped cw-laser is employed in the experiment.

Table 3.1   Physical properties of some selected solvents[a].

Solvent	Density (g/mL)	Heat Capacity (J/g °C)	Thermal Conductivity (mW/cm°C)	η Viscosity (cP)	$d\eta/dT$ (cP/°C)	$10^3 \times$ Solvent Constant[b] (mL/J)
Water	0.998	4.18	5.96	1.002	-0.0245	5.86
Methanol	0.791	2.46	2.02	0.597	-0.0076	6.54
Ethanol	0.789	2.36	1.67	1.200	-0.0232	10.4
Acetonitrile	0.786	2.17	——	0.360	-0.0030	4.89
Acetone	0.790	2.18	1.90	0.326	-0.0021	3.74

[a]All constants are at 20 °C [3,14-16].
[b]The solvent constant, $K_s = (-\eta\rho C_p)^{-1} d\eta/dT$.

Other experimental parameters such as electrode radius, electrode separation, spot size and modulation frequency, also do not translate through the convolution integral in a linear fashion because they are not independent of one another. A rigorous calculation for each set of conditions is necessary to predict how the signal will vary with each of these parameters. It is possible, though, to make some general statements.

If the spot size of the laser is kept sufficiently small, the signal will increase (for a constant current) as the dimensions of the electrolytic resistor (r and L) are made smaller. The physical interpretation is that the average

temperature rise in a small volume of liquid will be higher than in a large volume for a given laser power.

The signal should be insensitive to the spot size of the laser beam if the spot size is smaller than the electrode dimensions. This prediction can be verified mathematically by observing that the erf function of Eq. 3.12 will be close to 1 if ω/L is not large. Also, the magnitude of the hypergeometric function, Φ, changes slowly with ω unless ω/L is large. Physically, the power delivered to the resistor is constant, regardless of the spot size, for small ω. If the spot size gets large, less power is deposited into the region between the electrodes, resulting in a smaller signal.

The prediction of signal with chopping frequency is straightforward. At very low frequencies, the current approaches a steady state with time during the 'on' portion of the chopping period. In this limit the signal will be independent of frequency. At high frequencies, approaching the small spot limit, the current response is linear with time during the chopping period and the signal amplitude will be inversely proportional to chopping frequency. To draw on an electrical analogy, the system behaves as a low pass filter in which the amplitude is flat in the low frequency domain and eventually rolls over to give a 20-dB/decade decrease in the high frequency domain. One can envision a series of such amplitude vs. frequency curves in which the 3dB-point of each will be a function of the other experimental parameters.

3.3 EXPERIMENTAL

A cell was constructed to characterize the TMEC technique, Figure 3.8. One design criterion was to have electrodes with well controlled varia: le spacing. The electrodes were constructed by drawing glass tubing over 76-μm diameter platinum wire with a finished outer diameter of 530(10)-μm. The ends of the electrodes were polished progressively using coarse polishing cloth, 6-micron diamond polishing compound, 3-micron alumina and finally 1-micron alumina. The cell was machined from a Teflon block with an inner chamber volume of ~ 0.3-mL. A "V" groove was cut across the front of the block in which the electrodes could sit to a depth such that they remained flush with the front face of the block. A quartz window presses firmly against the front of the block. A thick Teflon ring holds the window in place. The laser beam enters the cell through the front window and exits through a second window at the back of the cell. The distance the beam travels in solution before it passes the electrode central axis is about 265-μm. One electrode was held stationary while the other moved along its axis using a translation stage-micrometer assembly. In this way the electrode spacing could be varied accurately while maintaining the platinum faces of the electrodes directly opposite each other in a parallel plate configuration. The entire cell-electrode assembly was mounted on translation stages for movement in three dimensions by computer controlled actuators.

An ac method was used to measure the conductance of the solution between the electrodes. The electronics were similar to those described previously [4]. Briefly, a high frequency voltage was applied to the electrodes.
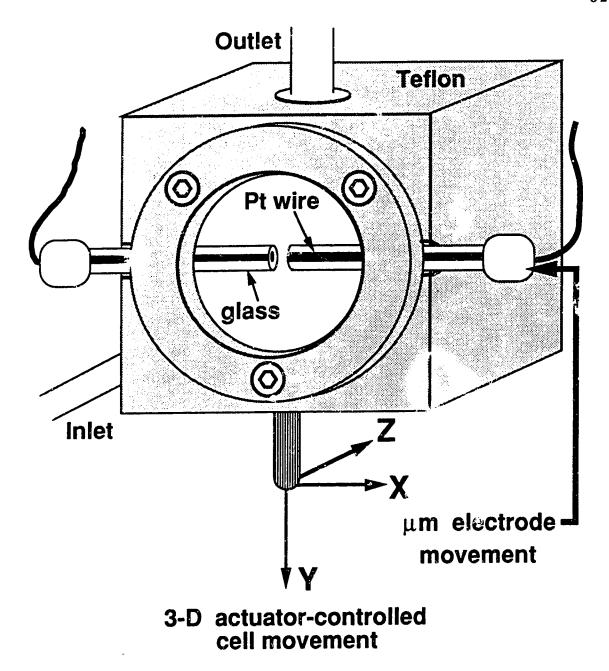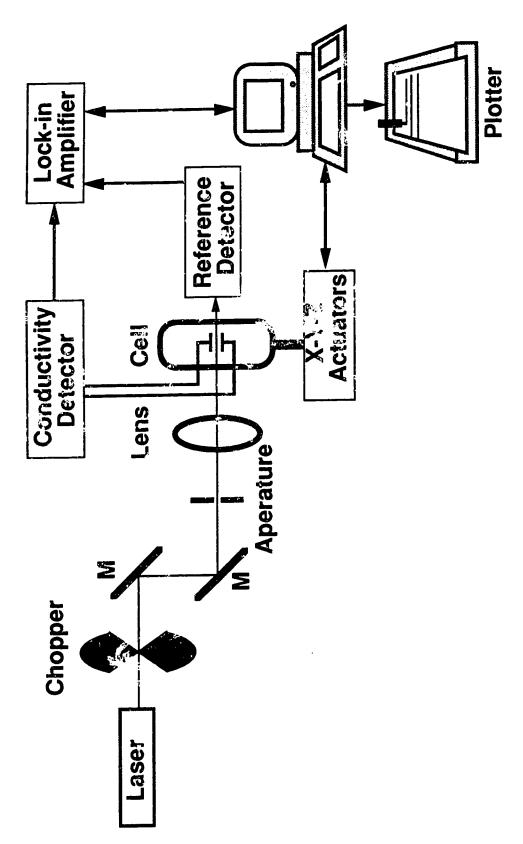
Figure 3.8   Diagram of the cell used for characterization of TMEC. The laser beam travels in the 'z' direction, exiting the cell through a second window at the back. The microelectrodes are 76-μm in diameter.

The ac current passing through the cell was amplified, half-wave rectified and smoothed using an active four pole low pass filter. The resultant dc signal was linear with the conductivity of the solution. It was found that with this electrode configuration, an ac frequency of 40-kHz was needed to minimize the double la ϵ ω acitance impedance. In addition, there are three parallel capacitive imper nces that should be maximized in any conductivity measurement to reduce non-electrolytic current flow. They are the cell capacita... contact and lead capacitance, and the physical electrode capacitance (due to the parallel plate configuration). Grounding of the metal cell inlet and outlet ports helped reduce the cell capacitance. The contact and lead capacitance was reduced by careful electronic design. The physical electrode capacitance is dependent on the dielectric material and the electrode dimensions. This capacitance was measured to be ~ 10-fF at 10-kHz and L=75-μm, insignificant compared to the other sources. The parallel current flow due to all three of these capacitances was typically less than 10% of the electrolytic current flow. This value would be unacceptable for an absolute conductance measurement but is acceptable for the differential measurement of conductance in TMEC.

A block diagram of the experiment is presented in Figure 3.9. A 5-mW HeNe laser beam passes through an optical chopper operating at frequency, f. Mirrors direct the beam through a small 2-mm diameter aperture that eliminates any aberrations in the beam profile. A)X, 16-mm focal length lens focuses the beam to a small spot between the electrodes in the cell. The light exiting the cell strikes a photodiode to generate a reference signal for the two-channel lock-in amplifier. Alternatively, a reference signal from the chopper could be used. The conductivity detector provides the signal for the

Laser

Chopper

M

M

Aperature

Lens

Cell

Conductivity Detector

Reference Detector

Lock-in Amplifier

X-Y Actuators

Plotter

Figure 3.9 Schematic diagram of the experimental setup for characterization of TMEC. The focusing lens is a 16-mm focal length microscope objective.

lock-in amplifier. The lock-in measures both the amplitude and phase of the TMEC signal simultaneously

For beam positioning and for generating x,y scans, an 855C Newport programmable controller and actuators were used to control the movements of the cell with respect to the laser beam. The controller is capable of 0.1-μm movements, although such resolution was not needed in this application. A *Stride* computer both controlled actuator movements and performed data collection from the lock-in amplifier as incremental movements were made.

Aqueous solutions were typically 0.01M NaCl. Fast Green FCF dye (Aldrich, 96%), which has a strong absorbance at the HeNe wavelength, was used for the experiments without further purification. The visible spectrum of the dye was recorded in water as a function of its concentration, NaCl concentration and pH with an HP 8451A diode array spectrophotometer. The purpose of these measurements was to determine the εC product and to assess the extent of aggregation of the dye, if any, at higher concentrations. A 0.01-M NaCl concentration had little effect on the spectrum. The dye behaves as an acid-base indicator, changing from violet in strongly alkaline solutions, to aqua in neutral solutions to green in acidic solutions. The spectrum is constant as the concentration of the dye is increased in neutral solutions up to 10^{-5} M. Above this concentration, the intensity of the main α-band centered at 624-nm starts to decrease in intensity. This decrease in intensity cannot be accounted for by any change in pH that occurs as the dye concentration is increased. Instead, the decrease appears to be due to aggregation of the dye molecules. This effect has been reported previously for other dyes [17].

3.4 RESULTS AND DISCUSSION

3.4.1 Conductivity Detection

The cell-electrode arrangement was characterized with respect to conductivity detection first. For a 0.01-M NaCl solution, the current through the cell was measured for various electrode separations. As expected from Eq. 3.1, the current was inversely proportional to the electrode separation between 40 and 3000-μm (R=0.998, n=15) at a constant applied voltage. A small positive y-intercept was observed, which is attributable to the parallel capacitances mentioned previously. The current through the cell was also linear with the applied voltage (R=0.9991, n=12) from 0 to 3-Vrms. Above this voltage, resistive heating of the solution between the electrodes led to positive curvature. The upper limit to the voltage that may be applied to the electrodes is set by the effects of resistive heating. Heating of the solution between the electrodes presumably leads to convection currents, which cause additional noise in the system. The current was more stable over a long period of time with lower applied voltages. For this reason, voltages of less than 1-V rms were used for subsequent experiments.

In ac conductance measurements, audio frequencies are necessary to ensure the resistance limiting the current flow is, in fact, the electrolytic resistance, R_{el}. Frequency dependent impedance also arises from the double layer capacitance, C_{dl}, at each electrode. The frequency dependence of the current through the cell, Figure 3.10, exhibits typical behavior. At low frequencies, the double layer impedance is much greater than the electrolytic resistance and the current is very small. As the frequency, F, increases, the double layer impedance becomes comparable to the electrolytic resistance and
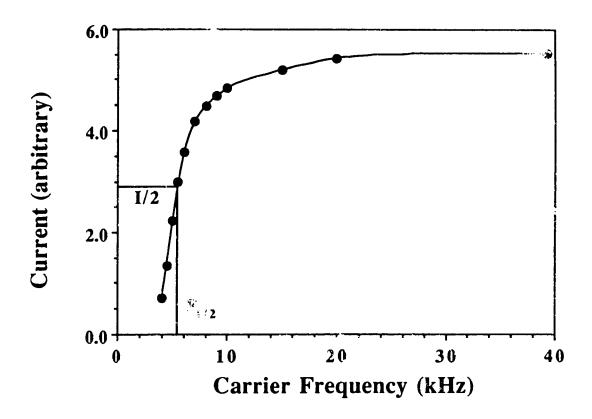
Figure 3.10 Effect of double layer capacitance on the current through the cell. The double layer capacitance dominates the impedance at low frequencies. The electrolytic resistance limits the current at high frequencies.

the current goes through a transition region where it increases quickly. At higher frequency, the double layer impedance becomes negligible and the voltage source sees a pure resistor; the current levels off to a constant value.

Mathematically, the current through the cell can be expressed as

$$I = \frac{V}{\left[R_{el}^2 + (1/2\pi FC_{dl})^2\right]^{1/2}}$$ (3.21)

assuming ideal resistance and capacitance [18]. With some rearrangement, the frequency at half the maximum current level, $V/2R_{el}$, can be used to estimate the double layer capacitance,

$$C_{dl} = \frac{1}{2\sqrt{3}}\frac{1}{\pi R_{el} F}$$ (3.22)

For the conditions used in this study, 76-μm diameter platinum electrodes and 0.005M NaCl solutions, the double layer capacitance was found to be 94-pF using Eq.3.22. A frequency of 40-kHz was used with the conductivity detector to overcome this capacitance, ensuring a purely electrolytic impedance in the cell.

3.4.2 Signal Imaging

A thermal modulation of the solution conductivity will result from any phenomena that produces a temperature rise between the electrodes. Only modulations at the frequency of the chopped laser are measured by the lock-in amplifier within its frequency bandwidth. In addition to the TMEC signal resulting from direct absorbance between the electrodes, laser light striking the electrodes also generates a thermal modulation signal. The metal wire reflects most of the light, but absorbs a finite amount causing a local

temperature rise on the wire. Platinum, being a metal, has a very high thermal conductivity, 730-mW/cm/°C at room temperature [14], more than two orders of magnitude greater than that of water. Heat is transmitted along the wire very efficiently to regions of lower temperature. The heat is then transferred to the solution between the electrodes leading to a thermal modulation of the current at the same frequency as the chopped laser.

Figure 3.11 shows the TMEC signal as a function of X-Y position for a two dimensional scan of the region near the electrodes using a blank solution and a chopping frequency of 200-Hz. Individual pixels in the plot are 10-μm on a side. The significant signal produced by wire absorbance results in a clear image of the wires. The valley between the electrodes shows a low absorbance by the blank solution. The signal drops off quickly as the laser spot moves along the wire away from the resistor region. The explanation is that the heat must be transmitted a progressively longer distance to the resistor region in the same time period, τ, where τ (=1/2f) is the "on" time of the laser during a chopping period. Other measurements have shown that the signal falls off much more slowly with distance along the wire as the chopping frequency is reduced.

The measurement of solution absorbance in TMEC requires measurement of the signal in the valley region beween the electrodes. The large signals produced by the laser striking the platinum wire make the alignment process trivial. Figure 3.12 shows three closeup images of the region between the electrodes using step sizes of 2.5-μm. Figure 3.12a shows the image generated with a blank solution. The edges of the wire are observable as sharp rises in signal on the left and right sides of the scan. Any residual signal on the 'valley floor' constitutes a background for the
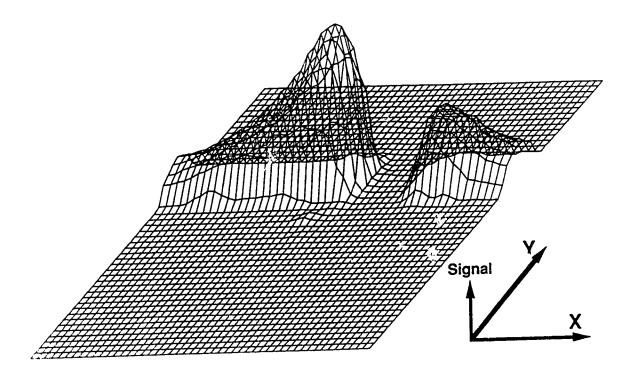
Figure 3.11 Laser scan of the TMEC signal generated in the vicinity of the electrodes for a blank solution. The signal due to the laser striking the electrodes has generated their image. TMEC absorbance measurements are made by aligning the beam to pass between the electrodes. Pixels are 10-μm.
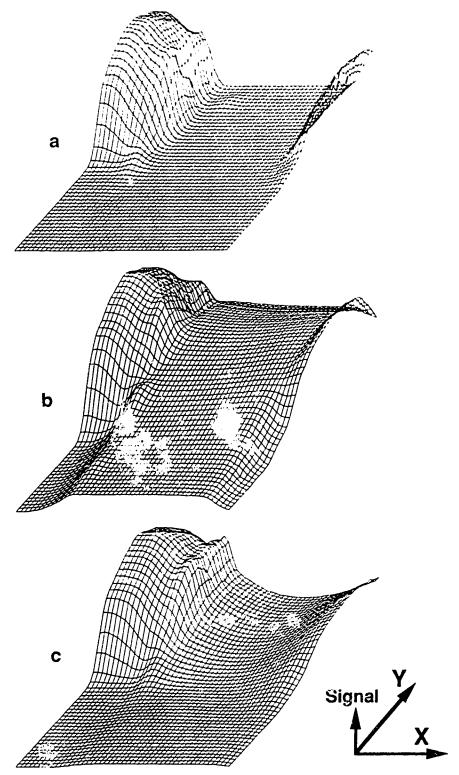
Figure 3.12 Closeup scans of the signal in the resistor region using 2.5-μm pixels.
(a) blank solution (b) absorbing solution, f = 10-Hz (c) absorbing
solution, f = 200-Hz.

absorbance measurement. The magnitude of the background signal has been reduced greatly in this study compared to the preliminary report of TMEC [Chapter 2 or ref. 4]. This reduction was accomplished by paying careful attention to beam reflections off the windows and by using polished Pt electrodes to enhance the specular reflection off of the electrode surface. Figures 3.12b and 3.12c show images of the same region with a 4.0×10^{-5}M dye solution for chopping frequencies of 10-Hz and 200-Hz respectively. The signal maximizes between the electrodes and then falls off gradually in the radial (y) direction. The signal observed when the laser is shining in a region outside the resistor volume arises from diffusion of heat into the resistor region The effects of the beam induced modulation will extend to a distance given by the thermal diffusion length, η_ω,

$$\eta_\omega = \left(\frac{D}{\pi f}\right)^{1/2}$$

(3.23)

The thermal diffusivity of the solution, D, is given by

$$D = \frac{k}{\rho C_p}$$

(3.24)

Eq. 3.23 suggests that the distance over which the effects of the modulated beam can be detected, decreases with the modulation frequency. Thus, as the chopping frequency is increased, Fig. 3.12c, contributions to the signal from diffusion through solution in the radial direction are diminished relative to the signal arising from direct absorbance between the electrodes. Since the thermal diffusion contributions are diminished at higher frequencies, the signal reflects a higher spatial resolution. A 'U-shaped' signal between the electrodes along the X direction is observed in the higher frequency scan. The sharp falloff of the background between the electrodes for

the control scan, Fig. 3.12a, demonstrates that the unusual shape in Fig.c must be attributable to variations in the TMEC sensitivity between the electrodes. Larger signals are observed near the electrode faces as opposed to the solution center.

To help find the source of this inhomogeneity, a calculation was done to evaluate the change in the magnitude of the electric fields with distance between the electrodes. Appendix A of this chapter derives the expression given below, which can be used to calculate the magnitude of the electric field at a point along the resistor axis for this particular cylindrical parallel plate configuration.

$$E = \frac{\sigma}{K\varepsilon_o}\left[1 - 1/2\left(\left[\frac{1}{1+(R/(0.5+\beta))^2}\right]^{1/2} + \left[\frac{1}{1+(R/(0.5-\beta))^2}\right]^{1/2}\right)\right]$$

(3.25)

K is the dielectric constant of the medium, ε_o is the permittivity of free space, R is the ratio of the wire radius to the electrode separation, r/L, and β is the fractional distance along the axis between the electrodes, $\beta=x/(L/2)$.

This function has been plotted as a function of β for various values of the dimensionless parameter R in Figure 3.13. As R approaches infinity, corresponding to small electrode separations, the electric field along the axis becomes uniform and approaches that given for a parallel plate configuration, $|E_{pp}| = \sigma/K\varepsilon_o$ [19]. The electric fields in the diagram are presented as a fraction of this value. As R decreases, the electric field becomes smaller and the magnitude of the field at the electrode surface asymptotically approachs a limit of $E_{pp}/2$. At the same time, the electric field on axis between the electrodes approaches zero. The dashed line, R=0.381, corresponds to the
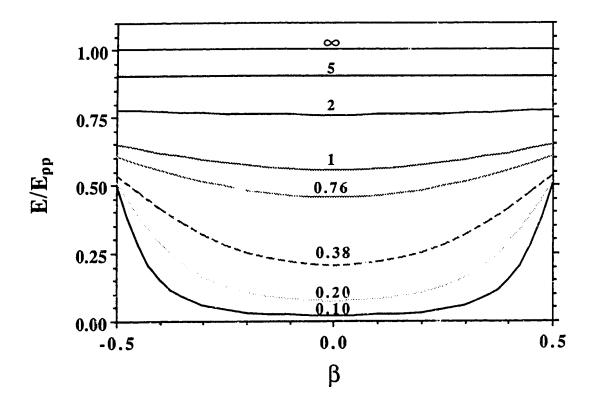
Figure 3.13 Plotted are the curves of the calculated (Eq. 3.25) electric field strength on-axis of the cylindrical electrolytic resistor as a function of the fractional distance between the electrodes, β. Each curve represents a particular value of R, the electrode radius to electrode separation ratio. E_{pp} is the field inside an infinite size parallel plate capacitor.

particular r/L ratio used for the scans of Fig. 3.12. The shape of this line qualitatively matches the shape of the 'U' valley between the electrodes in Fig 3.12c. The imperfect match of the electrodes (due to differences in polishing or deviations from a perfect axial alignment) and the finite spot size of the laser beam discourage attempts to quantitatively compare the experimental and theoretical curves. Higher current densities are expected close to the electrode face because of the higher electric fields there. The higher current densities cause a greater sensitivity to be observed near the electrode face for absorbance measurements by TMEC. This spatial sensitivity variation could only be exploited analytically when using a high chopping frequency. Unfortunately, the sensitivity also decreases with chopping frequency.

The results of Eq. 3.25 and its graphic representation in Fig. 3.13 should also have importance for the design of conductivity detectors used in liquid chromatography and capillary zone electrophoresis. A low value of R would suggest that the approximation of a cylindrical electrolytic resistor of radius, r, is unreasonable. The effective detector volume, which is important for band broadening considerations, may be much larger than the volume of the cylinder.

3.4.3 Testing the Model

In section 3.2, a mathematical model was developed to describe the signal measured in TMEC. Experiments were run to test this model and to investigate the performance of the technique for absorbance measurements. Water was used as a solvent, unless otherwise mentioned, with moderate dye concentrations of 5×10^{-7}M. The 5-mW laser was aligned to intersect the

resistor center origin (Fig. 3.1) and a time constant of 3-seconds was used on the lock-in amplifier.

Current and Laser Power Dependence

For an electrode spacing of 100-μm, the lock-in signal and current were measured as the voltage was increased from 0.0 to 3.0-Vrms. The lock-in signal was found to be linear with current, Figure 3.14a (R=0.9998, n=12), as predicted from the theory. To measure the signal as a function of laser power, a linear polarizer was placed in the path of the polarized laser beam. The power reaching the electrodes was varied by simply rotating the polarizer. A power meter was used to measure the power of the beam prior to measurement. Using an electrode spacing of 50-μm, the lock-in signal increased linearly with the power, Figure 3.14b (R=0.9998, n=7). Interestingly, the noise in the signal did not increase over this power range. This observation indicates that the noise in the system is laser power independent, at least at a power of 5-mW. In this situation, one can obtain increased signal-to-noise ratio and proportionately lower detection limits simply by increasing the laser power further.

The noise in the system is associated with the conductivity measurement. Fundamental noise sources are either Johnson noise or shot noise. A quick calculation showed that the Johnson noise associated with the largest resistor (750-kΩ) in the circuit would be only 20-nV. The shot noise associated with the measurement is given by the following expression [20],

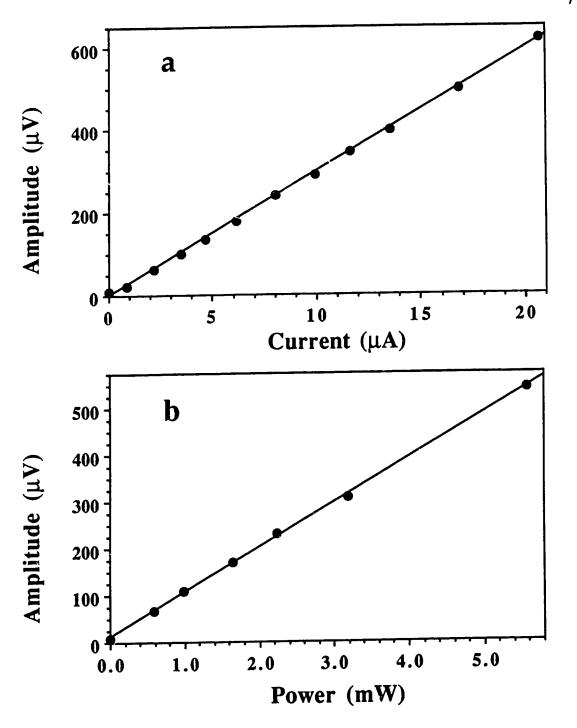$$I_{noise}(\text{rms}) = (2eIB)^{1/2} \qquad (3.26)$$

Figure 3.14 TMEC amplitude signal as a function of: a) cell current, L = 100-μm, P=5mW; b) laser power, L=50-μm, I=19-μA. A modulation frequency of 10-Hz was used for both studies.

where e is the electron charge, I is the average current through the cell and B is the frequency bandwidth. Typical ac currents th·. $_gh$ the cell are 2.5-μA rms and the frequency bandwidth of the lock-in is $1/(8t_c)$ using the time constant of the lock-in amplifier, t_c [21]. Taking amplification into account, the expected shot noise appearing at the lock-in was 0.5-μV. Depending on the day, the observed noise was anywhere from one to six times this fundamental limit for chopping frequencies of 10 to 100-Hz. Replacing the cell with an appropriate 300-kΩ resistor resulted in noise that was consistently within a factor of two of the fundamental shot noise limit. This observation suggests that there is extra noise associated with the electrolytic resistor, possibly convection noise due to power dissipation in the solution.

Electrode Separation and Chopping Frequency Dependence

The variation of the sensitivity with electrode spacing, L, and chopping frequency, f, was measured under constant current conditions for the ranges L=50 to 200-μm and f=10 to 100-Hz. The amplitude was also calculated using a converged square wave response function (section 3.2) with identical experimental conditions. The experimental and theoretical amplitudes are illustrated in Figures 3.15a and 3.15b respectively. The absolute magnitude of the theoretical amplitude is larger than the experimental amplitude for reasons that will be discussed later. Because of this discrepency, the two surfaces in Figure 3.15 have been normalized arbitrarily at the point of maximum signal, L=50-μm and f=10-Hz.

The general trends are shown by either figure. The signal maximizes at low frequencies and small electrode separations. This observation can be rationalized in the following manner. At low frequencies, the heating time
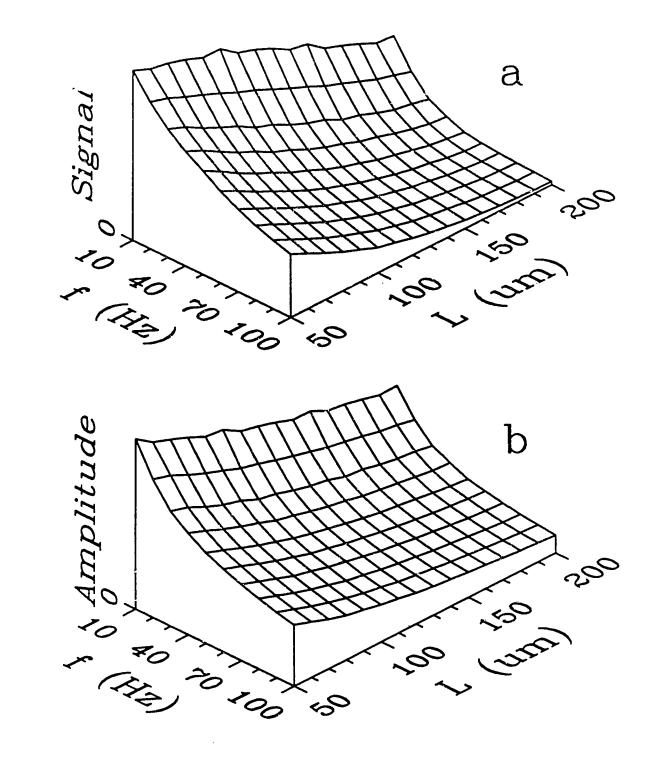
Figure 3.15 (a) Experimental signal measured under constant current conditions and normalized at f=10-Hz, L=50-μm. (b) Theoretical signal, similarly normalized and calculated from a converged square wave response.

during the 'on' cycle and cooling time during the 'off' cycle of the chopping period are long, allowing a large temperature change and current modulation. With smaller electrode separations, the volume of liquid that must be heated is smaller, generating a greater average temperature rise between the electrodes. In the same vein, the signal also is expected to increase at constant current as the electrode radius is decreased, although no attempt was made to measure this experimentally. Qualitatively, the frequency response of the signal is in best agreement with the theory at small electrode separations. For example, at L=50-μm, the experimental signal decreases by a factor of 2.72 when the chopping frequency is increased from 10 to 100-Hz. The corresponding factor for the theoretical calculation is 2.79, a good agreement. On the other hand, the same factors at a larger electrode separation of L=200-μm are significantly different, 21.4 experimentally and 5.0 theoretically. The normalized experimental signal at large electrode separations and high chopping frequencies is smaller than predicted by theory. This discrepancy can be seen by comparing Figures 3.15a and 3.15b in the lower right quadrant. In fact, the experimental normalized signal is 5.3 times smaller than the theoretical normalized signal at the corner of that quadrant. This difference is not surprising considering that the theoretical model uses a constant electric field approximation between the electrodes. The rigorous electric field calculation, Eq. 3.25 and Fig. 3.13, suggest that the electric fields at the center of the electrode are smaller than predicted by the constant field approximation. The effect of the smaller fields can only be observed experimentally at high modulation frequencies because of the improved spatial resolution.

The theoretical model presented in section 3.2 is reasonable for small electrode separations. A rigorous comparison of experiment and theory at large electrode separations would invalidate the approximation of a cylindrical electrolytic resistor with constant electric field. Instead, the electric field would be calculated in three dimensional space. The overlap integral in Eq. 3.4 would involve the integration of the overlap between the laser induced temperature field with the nonhomogeneous electric force field.

The interpretation of Fig. 3.15 is that the greatest analytical sensitivity can be obtained in the regime of small electrode separations and low chopping frequencies. For the fundamental shot noise limit, Eq. 3.26, the signal-to-noise surface would look identical to Fig. 3.15. At low modulation frequencies, some $1/f$ noise was seen experimentally, but the best signal-to-noise was still found at low frequencies and small electrode separations.

Spot Size Dependance

To study the spot size dependency of the signal, a large electrode separation of 125-μm was used, allowing a wide range of spot sizes, 9-40-μm, to be employed without interference from the background signal associated with light striking the electrodes. The spot size was varied by moving the lens with respect to the cell using a micrometer. The spot size of the beam, $\omega(z)$, a distance z away from its focus with minimum spot size ω_0, is expected to vary in a predictable manner [3],

$$\omega^2(z) = \omega_0^2 \left[1 + (z/z_c)^2\right] \tag{3.27}$$

Here, z_c is the confocal distance given by $z_c = \pi \omega_0^2/\lambda$, with λ being the wavelength of the laser beam. The spot size of the beam between the

electrodes was measured in a rather unconventional way. At each lens position, the X-actuator was used to scan the electrode with respect to the beam with a blank solution in the cell. As the beam spot moved from the electrode into the region between the electrodes, the background signal gave a good approximation to an error function for the overlap of the gaussian beam with the electrodes. The estimated spot size was extracted from this data by measuring the spatial width of the function (13.5 - 86.5%), which is theoretically equivalent to 2ω. The smallest spot size observed with the 10× lens was estimated to be 9-μm.

The estimated spot sizes measured at each lens position are shown in Figure 3.16a. The beam waist is located between the electrodes at a relative lens position of ~ 400-μm. The TMEC net signal, represented by the dots with 95% confidence error bars, was measured with a moderate concentration of dye solution at each lens position using a modulation frequency of 10-Hz, Fig. 3.16b, and 50-Hz, Fig. 3.16c. The solid lines represent the theoretical calculation of the amplitude using the converged square wave response and normalized at small ω.

The theoretical curves at both frequencies suggest that the signal should decrease slightly (10 to 15% respectively) from the smallest spot size to a spot size that is the same size as the electrode radius, 38-μm. The experimental data show a constant signal over this range of spot sizes and even possibly a slight increase (2 to 5%) in the measured signal. This slight discrepency may be accounted for by arguing that the edges of the gaussian beam at large spot sizes are closer to the electrode faces. It was shown previously that regions close to the electrode have larger electric fields giving rise to larger signals when the laser beam intersects the resistor there.
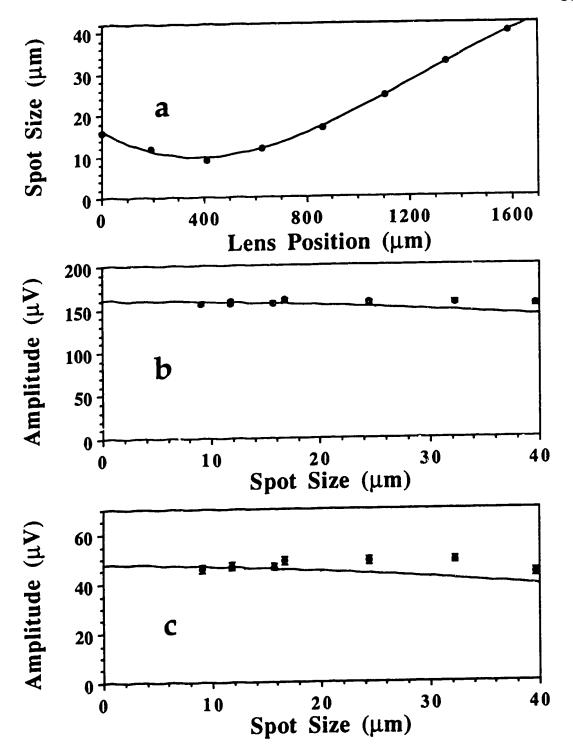
Figure 3.16   Spot size dependence of the TMEC signal for a 125-μm electrode separation (a) Spot size measured at each lens position. At 10-Hz(b) and 50-Hz(c), dots represent experimental signals and solid lines represent the theoretical signals normalized at ω=10μm.

Considering all, the signal is relatively insensitive to changes in spot size providing that the beam is confined to the volume between the electrodes. This behavior is in contrast to thermooptical methods such as the crossed-beam thermal lens, thermal lens calorimetry and thermal diffraction, which show an inverse relationship between the sensitivity and the spot size.

Solvent Studies

Like other calorimetric methods of absorbance measurement, the sensitivity of TMEC is expected to be solvent dependent. To compare the sensitivity of the absorbance measurement for different liquids, measurements were carried out in a variety of common solvents under constant experimental conditions. The solvents used were not pure, but instead were 20% H_2O by volume with 4×10^{-5} M dye concentration. The water was needed to ensure solubility of the 0.01-M NaCl charge carriers. The absorbance of each solution was measured on a commercial spectrophotometer. The spectra allowed correction for changes in the ϵC product, caused by the volume change upon mixing with water and solvent effects on the dye spectrum. The signals were measured for two extremes of the electrode separation, L=50 & 200-μm, and chopping frequency, f=10 & 200-Hz. Theoretical calculations of the signal were carried out for each solvent under the same experimental conditions using the converged square wave response (see Program Train in Appendix C).

Table 3.2 presents the results in a normalized form. All theoretical and experimental signals are given relative to the appropriate signal in water. Theoretical signals were not calculated for acetonitrile, for which a value of the thermal conductivity could not be found. The relative theoretical signals

Table 3.2 TMEC sensitivities in other liquids.

Solvent [a]	f = 10-Hz [b]				f = 200-Hz			
	L = 50-μm [c]		L = 200-μm		L = 50-μm		L = 200-μm	
	Th.[d]	Exp.[e]	Th.	Exp.	Th.	Exp.	Th.	Exp
Acetonitrile	—	1.96	—	1.60	—	1.74	—	1.38
Acetone	0.76	2.77	0.72	1.61	0.66	2.15	0.64	1.34
Ethanol	2.43	2.64	2.20	1.94	1.89	2.08	1.80	1.32
Methanol	1.39	1.68	1.30	1.47	1.17	1.39	1.13	1.21
Water	1.00	1.00	1.00	1.00	1.00	1.00	1.00	1.00

[a] Solvents were mixed with 20% H_2O by volume to facilitate dissolution of the 0.01M NaCl charge carriers.

[b] f is the chopping frequency.

[c] L is the electrode separation.

[d] Theoretical calculation using a converged square wave response (Section 3.2). Pure solvents were assumed in the calculations. All calculations are compared to H_2O which was normalized to one.

[e] Experimental measurements compared to water.

in the far right side of the table (large L, high f) converge to the ratio that would be predicted in the small spot limit, simply the ratios of the solvent constant in Table 3.1.

The experimental signals in different solvents are all greater than the signal in water, although at most by a factor of 2.8. The normalized signals show a decrease at higher frequencies. For example, at 200-Hz and 200-μm electrode separation, all signals in the five solvents are within 38%. This similarity is attributable to the smaller time constant of water, Eq. 3.6, which allows the aqueous system to respond faster at high frequencies.

The relative sensitivities of acetone, methanol and, to a lesser extent, ethanol are all larger than predicted by theory. For example, the relative sensitivity of acetone is 200 to 400% more sensitive than predicted by theory under the various conditions. A point to remember here is that the experimental measurements were made with solvents mixed with 20% water by volume. The water was added solely for the purpose of increasing the solubility of the current carrying salts. It is proposed that this mixing is the source of the enhanced sensitivity in these solvent systems, as will be discussed in the next section.

As a small volume absorbance detector, TMEC shows promise for use with water. Other calorimetric absorbance techniques such as thermo-optical detection are not suitable for use with water. Water is the least sensitive solvent in these methods by one to two orders of magnitude compared to other common solvents [3,22,23]. TMEC shows better sensitivity in water compared to other calorimetric techniques because of a relatively high value

of $d\eta/dT$ and a decreased dependency on the thermal conductivity of the solvent.

3.4.4 Viscosity and Mixed Solvents

The viscosity of a liquid such as water, Figure 3.17a, varies exponentially with temperature in the following manner

$$\eta = A_\eta e^{E^*/RT}$$ (3.28)

where A_η is a suitable constant, R is the gas constant, T is the absolute temperature and E^* is a characteristic energy of the solvent [7,24]. This characteristic energy represents the barrier that a molecule must overcome in a structured solvent, in order to jump from one solvent 'cage' to another. This escape process is similar to that required for a molecule to break free from a bulk liquid in the vaporization process. Not surprisingly, E^* is typically about one third the energy of vaporization for many liquids. Values of E^* are about 10 to 20-kJ/mole.

The TMEC signal is proportional to the solvent constant, K_s, Table 3.1. Substituting Eq. 3.28, the solvent constant becomes

$$K_s = \frac{-E^*}{\rho C_p RT^2}$$ (3.29)

The absorbance sensitivity is proportional to the viscous energy, E^*. This energy may be expected to change in mixed solvents, affecting the viscosity of the mixed liquid. For ideal mixtures, the fluidity, ϕ ($\phi = 1/\eta$), is expected to vary linearly with solvent composition. For non-ideal liquids, the intermolecular interactions, A-B, can modify the solvent structure, changing
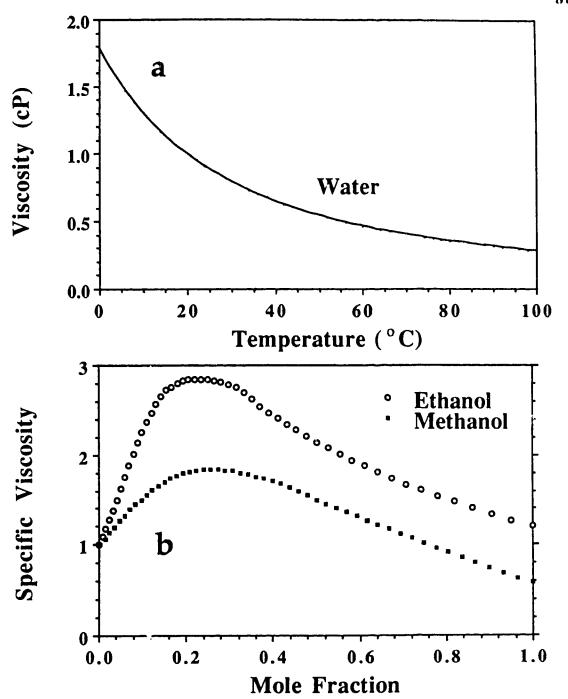
Figure 3.17   (a) Exponential behavior of the viscosity of water with temperature.
From *CRC Handbook of Chemistry and Physics*, 63rd edition (1983).
(b) Specific viscosity of aqueous solutions of ethanol and methanol.
Non-ideal behavior is characterized by a maximum in the plots.

E* and the viscosity in a non-ideal manner. Mixtures in which A-B attractive interactions are stronger than A-A or B-B type interactions exhibit an increase in E*, viscosity, and density, and show a dip in the appropriate vapour pressure diagram. The four solvents used in this study exhibit this type of behavior when mixed with H_2O, presumably due to increased hydrogen bonding. An obvious clue to this behavior is the observable decrease in volume when the two liquids are mixed. The specific viscosity ($\eta_{solvent}/\eta_{water}$ at 20°C) of aqueous mixtures of ethanol and of methanol, Figure 3.17b, show a maximum in the plot. Acetone behaves in a similar manner. It was verified that the positive deviation from the ideal is attributable to an increase in E* and not an increase in A_η, by examination of viscosity data of the mixed solvents as a function of temperature [11]. The result of mixing the two solvents is an abnormally large temperature coefficient of viscosity. The room temperature coefficient of viscosity is 2.4%/°C for water, 1.9%/°C for pure ethanol and 4.0%/°C for a 40% (v/v) solution of ethanol. A significant signal enhancement occurs in the mixed solution.

The increase in E* in a solvent mixture should result in increased sensitivity for TMEC absorbance measurements. This possibility was investigated by recording the signal for 0, 20, 40, 60 and 80% ethanol solutions (v/v) under constant experimental conditions. Corrections (<2%) were made again for variations in the value of the εC product. The signals are plotted in Figure 3.18 as a function of the mole fraction of ethanol. Also shown is the theoretical signal for ideal solutions, in which linearity in ρ, C_p, k and φ was imposed. The experimental and theoretical signals were normalized for pure water. The experimental signal shows positive deviation from ideality. The
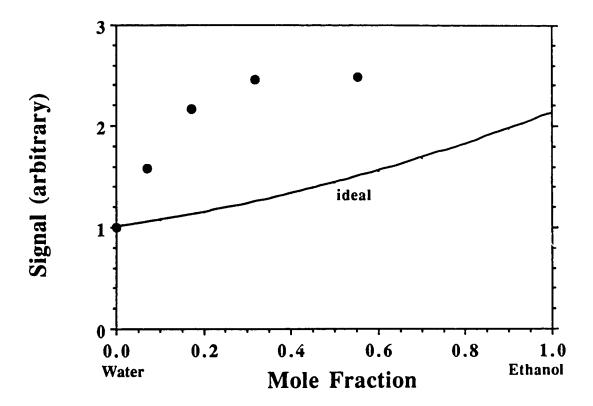
Figure 3.18 Experimental and theoretical ideal signals in ethanol solutions. Signals were normalized to 1.0 in H_2O. The theoretical ideal signals were calculated with an imposed linearity of ρ, C_p, k and ϕ. The signals are enhanced in ethanol solutions due to an increase in the characteristic viscous energy, E^*.

maximum deviation from the theoretical is ~ +95% at a mole fraction of 0.25. The corresponding deviation calculated from the viscosity data was +75% [25]. The density of the ethanol solutions deviates from the ideal by a maximum of only 2.3%. Clearly then, it is the increase in E^* that is the major contributing factor to enhanced signals in mixed solutions. Other solvent systems could show even higher enhancements.

3.4.5 Quantitation and Detection Limits

As an analytical absorbance measurement technique, one will want to relate the signal measured in TMEC to the concentration or molar absorptivity of the sample. For absolute absorbance measurements, one must consider the accuracy of the theory presented in Section 3.2. All theoretical signals presented thus far in this chapter were obtained from a program, written to perform the necessary numerical integrations using the appropriate equations (Eqs. 3.12-3.14; 3.18-3.19). Input to the program included the following parameters: r, L, ω, P, f, I, ρ, C_p, k, $d\eta/dT$, and εC. Reasonable values for the rms factor of the waveform were used, between 0.5 and 1.0. At the smallest electrode separation used, 50-μm, the calculated amplitude was 2.5 to 3.0 times larger than the observed signal for the frequency range of 10 to 100-Hz. This type of deviation is reasonable considering the approximations made in the model.

Much of the discrepancy can be traced to the approximation of a uniform electric field between the electrodes. The rigorous calculation of the electric field (not included in the theory), Eq. 3.25 and Figure 3.13, show that the field at the resistor center is 2.2 times less than the infinite parallel plate value assumed in the theory. This value is comparable to the discrepancy

mentioned above. Clearly, the uniform electric field approximation is the largest contributing factor to poor accuracy in the theory. Another factor is the presence of heat sinks close to the interaction region: windows, wires and glass, which will perturb the laser induced temperature field. The effects of heat sinks on the signal in thermal lens measurements have been modeled previously [26]. Such heat sinks would damp the temperature modulation between the electrodes, decreasing the signal. Finally, the solvent parameters input into the program were those obtained at 20°C while experiments were carried out in a warm lab at ~ 25 to 30 °C. The temperature coefficient of viscosity, Eq. 3.29, decreases with the square of the absolute temperature; a 2-7% decrease in the signal would be expected because of this. Detection should be carried out at cool temperatures for better sensitivity.

The model could give reasonable accuracy (±50%) if all of these factors were taken into account. Generally, calibration would be used in any real detector. A calibration was done to assess the sensitivity of the technique. An electrode separation of 50-μm was used with a chopping frequency of 10-Hz. Solutions were made in nanopure H_2O, 0.01M NaCl with Fast Green dye concentrations ranging from 1.0×10^{-8}M to 4.0×10^{-5}M. Two 0.01-M NaCl blank solutions were prepared, one in H_2O and the other in D_2O. The noise measured during the calibration was 3.6 times the shot noise limit. The calibration curve, Figure 3.19a, was linear (R= 0.9998, n=14) from the one point detection limit (3-σ) of 6.9×10^{-9} M, up to 1.0×10^{-5} M dye concentration. The linear dynamic range was over three orders of magnitude.

The lowest order of magnitude of the calibration curve is illustrated in Figure 3.19b. The blank signal in H_2O was not zero, even though the laser beam (ω=10-μm) passed through the center of the electrodes. This
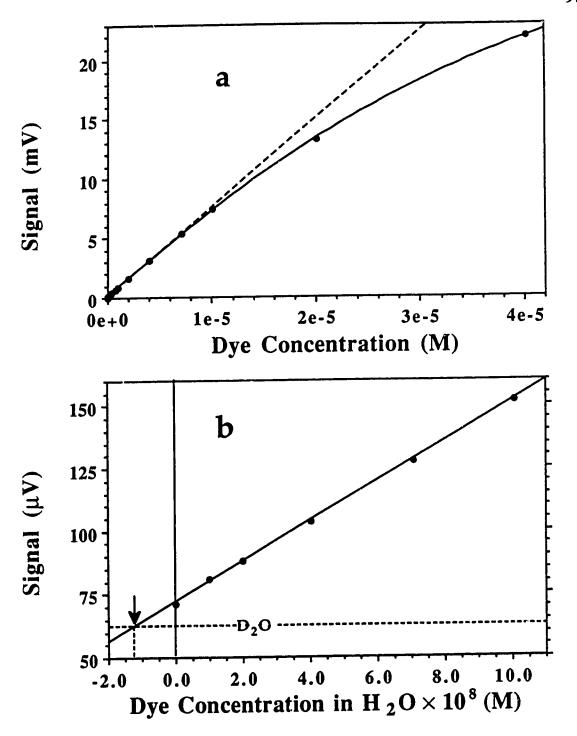
Figure 3.19 (a) Calibration curve in H_2O has linear dynamic range of > three orders of magnitude. (b) expanded curve shows difference in signal between H_2O and D_2O. Intercept marked by arrow is used to calculate the difference in absorbance between the two solvents at 632.8-nm.

background signal has two origins: residual light scatter on the electrodes and the finite absorbance of H_2O at 632.8-nm. To determine the latter contribution, the signal in H_2O is compared to the signal in D_2O. Although the light scatter background for the two solvents should be similar, the absorbance of D_2O is more than an order of magnitude less than that of H_2O at 632.8-nm. The absorbance of H_2O in the red is associated with overtones of infrared transitions [27], which explains the weakness of the absorbance (the resultant green color of H_2O is only visible to the eye in a long path length) and the change in absorbance with isotopic substitution that would not be expected for electronic transitions in general. The difference in signal between the H_2O and D_2O blank solutions can be converted to an absorptivity difference by using the dye as a standard. In effect, the dye acts as the standard for the standard additions method of quantitation [28]. The dye/H_2O calibration line intercepts the D_2O signal level at a negative dye concentration of 1.31×10^{-8} M. Thus, the absorbance of this concentration of dye should be interpreted as the difference in absorbance between H_2O and D_2O at 632.8-nm. The experimental value for this difference, $\Delta \varepsilon C(H_2O\text{-}D_2O) = 1.3 \times 10^{-3} \text{cm}^{-1}$, is in excellent agreement with the literature value of $1.22 \times 10^{-3} \text{cm}^{-1}$ determined using pulsed photoacoustic spectroscopy in a long path length cell [27].

The calibration curve shows negative deviation at dye concentrations greater than 1.0×10^{-5} M. The source of this negative deviation is a change in the spectrum of the dye due to self-association and a decrease in the laser power reaching the electrodes because of absorbance of the beam through the 260-μm distance to the electrodes. This phenomenon was observed in the preliminary report of TMEC [4]. As an applied absorbance detector in capillaries, the linear dynamic range would be extended on the high

concentration end by an order of magnitude or more by the necessary reduction in the distance from the glass (or silica) to the electrode axis.

The absorptivity-concentration product (ϵC) detection limit for the calibration was 7.2×10^{-4} cm^{-1}, made over a path length given by the diameter of the wire, 76-μm. This detection limit is less than the absorbance of pure water and was made in a volume of only 230-pL, conservatively estimated by the full resistor volume. On the basis of the path length, the absorbance detection limit is 5.5×10^{-6}. The amount of analyte between the electrodes at the detection limit is only 1.6-attomoles or about a million molecules. This excellent sensitivity has been achieved using a very modest and inexpensive 5-mW laser. An increase in the laser power will result in a proportional increase in the sensitivity and decrease in the detection limit. For example, a 250-mW laser could produce absorbance detection limits of 1×10^{-7} for aqueous samples, a significant improvement in the state of the art.

3.5 CONCLUSIONS

Thermal modulation of electrical conductivity is a very sensitive small volume absorbance measurement technique. It is a true small volume technique in the sense that the sensitivity increases with a decrease in the volume. The lower volume limit to this trend is only limited by the practical spot size that one can obtain with the laser and the dimensions of the microelectrodes that can be incorporated into the system. To attest to the sensitivity of the method, the absorbance of water was measured in a 230-pL volume by a calibration method and found to be ϵC=1.3×10^{-3}cm^{-1} at 633-nm, comparable to the literature value. These measurements were made with a low power 5-mW He-Ne laser. If required, the sensitivity could be improved

by at least an order of magnitude by increasing the laser power proportionately.

The model that was developed to describe the TMEC signal was verified experimentally with respect to the detector dimensions, current, laser power, modulation frequency and physical properties of the solvent. The greatest sensitivity can be obtained with small detector dimensions, high current, high laser power, and low modulation frequencies. Higher spatial resolution for imaging is possible at high modulation frequencies, but at the expense of reduced signal-to noise. Increased sensitivity could be gained in suitable aqueous mixtures with other solvents, in which strong A-B type attractive interactions increase the characteristic viscous energy, E^*, giving a larger thermal coefficient of viscosity. Unlike other calorimetric techniques, TMEC shows particular promise for absorbance measurements in water.

The theory was tested for its accuracy in predicting the amplitude of the signal. The best agreement with experiment was found at small electrode separations, where the measured signal was 2 to 3 times smaller than the predicted signal. Most of this discrepancy was due to the inhomogeneous electric field strength between the electrodes. A more complete theory would include 3-dimensional modeling of the electric field between the electrodes. A final refining of the theory would consider heat sinks close to the detector region. These additions to the theory might allow absolute absorbance measurements to be made without the need for calibration.

Any future work into this technique should be directed toward detector development inside capillaries for liquid chromatographic or electrophoretic separations. The challenge here is in the placement of the microelectrodes

into the capillary for on-column detection or the development of a post-column detector cell in which dead volume is kept smaller than the anticipated peak volumes. Conductivity detection in electrophoresis has been performed inside capillaries in which 10-μm platinum wire was inserted into holes that were punched into the capillary with a pulsed CO_2 laser [29]. Private communication with the authors revealed that the task was not trivial and that axial alignment of the electrodes was difficult. Such an arrangement though, with a laser aligned to intersect the volume between the electrodes, should facilitate simultaneous absorbance and conductivity detection.

Other future work also would involve the study of alternate solvent systems, designed to enhance the temperature coefficient of viscosity, and appropriate buffer systems that could further enhance the coefficient of conductivity through the thermal production of ions. This latter possibility was discussed in Chapter 2.
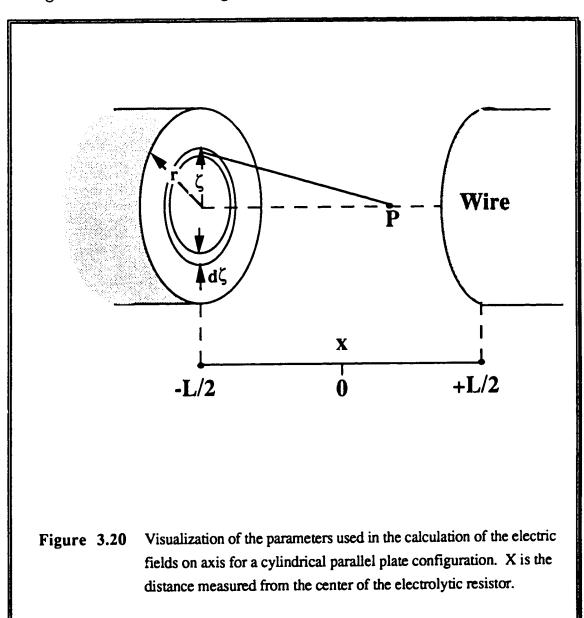
REFERENCES

(1) G.H. Brilmyer and A.J. Bard, *Anal. Chem.* **52**, 685 (1980).

(2) D. Betteridge and A.J. Bard, *CRC Crit. Rev. Anal. Chem.* **14**, 267 (1984).

(3) N. J. Dovichi, *CRC Crit. Rev. Anal. Chem.* **17**, 357 (1987).

(4) R. McLaren and N.J. Dovichi, *Anal. Chem.* **60**, 730 (1988).

(5) T.G. Nolan and N.J. Dovichi, *Anal. Chem.* **59**, 2801 (1987).

(6) K.C. Waldron, S. Wu, C.W. Earle, H.R. Harke and N.J. Dovichi, *Electrophoresis.* **11**, 777 (1990).

(7) A. Adamson, *A Textbook of Physical Chemistry* , 2nd edition, Academic Press, New York (1979).

(8) A.J. Twarowski and D.S. Kliger, *Chem. Phys.* **50**, 253 (1977).

(9) *CRC Handbook of Chemistry and Physics,* 63rd Edition; R.C. Weast, Ed., CRC Press: Boca Raton, Florida (1982). Integral #532

(10) I.S. Gradshteyn and I.M. Ryzhik, *Tables of Integrals ,Series and Products* , 4th edition, Academic Press, New York (1965) Definition 3.383.# 1.

(11) A. Arfken, *Mathematical Methods for Physicists,* 2nd edition, Academic Press, New York (1970).

(12) E.W. Swokowski, *Calculus : A First Course* , 2nd edition, Prindle, Weber & Schmidt, Belmont, California (1979).

(13) M. Schwartz, *Information Transmission, Modulation, and Noise,* 2nd edition, McGraw-Hill, New York (1970).

(14) *CRC Handbook of Chemistry and Physics,* 63rd Edition; R.C. Weast, Ed., CRC Press: Boca Raton, Florida (1982).

(15) *Journal of Physical and Chemical Reference Data.* **11**, D.R. Lide, Ed., (1982).

(16) *Journal of Physical and Chemical Reference Data.* **13**, D.R. Lide, Ed., (1984).

(17) B.C. Burdett, in *Aggregation Processes in Solution* , E. Wyn-Jones and J. Gormally , Eds., Elsevier Scientific Publishing Co., New York (1983).

(18) G.H. Horlick, *Electronics For Scientists: Course Notes* , University of Alberta (1987)

(19) A.F. Kip, *Fundamentals of Electricity and Magnetism* ,2nd edition, McGraw-Hill, New York (1969).

(20) P. Horowitz and W. Hill, *"The Art of Electronics"*, Cambridge University Press, Cambridge (1980).

(21) *Instruction and Maitnenance Manual : Ithaco Model 3961 Lock-In Amplifier*,Ithaco Inc., 735 W-Clinton St., New York (1985).

(22) N.J. Dovichi, T. J. Nolan and W.A. Weimer, *Anal. Chem.* **56**, 1700 (1984).

(23) T. J. Nolan, W.A. Weimer and N.J. Dovichi, *Anal. Chem.* **56**, 1704 (1984).

(24) *"Fundamental Formulas of Physics"* , Volume 2, D.H. Menzel, Ed., Dover, New York (1960).

(25) *CRC Handbook of Chemistry and Physics*, 43rd Edition; C.D. Hodgman, Ed., Chemical Rubber Publishing Co.: Cleveland, Ohio (1962).

(26) S. Wu and N.J. Dovichi, *J. Appl. Phys.* **67**, 1170 (1990).

(27) A.C. Tam, C.K.N. Patel, *Applied Optics.* **18**, 3348 (1979).

(28) D.C. Harris, *"Quantitative Chemical Analysis"*, 2nd edition, W.H.Freeman and Company, New York (1987).

(29) X.H. Huang, T.K. Pang, M.J. Gordon and R.N. Zare, *Anal. Chem.* **59**, 2747 (1987).

APPENDIX A

This appendix presents a derivation for the magnitude of the electric field at a point on the axis of a cylindrical parallel plate capacitor. The calculation involves summing up all the contributions to the field at point P, in Figure 3.20, due to all charge on the surface of the electrode faces.

Figure 3.20 Visualization of the parameters used in the calculation of the electric fields on axis for a cylindrical parallel plate configuration. X is the distance measured from the center of the electrolytic resistor.

A charge density of $+\sigma$ exists on the left electrode surface and one assumes an equal and opposite charge density on the right electrode surface. An incremental electric field vector, $\vec{dE}$, at point P, is calculated from Coulombs law [19],

$$d\vec{E} = \frac{1}{4\pi K\varepsilon_o} \frac{dq}{l^2} \vec{l}$$

(3.30)

where K is the dielectric constant of the material between the electrodes, ε_o is the permittivity of free space, dq is the element of surface charge a distance l away from point P and $\vec{l}$ is a vector pointing along the line from the surface charge to point P. When calculating the field on axis due to a thin circular ring of surface charge on an electrode face, the vector components perpendicular to the x axis can be ignored due to cancellation by symmetry. The field at P, due to a charged ring of radius ζ and thickness $d\zeta$ on the left electrode face, is given by

$$d\vec{E} = \frac{1}{4\pi K\varepsilon_o} \frac{2\pi\zeta \, d\zeta \, \sigma}{\left((L/2+x)^2+\zeta^2\right)} \frac{(L/2+x)}{\sqrt{(L/2+x)^2+\zeta^2}} \vec{x} = \frac{(L/2+x)\sigma}{2K\varepsilon_o} \frac{\zeta \, d\zeta}{\left((L/2+x)^2+\zeta^2\right)^{3/2}} \vec{x}$$

(3.31)

The total field at point P due to the left electrode is obtained by integrating the above expression with respect to ζ.

$$d\vec{E}_{left} = \frac{(L/2+x)\sigma \vec{x}}{2K\varepsilon_o} \int_0^r \frac{\zeta}{\left((L/2+x)^2+\zeta^2\right)^{3/2}} \, d\zeta$$

(3.32)

With a single substitution, $y = \zeta^2$, the integral is solved to yield

$$\vec{E}_{left} = \frac{\sigma \vec{x}}{2K\varepsilon_o} \left(1 - \left[\frac{1}{1+[r/(L/2+x)]^2}\right]^{1/2}\right)$$

(3.33)

The field at P due to charge on the right electrode can be calculated in a similar fashion and will add to the field calculated above. It is convenient to use the fractional distance between the electrodes, β = x/L, and to calculate the field for a particular ratio, R, of the wire radius to the electrode separation, R = r/L. The final expression for the magnitude of the field at P using these substitutions is

$$E(\beta,R) = \frac{\sigma}{K\varepsilon_0}\left[1 - 1/2\left(\left[\frac{1}{1+[R/(0.5+\beta)]^2}\right]^{1/2} + \left[\frac{1}{1+[R/(0.5-\beta)]^2}\right]^{1/2}\right)\right]$$

(3.34)

CHAPTER 4

SPATIALLY RESOLVED DIFFERENTIAL

RESISTIVITY MEASUREMENTS OF

SUPERCONDUCTORS

4.1 INTRODUCTION[1]

The measurement of electrical resistance is an important method for the characterization of the physical properties of superconducting materials, and was used for the discovery of the superconductive phemomena itself [1]. A sharp decrease in the resistance of the sample occurs at the transition temperature, T_c. For polycrystalline materials, the sample does not always achieve zero resistance below a transition temperature because of the presence of impurities, multiple superconducting phases, or excess intergranular resistance. For such samples, the resistance itself is not of primary interest. Instead, the change in resistance with temperature, dR/dT, is of interest because a large value of dR/dT identifies possible superconducting transitions within the sample. Of course, a resistive transition itself is not proof of superconductivity and must be supplemented by other physical measurements such as the magnetic susceptibility $\chi(T)$. However, measurements of the Meissner effect, like resistance measurements, are associated with the bulk specimen. They do not give information on the spatial distribution of the superconductive properties of the sample.

Localized measurements on high temperature superconductors are important for a fundamental understanding of the processes responsible for spatial inhomogeneities and for the development of useful superconducting devices. For example, low temperature scanning electron microscopy has been used to image the physical properties of low temperature

---

1   A version of this chapter has been previously published :
     R. McLaren, N.J. Dovichi, *J. Appl. Phys.* **68**, 4882 (1990).

superconducting tunnel junctions and microbridges [2]. More recently, the same technique has directly shown the limitation of critical current densities by individual grain boundaries in $YBa_2Cu_3O_7$ thin films [3]. In a different study, the directional anisotropies in the thermal diffusivity of single crystal $Bi_2Sr_2CaCu_2O_8$ and polycrystalline materials were measured and imaged using a photothermal technique [4].

In this chapter, a new technique, Photothermal Conductivity Modulation (PCM), is presented for measuring the differential resistivity, $d\rho/dT$, of bulk high-T_c superconducting samples. Large values of $d\rho/dT$ are evidence of resistive transitions in the sample. A four probe ac method is used to measure the resistance of the sample. A laser beam is modulated in the low audio frequency range and focused onto the superconductor between the two inner leads. The laser acts as a thermal source, modulating the temperature of a localized region on the sample. Any variation in resistivity with temperature in the region of the focused beam will result in a modulation of the bulk resistance of the sample. The ac component induced upon the resistance signal is proportional to $d\rho/dT$. A distinction between resistance, R, and resistivity, ρ, has been made here. Resistance is a bulk property of a sample dependent on electrode configuration, while resistivity is an intrinsic property of the material. Since localized (as opposed to bulk) measurements of inhomogeneous materials are made with this method, it is appropriate to label the property being measured as differential resistivity as opposed to differential resistance.

With this technique, one can perform two types of measurements. Using a large spot size and low modulation frequencies, the thermal modulation signal can be recorded as a function of temperature. This

procedure will generate an approximate differential resistance spectrum representative of the bulk specimen, dR/dT (T). Alternatively, high modulation frequencies and a tightly focused beam can be used to image the differential resistivity of the sample, $d\rho$ /dT(x,y). To generate such images, the modulated signal is recorded as the laser beam rasters across the sample at a constant temperature, usually at the peak of a resistive transition. The impetus in this imaging experiment is to illuminate the nature of, and the source of inhomogeneities in, high temperature superconductors. In this Chapter, the thermal diffusivity of a Bi-Sr-Ca-Cu-O sample is also estimated.

The thermal modulation technique used for these measurements is similar to that used previously for making sensitive absorbance measurements in small volumes of aqueous solutions, laser-induced thermal modulation of electrical conductivity (TMEC) [5,6]. A description of that technique was given in Chapters 2 and 3. In solution measurements, a physical property of the solvent, the temperature coefficient of viscosity, is assumed to be constant and variations in the absorbance of the analyte are measured. In contrast, when making measurements on superconductors, the absorptivity of the sample is assumed constant and variations in the temperature coefficient of resistance are measured.

4.2 SIGNALS

Before looking at methods of measuring the thermally modulated resistance, let's consider the voltage signals in the experiment. The ac-current, I, at frequency F, induces a time dependent voltage, $V_F(t)$, in the sample.

$$V_F(t) = IR \cos (2\pi Ft) \qquad (4.1)$$

Assuming sinusoidal modulation for simplicity, the laser induced heating modulates the amplitude of this carrier wave at frequency, f, in the following manner,

$$V(t) = [1 + A_f \cos(2\pi ft)] \, V_F(t) \qquad (4.2)$$

A_f is the modulation factor responsible for the thermal signal. A simple description of this factor can be given in the approximation of a homogeneous sample, homogeneous current density, fast optical modulation and a relatively thick sample[2],

$$A_f = \frac{1}{4v\rho} \frac{d\rho}{dT} \frac{P(1-r)}{fC_p} \qquad (4.3)$$

where v is the volume of sample between the inner leads, ρ is the resistivity of the sample, P is the incident power, r is the reflectance from the surface and C_p is the heat capacity of the sample.

The time dependent voltage takes on the following form by substitution of Eq. 4.1 into Eq.4.2,
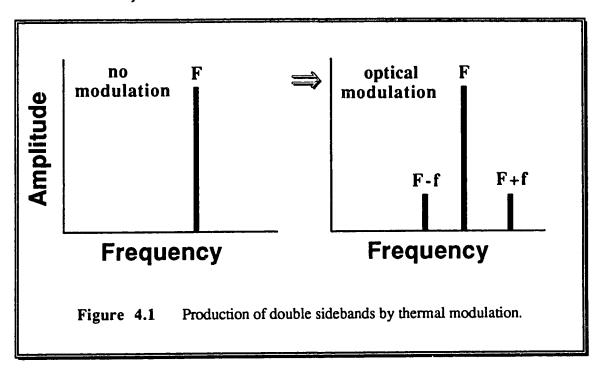
$$V(t) = IR \cos(2\pi Ft) + 1/2 \, IRA_f [\cos(2\pi[F+f]t) + \cos(2\pi[F-f]t)] \qquad (4.4)$$

The modulation produces two sidebands at frequencies, F+f and F-f, Figure 4.2. These sidebands hold the thermal modulation information, while the signal amplitude at the carrier frequency gives the resistance of the sample. The amplitude of the thermal modulation signal is

$$\Delta V_{rms} = \frac{IR}{8v\rho} \frac{d\rho}{dT} \frac{P(1-r)}{fC_p} \qquad (4.5)$$

---

2 The derivation of this modulation factor is similar to that given for the square wave response in Chapter 3, at the small spot limit.

again with the assumptions mentioned above. The dynamics of heat flow and the thermal conductivity of the sample become more important as one decreases the modulation frequency and sample thickness. Huebener et al. have presented a more detailed description of the thermal dynamics in thin films induced by an electron beam source [10].

Figure 4.1   Production of double sidebands by thermal modulation.

A few observations can be made from Eq.4.5. First, the signal is proportional to $d\rho/dT$. This relationship is the primary reason for applying this technique to superconductors. The signal is proportional to the laser power although, in general, one wants to use as low a power as possible to avoid thermal broadening of the transition peaks. Thermal broadening results from temperature gradients present in the sample. Also, smaller samples generate proportionately larger signals for a given current through the sample. This fact is due to the larger average temperature rise that is possible in a smaller volume for constant heat input. In this simple

description, the signal is inversely proportional to the frequency. Low modulation frequencies generate large signals, albeit at a cost in terms of spatial resolution. The spatial resolution can be characterized by the dynamic thermal healing length (thermal diffusion length), η_ω,

$$\eta_\omega = \left(\frac{2D}{\omega}\right)^{1/2} = \left(\frac{D}{\pi f}\right)^{1/2} \tag{4.6}$$
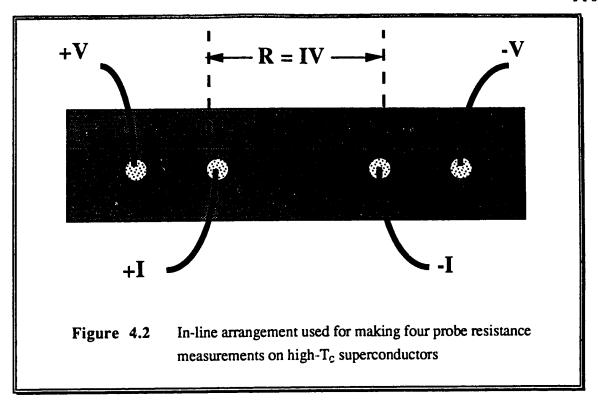
where $D=k/\rho C_p$ is the thermal diffusivity of the material with thermal conductivity k and ω is the angular frequency of the modulation [2]. High resolution microscopy requires high modulation frequencies.

4.3 EXPERIMENTAL

4.3.1 Resistance Measurements

Standard resistance measurements require the use of two leads in which each lead both carries current and measures the voltage drop across the sample. The leads themselves, with resistances of hundreds of microhms to tens of milliohms, have a negligible voltage drop across them compared to the voltage drop across the resistor being measured. Ceramic superconducting samples of millimeter dimensions typically have resistances in the milliohm range. The voltage drop across a lead is not negligible in this case, and a four-probe technique [7] is used to ensure accuracy in these low resistance measurements.

In this study, four leads were connected to the sample using an in-line arrangement, Figure 4.1. An ac current passes through the sample using the inner two leads and the voltage drop is measured using the outer two leads, or visa-versa.

Figure 4.2 In-line arrangement used for making four probe resistance measurements on high-T_c superconductors
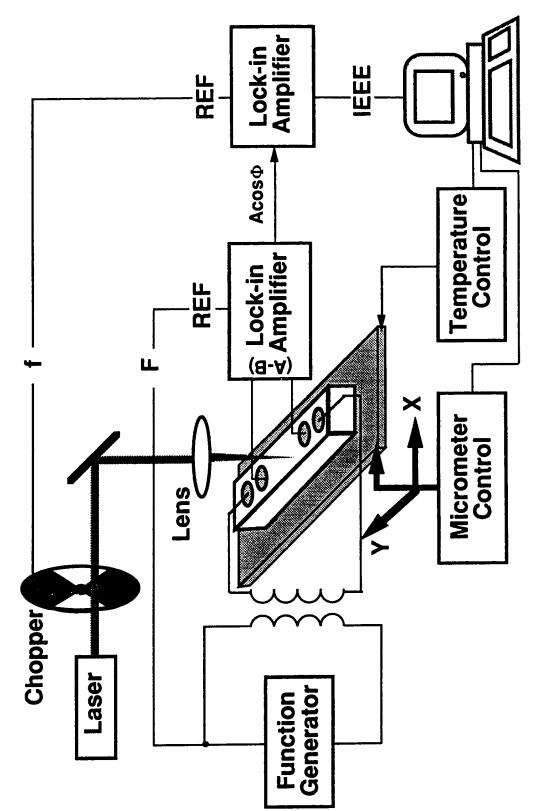
Good electrical contact to the samples was made by a process of trial and error, . . . mostly error. The following procedure gave reasonably consistent connections. Contacts to the samples were made by sputtering gold over teflon masked samples to an estimated thickness of 100-nm. Very low resistance gold contacts on superconductors have been reported in the literature [8]. The masks were made by burning 0.2-0.5mm diameter holes into colored teflon tape using a focused Ar^+ laser (488-nm). Thin copper wire (75-μm) was connected to the gold contacts using minimal amounts of two component silver epoxy (Epo-Tek, Billerica, Mass.) and a 4-hour curing at 90°C. Contact resistances of 5 to 100-Ω, measured with a simple analog meter, were found to give good results. Contact resistances larger than this had poor noise characteristics and gave ambiguous resistive data. The quality of the contact could be determined by measuring the phase difference between the input current and the sample voltage in the audio frequency range. A pure

resistor has a zero phase lag between the current and the voltage. Phase differences of -5° to +5° in this frequency range were indicative of good electrical connections.
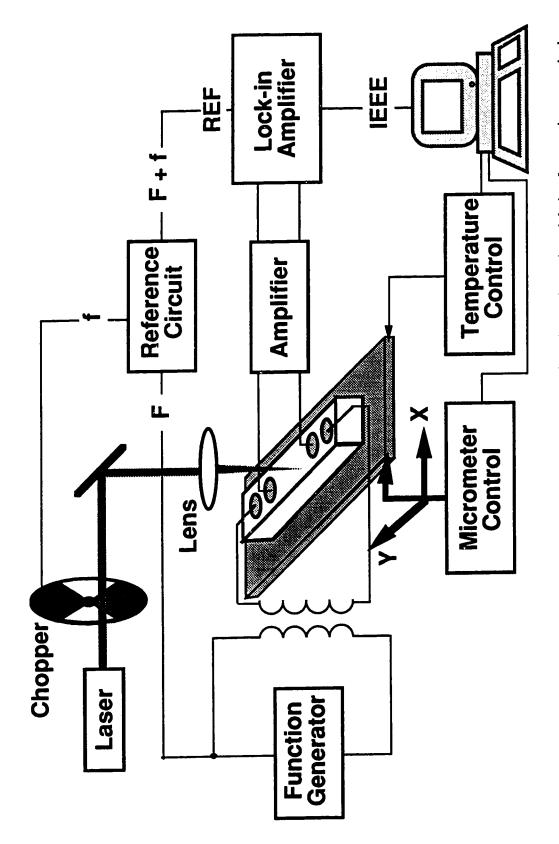
4.3.3 Thermal Modulation Measurements

The thermally modulated resistance signal, Eq. 4.5, is measured in one of two ways. The first method, requiring the use of two lock-in amplifiers, Figure 4.3, is suitable for low modulation frequencies (10-100-Hz). A helium cadmium laser (15-mW, 442-nm) is mechanically chopped at frequency, f, and focused onto the sample. An ac current at higher frequency (0.5-5.0-kHz) , F, passes through the sample. The first of two 2-phase lock-in amplifiers, operated with a 1-msec time constant, demodulates the voltage across the sample at frequency F. The amplitude measured by this first lock-in is related to the resistance of the sample. This resistance is modulated by the laser induced heating. A fast analog output from the first lock-in feeds the second lock-in amplifier, operated with a longer time constant, typically 300-msec. This signal is subsequently demodulated at frequency f. The output of the second lock-in amplifier is the thermally modulated signal. Both the amplitude and phase of the modulation can be measured. The amplitude gives information on $d\rho/dT$ and the phase is related to the thermal diffusivity of the material. With this detection arrangement, three signals are recorded simultaneously: resistance, modulation amplitude, and modulation phase.

The second method for measuring the thermal signal requires the use of single sideband detection [11], Figure 4.4. This method is suitable for high modulation frequencies but has the disadvantage that the resistance cannot be

Figure 4.3 Experimental schematic using two lock-ins. F and f are the carrier and modulation frequencies respectively.

Figure 4.4 Experimental schematic using sideband detection. F and f are the carrier and modulation frequencies respectively.

measured simultaneously. An active ac amplifier or an audio transformer amplifies the signal before input to the lock-in amplifier. The signal is then demodulated, either at the upper or lower sideband frequency. Appendix B at the end of this chapter illustrates the circuit used to generate the reference signal for the lock-in amplifier.

The cooling system is an MMR Technologies micro-miniature refrigerator with 300-mW cooling power and a programmable temperature controller. Cooling is achieved by a Joule-Thompson expansion of high pressure N_2 gas through fine capillaries in a vacuum surrounded cold finger. Liquefied N_2 is produced below the cold finger, which can support samples of 1-cm×1-cm dimension. By attaching a vacuum to the capillary outlet, temperatures as low as 70-K can be reached. Samples are mounted on the cold finger with a thin layer of thermal compound. The laser beam enters the refrigerator through a sapphire window.

For this study, the focusing lens was mounted on a three axis translation stage system equipped with programmable linear actuators, capable of 0.1-μm movements. This arrangement was adequate for scans over areas less than 1-mm×1-mm because the laser spot movement correlated accurately with the lens movement to within 5% over a 2-mm range. For movements over the full area of the cold finger, the refrigerator itself can be mounted on the translational stage system while the laser spot is held stationary. An 80286-microprocessor based PC with IEEE-488 interface performs simultaneous temperature control and measurement, and data collection from the two lock-in amplifiers.

115

The images presented in this study were collected and plotted with software written for a scanning laser microscope [24]. A *Stride 440* microcomputer with IEEE-488 interface was used to execute the software. Subsequent to this report, alternate software was written by the author for collecting image data. This will be discussed in Chapter 5.

4.3.4 Sample Synthesis

Several samples of the Bi-Sr-Ca-Cu-O class superconductors were synthesized. The raw materials were Bi_2O_3, $SrCO_3$, $CaCO_3$, and CuO (Johnson Matthey, puratronic). The powders were weighed to give a 4:3:3:6 respective metal atom ratio. The powders were then mixed and ground with a mortar. The powder mixture was fired in air inside a muffle furnace at 850-865°C for 92-hours, reground, pelletized in a press, and annealed at 850-875°C for a further 28-hours. The sample was then oven cooled to room temperature.

The particular metal atom ratio used here was reported to help enrich the sample with the 2223 superconducting phase relative to the 2212 phase [12]. It is now well known that substitutions of Pb and Sb for Bi in a 2:2:2:3 mixture produce samples with predominantly 2223 phase material [13-17].

Dr. W.A. Weimer of the China Lake Naval Weapons Research Lab kindly provided a polycrystalline $YBa_2Cu_3O_{7-x}$ sample for use in this study.

4.4 RESULTS AND DISCUSSION

Figure 4.5 shows results for a polycrystalline sample of $YBa_2Cu_3O_{7-x}$ of dimensions 5-mm×2-mm×1-mm. The resistance (Figs. a, c) was measured using a 150-Hz carrier frequency. The modulation amplitude (Figs. b, d) was
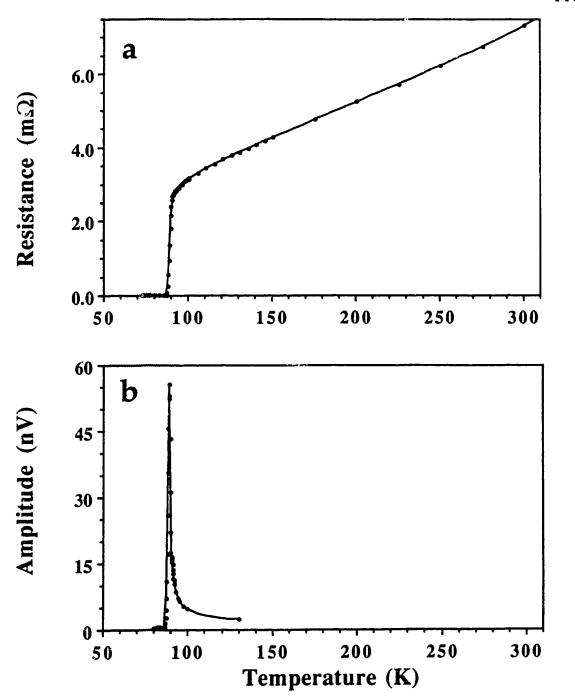
Figure 4.5 (a) Measured resistance of a polycrystalline sample of $YBa_2Cu_3O_{7-\delta}$.

(b) Modulation amplitude measured using a 10-Hz laser beam loosely focused between the inner electrical leads. Solid lines are for clarity.
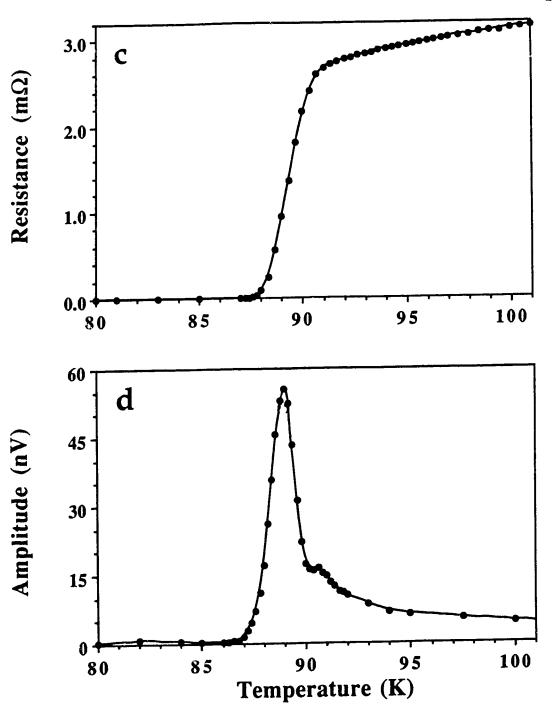
Figure 4.5 (c) & (d) Transition region of Fig. 4.5a and 4.5b respectively. Solid lines are for clarity only.

recorded using a two lock-in scheme with F=150-Hz and f=10-Hz. A 1-mm spot size 15-mW beam was used to record a thermal modulation signal that is representative of the bulk sample. The resistance of the sample increases linearly with temperature above the transition, $T_c \approx 88K$. The modulation amplitude exhibits a peak at approximately the same temperature as the resistive transition. The amplitude peak actually appears at a slightly lower temperature than the resistive transition because of the local steady state (dc) temperature rise induced by the laser. This temperature shift, approximately -1K for the 15-mW incident power, decreases when the laser power is lowered. The modulation amplitude above the transition falls slowly to a constant level that reflects the metallic like behavior of the resistance in the normal state of the material.

The zero amplitude signal below T_c suggests the absence of a significant nonbolometric response of the material to the 442-nm radiation. Nonbolometric responses, such as quasiparticle formation, allow fast infrared detection [18,19]. Previously, the absence of a nonbolometric response to 633-nm and 1.06-μm radiation in $YBa_2Cu_3O_7$ thin films was reported [20]. This is contrasted with the report of fast optical detection of 1.06-μm radiation via a nonbolometric response for a c-axis oriented $YBa_2Cu_3O_7$ crystalline thin film [19].

Figure 4.6 presents the simultaneously recorded (a) thermal modulation amplitude, (b) numerically differentiated resistance, (c) resistance and (d) modulation phase of a sample of nominal composition $Bi_4Sr_3Ca_3Cu_6O_{18-x}$. The laser was loosely focused between the voltage leads. Three transitions can be observed in the modulated signal, a broad transition centered at 72-K and two minor transitions at 105 K and 116 K (inset).
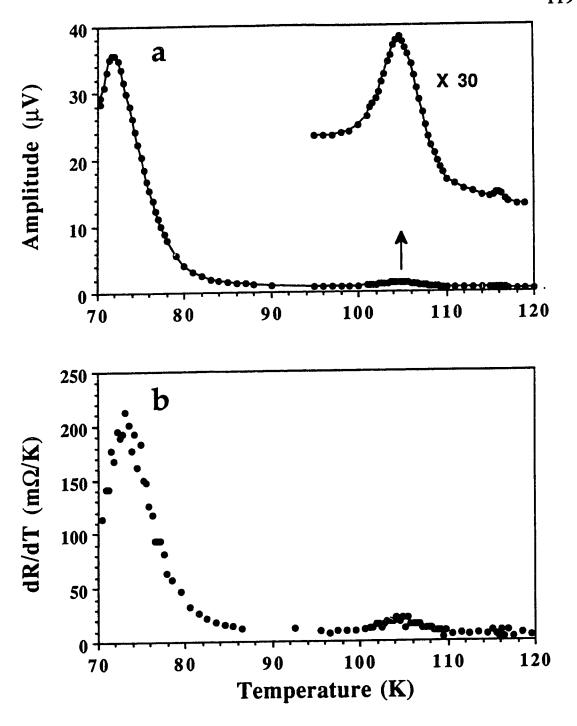
Figure 4.6 Comparison between the thermal modulation amplitude (a) and the numerically differentiated bulk resistance (b) of a sample of nominal composition $Bi_4Sr_3Ca_3Cu_6O_{18}$.
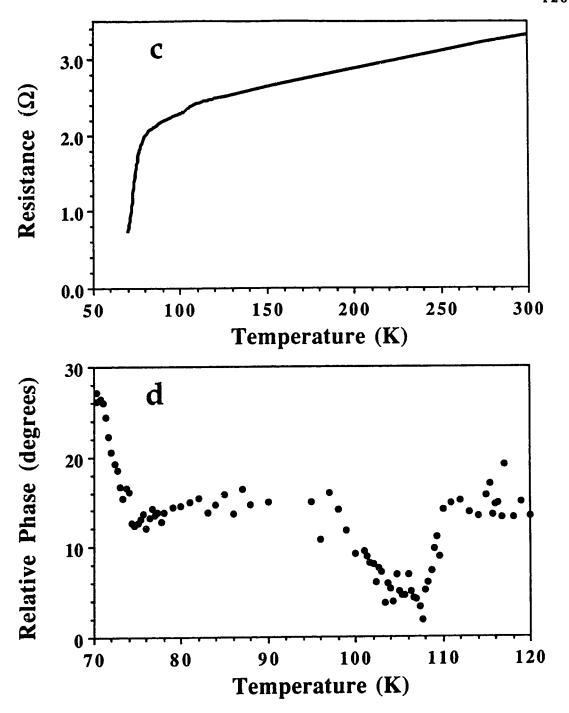
Figure 4.6   Resistance (c) and thermal modulation phase (d) of $Bi_4Sr_3Ca_3Cu_6O_{18}$. The data in (a),(c) and (d) were recorded simultaneously using a two lock-in signal detection scheme.

Multiple structural superconducting phases in the Bi-Sr-Ca-Cu-O system are well known and can be represented by the general formula $Bi_2Sr_2Ca_{n-1}Cu_nO_{2n+4}$ where n is the number of adjacent Cu-O layers in the crystal structure. The transition temperatures increase with n and have been reported as T_c = 60±20 K, 82±8 K and 107±3-K for the n = 1, 2, 3 members of the series respectively [21,22]. The 72-K transition is very broad and may not be due to a pure phase. The onset of the transition at $\approx$ 90K may suggest the presence of the 2212 phase. The slow drop in resistance below this temperature, Fig. 4.6c, is characteristic of the Bi-Sr-Ca-Cu-O system. This sample does not show zero resistance above 70-K, the lowest temperature possible with the refrigeration system used. The transition at 105 K is assigned to the presence of the 2223 phase. The transition at 116 K may be due to a higher order phase, n > 3, and may be responsible for reports of superconductivity onset near 120K in this system using magnetic susceptibility measurements [23].

The numerically differentiated resistance data, Fig. 4.6b, qualitatively matches the thermal modulation spectrum. However, the relative intensity of the two lowest transitions in the thermally modulated data (H_{72-K}/H_{105-K}), measured by peak heights, H, is greater than the corresponding ratio in the numerically differentiated data. This trend would be consistent with a gradual decrease in the heat capacity of the material from 105-K to 72-K. Interestingly, the transition at 116K in the amplitude spectrum cannot be detected in the differential resistance spectrum because of noise. The thermally modulated signal shows a much higher signal-to-noise ratio when compared to the numerically differentiated data, in part due to the longer

time constant of the second lock-in amplifier compared to the first lock-in. It is also partly due to the inherently noisy process of numerical differentiation.

Shifts in the signal phase are observed at the temperature of the two main resistive transitions, Fig. 4.6d, at 105-K and 72-K. The phase of the PCM signal is expected to be related to heat flow in the sample and the thermal diffusivity of the material. The phase will depend on several other parameters such as sample geometry, modulation frequency, temperature, spot-size, distance to inhomogeneous features, etc., and will not be modeled here. The shifts shown in the diagram above are believed to be related to the steady state temperature field near the laser beam spot. As the temperature is scanned, different regions of the sample in the heated region come into 'resonance' as the local temperature of that region matches the transition temperature of the material. The distance between the beam spot and the signal generating region changes as the temperature of the bulk sample is scanned through the resistive transition. It is this change in *distance* that gives rise to phase shifts. In a practical sense, the signal phase could be used as an alternate method for imaging inhomogeneities on the sample.

Figure 4.7 and Figure 4.8 present images of the thermal modulation amplitude (a) and phase (b) of a 1 × 1-mm area between the electrodes on the Bi-Sr-Ca-Cu-O sample. Modulation frequencies of 50 and 400-Hz were used respectively to record the data. The images were collected using 20-μm pixels at 72K, the temperature of the main transition. The current path was along the center of the images, parallel to the y-axis. A single feature that appears to be on the current path dominates all four images in Figs. 4.7 and 4.8. The width of the feature decreases at higher modulation frequencies, consistent with a decrease in the thermal diffusion length (Eq.4.6). Both optical
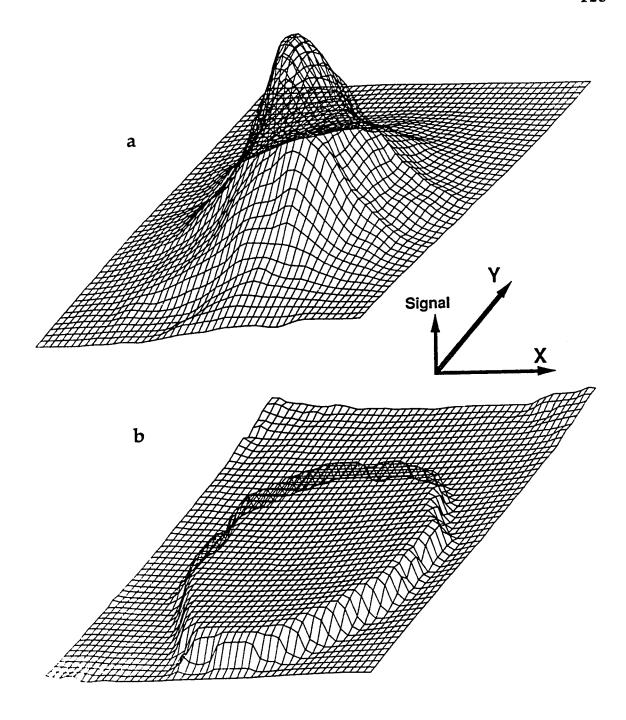
Figure 4.7   Thermal modulation images recorded simultaneously on the same Bi-Sr-Ca-Cu-O sample for the data in Fig. 4.6. The amplitude-(a) and phase-(b) images are that of a 1×1-mm area between the voltage leads at 72-K using 20-μm pixels and a 50-Hz modulation frequency. The current path is along the y-direction.
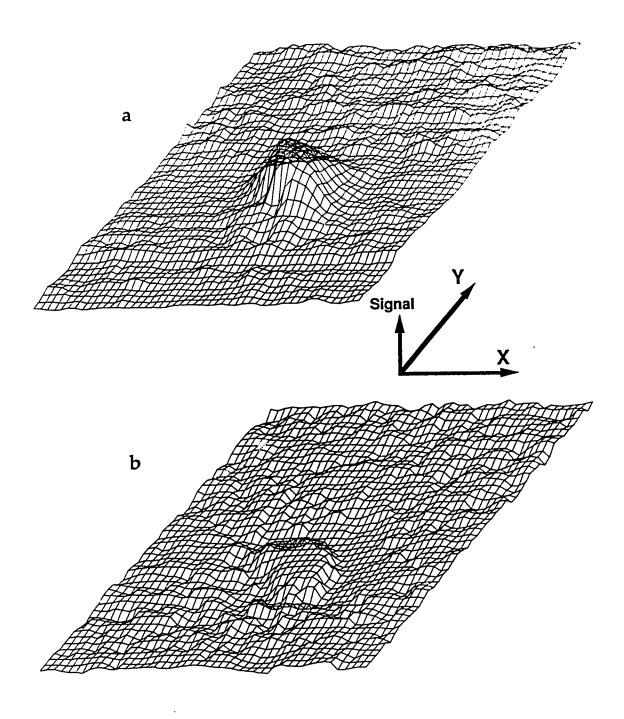
Figure 4.8   Amplitude (a) and phase (b) images of the same area as Fig. 4.7. The modulation frequency was increased to 400-Hz for these scans.
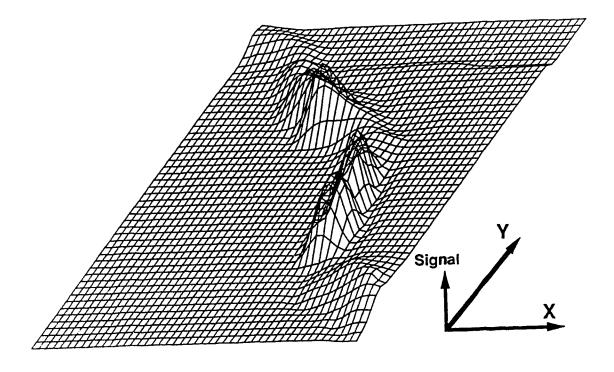
Figure 4.9 High resolution 100×100-μm amplitude scan of an area on the sample corresponding to the peak in Fig. 4.7 using 2-μm pixels and a 400-Hz modulation frequency. The material defect is readily observable.

microscopy and SEM identified the source of the feature as a material fault, a crack that ran diagonally across the full width of the sample. The signal appears to originate at the intersection of the defect line and the current path between the electrodes. A higher resolution image of a small area on top of the signal peak is presented in Figure 4.9. The modulation frequency used was the same as in Figure 4.8, 400-Hz, but the pixel size (2-μm) and image area (100×100-μm) were decreased by an order of magnitude, allowing more detail to be shown. Part of the defect can be seen running diagonally across the sample in this image. Surprisingly, this feature is visible with a much higher resolution than expected for this modulation frequency, ~10 to 15-μm. By no small coincidence, the spot size of the beam at the sample surface was estimated to be 13-μm. Based upon frequency dependent one-dimensional scans across the peak to be discussed shortly, the anticipated thermal resolution for this sample with a 400-Hz modulation frequency is 50-μm. The explanation for the increased resolution lies in the dependence of the signal on the reflectance of the material, Eq. 4.5. A decrease in the reflectivity of the material or increased surface roughness (nonspecular reflection) will give rise to more heat being deposited into the sample and subsequently a larger signal. The spot size of the laser beam ultimately limits this type of optical resolution. The defect in this sample was actually ~100-μm wide. The 15-μm feature seen in Figure 4.8 is believed to be one side of the defect only. The nonspecular reflectance that occurs as the beam scans over one side of the defect causes an increase in the signal.

The defect appears as a crack with partially melted shiny black material in the center under optical inspection. An SEM image of the sample in 'reverse angle', Plate 4.1, also clearly shows the crack. This material fault may
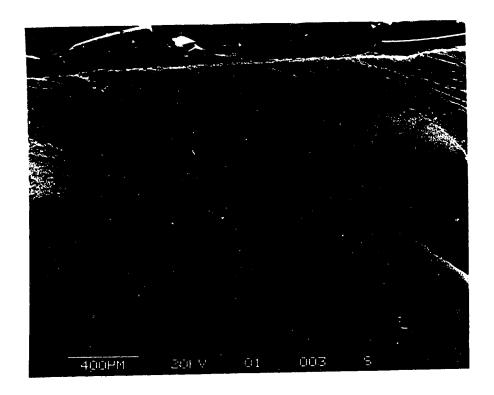
Plate 4.1   Scanning electron micrograph of the $Bi_4Sr_3Ca_3Cu_6O_{18}$ sample. A
material defect runs diagonally across the sample. This defect
dominates the thermal modulation images in Figs. 4.7-4.9.

have occurred during the processing of the material. The bulk resistance of this sample is clearly representative of the material close to the defect. Attempts to measure the modulation amplitude spectrum in an area away from this defect were unsuccessful. This failure was presumably a result of the small resistivity of the material in those regions, and the dominance of the signal by the defect.

To measure the thermal diffusion length and the diffusivity of the material, one-dimensional scans of the modulation amplitude were recorded as a function of chopping frequency as the laser traversed the defect in the x-direction. The variance of each peak was measured (1/e intensity). The observed variance of the peak, σ^2_{obs}, can be represented as the sum of the variances of other experimental parameters,

$$\sigma^2_{obs} = \sigma^2_{\eta} + \sigma^2_{nat} + \sigma^2_{\omega} + \sigma^2_{tc} \qquad (4.7)$$

where the variances in the sum are due to the: thermal healing length, σ^2_{η}, natural defect size, σ^2_{nat}, spot size of the laser, σ^2_{ω}, and time constant of the lock-in amplifier, σ^2_{tc}. The last two of these contributions are negligible and can be easily calculated. Only the healing length variance is dependent on frequency. Using Eq. 4.6, the following equation develops,

$$\sigma^2_{obs} = \frac{D}{\pi f} + \left[\sigma^2_{nat} + \sigma^2_{\omega} + \sigma^2_{tc}\right] \qquad (4.8)$$

A plot of σ^2_{obs} vs. 1/f should have a slope equal to D/π. The intercept should be equal to the term in brackets from which the defect size can be estimated. Such a plot, Figure 4.10a, showed slight negative curvature at high values of 1/f (low frequency), due to a dependence of the signal on the thermal coupling of the sample to the cold finger at low modulation frequencies. In the limit of zero modulation frequency, the variance
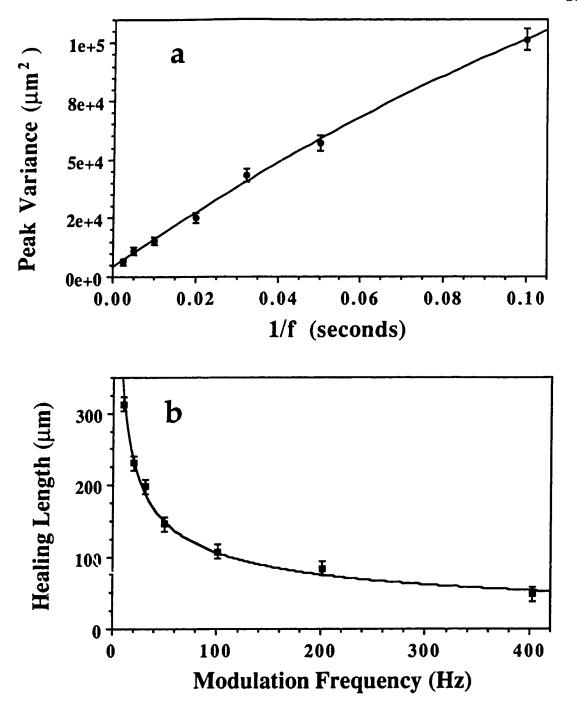
Figure 4.10 (a) Estimation of the thermal diffusivity of the material. (b) Frequency dependence of the dynamic thermal healing length. See text for details of the measurement process.

converges to a steady value which can be characterized by the static thermal healing length, η_0 [2]. The data was thus fit to a second order polynomial. The linear term of the fit gives the slope in the high frequency regime, where Eq. 4.6 is expected to hold true. In this way, the thermal diffusivity of the material was estimated to be 3.9 ± 0.2-mm^{2}sec^{-1} at 72-K. It is difficult to compare this estimate with literature because of the inhomogeneity and uniqueness of the material. Fanton et al. have reported a thermal diffusivity of 1.9-mm^{2}sec^{-1} at room temperature for a single crystal $Bi_2Sr_2CaCu_2O_x$ sample using a photothermal measurement [4]. From the intercept, the defect size was estimated to be 140 ± 20-μm. This is slightly larger than the observed 50-μm width.

The thermal healing length was extracted from the previous data and plotted as a function of chopping frequency in Figure 4.10b. The healing length varies from over 300-μm at 10-Hz to 50-μm at 400-Hz, the highest frequency used in this study. The exponential fit shown by the solid curve yielded an exponential coefficient of 0.49, close to the expected value of 0.5.

Higher modulation frequencies were not used with this sample due to poor noise characteristics. The amplitude signal falls off quickly with modulation frequency. This is illustrated in Figure 4.11, where the thermal modulation amplitude was measured as a function of frequency with the 15-mW laser impinging on the defect. A 7-mA(rms) current was used. The modulation amplitude was also measured for the continuous laser beam with no modulation. This 0-Hz amplitude was measured by monitoring the resistance of the sample as the laser was turned on while being focused to the same spot as in the modulated measurements. This value represents the steady state amplitude of an infinitely slow modulated beam. The actual
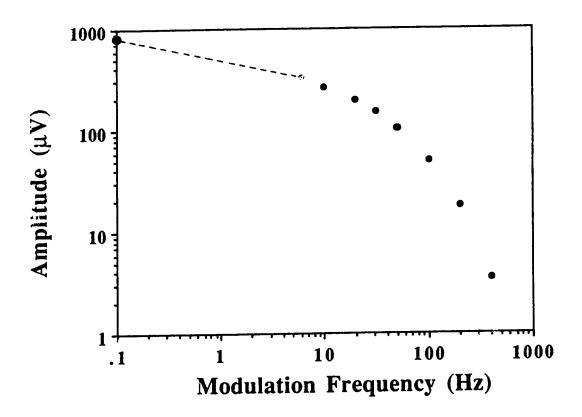
Figure 4.11 Frequency dependence of the thermal modulation amplitude. The steady state (0-Hz) laser modulation amplitude has been assigned a frequency of 0.1-Hz to accomodate the log-log plot. The decreased signal-to-noise at high frequencies ultimately limits the spatial resolution possible in thermal modulation imaging.

amplitude was divided by two to account for the rms value of a square wave that the lock-in amplifier would actually measure. On the log scale of the plot, this point has been given a frequency value of 0.1 Hz, conservatively estimating a 10-second delay for steady state to be reached.

4.5 CONCLUSIONS

The laser based photothermal modulation technique presented in this chapter provides a new method for characterizing high temperature superconducting materials. It can be used for making differential resistivity measurements on the bulk material to identify resistive transitions. It also can be used for making spatial measurements of the differential resistivity of inhomogeneous materials, helping to elucidate the source of the inhomogeneities.

In this study, spatial resolution of 10-μm has been demonstrated for imaging optical features on the sample. Thermal resolution on the order of 50-μm has been achieved using a 400-Hz modulation frequency. It should be possible to attain higher spatial resolution by going to still higher optical modulation frequencies, providing that the S/N ratio is adequate. In this respect, this technique could well be applied to the study of thin film superconductors. The increased current density present in a submicrometer thickness film (smaller volume sample-see Eq. 4.5) should lead to increased sensitivity. The increased signal will allow higher modulation frequencies and higher spatial resolution to be obtained.

Thin film critical current imaging has previously been performed using high frequency modulated electron beams [3]. It is believed that the laser source used in the present study results in a dramatic simplification of

the apparatus, eliminating the need for sophisticated electron beam apparatus, electronics and high vacuum hardware.

REFERENCES

(1) Superconductivity was first discovered by Heike Kamerlingh Onnes in Leiden (1853-1926) in 1911 while making resistance measurements on Hg metal at liquid helium temperatures.

(2) R.P. Huebener in *Advances in Electronics and Electron Physics* **70**, P.W.Hawkes, Ed., 1 (Academic, New York, 1988).

(3) J.Mannhart, R. Gross, K. Hipler, R.P. Huebener, C.C. Tsuei, D. Dimos and P. Chaudhari, *Science* **245**, 839 (1989).

(4) J.T. Fanton, D.B. Mitzi, A. Kapitulnik, B.T. Khuri-Yakub, G.S. Kino, D. Gazit and R.S. Feigelson, *Appl. Phys. Lett.* **55**, 598 (1989).

(5) R. McLaren and N.J. Dovichi, *Anal. Chem.* **60**, 730 (1988).

(6) R. McLaren and N.J. Dovichi, *Can. J. Chem.* **67**, 1178 (1989).

(7) Keithley - *Low Level Measurements* , 3rd ed., Keithley Instruments Inc. Cleveland, Ohio (1984).

(8) J.W. Ekin, A.J. Panson and B.A. Blankenship, *Appl. Phys. Lett.* **52**, 331 (1988).

(9) T.W. Jing, Z.Z. Wang and N.P. Ong, *Appl. Phys. Lett.* **55**, 1912 (1989).

(10) J.R. Clem and R.P. Huebener, *J. Appl. Phys.* **51**, 2764 (1980).

(11) P. Horowitz and W. Hill, *The Art of Electronics* , Cambridge University Press, New York (1980).

(12) J.M. Tarascon, Y. Le Page, P. Barboux, B.G. Bagley, L.H. Greene, W.R. McKinnon, G.W. Hull, M. Giroud and D.M. Hwang, *Phys. Rev. B* **37** , 9382 (1988).

(13) H.K. Liu, S.X. Dou, N. Savvides, J.P. Zhou, N.X. Tan, A.J. Bourdillon, M. Kviz and C.C. Sorrell, *Physica C* **157**, 93 (1989).

(14) B. Zhu, L. Lei, S.L. Yuan, S.B. Tang, W. Wang, G.G. Zheng, W.Y. Guan and J.Q. Zheng, *Physica C* **157**, 370 (1989).

(15) H. Liu, X. Zhan, Y. Chao, G. Zhou, Y. Ruan, Z. Chen and Y. Zhang, *Physica C* **156**, 804 (1988).

(16) B. Kabius, M.E. Gomez, P. Prieto, S. Thierfeldt and R.R. Arons, *Physica C* **162-164**, 635 (1989).

(17) M. Pissas, D. Niarchos, C. Christides and M. Anagnostou, *Supercond. Sci. Technol.* **3**, 128 (1990).

(18) Y. Enomoto and T. Murakami, *J. Appl. Phys.* **59**, 3807 (1986).

(19) A. Frenkel, M.A. Saifi, T. Venkatesan, C. Lin, X.D. Wu and A. Inam, *Appl. Phys. Lett.* **54**, 1594 (1989).

(20) W.S. Brocklesby, D. Monroe, A.F.J. Levi, M. Kong, S.H. Liou, J. Kwo, C.E. Rice, P.M. Mankiewich and R.E. Howard, *Appl. Phys. Lett.* **54**, 1175 (1989).

(21) H. Maeda, Y. Tanaka, M. Fukutomi and T. Asano, *Jpn. J. Appl. Phys.* **27**, L209 (1988).

(22) C.N.R. Rao, L. Ganapathi, R. Vijayaraghavan, G. Ranga Rao, K. Murphy and R.A. Mohan Ram, *Physica C* **156**, 827 (1988).

(23) M.A. Subramanian, C.C. Torardi, J.C. Calabrese, J. Gopalakrishnan, K.J. Morrissey, T.R. Askew, R.B. Flippen, U. Chowdhry and A.W. Sleight, *Science* **239**, 1015 (1988).

(24) D.S. Burgi, Ph.D. Dissertation, University of Wyoming (1987).

APPENDIX B

This appendix presents the circuit, Figure 4.20, used for generation of a reference signal at either the upper, F+f, or lower, F-f, sideband frequency. Input to the circuit are the reference signals from the function generator (F) and chopper (f). The two signals are first ac-coupled using high-pass RC type filters. The generator signal is input to a comparator to produce a constant amplitude signal, independent of the current through the sample. The two frequencies are input to a four quad mixer where they are multiplied. The ac-coupling removes any dc offsets to ensure that the output of the multiplier is a "double-sideband-supressed-carrier" signal. The absence of the carrier produces a purer frequency signal after filtering.

A bandpass filter is used to pass one sideband frequency while rejecting the other. The first bandpass filter built was a homemade model in which three MF10 monolithic-dual-switched-capactior-filter chips were used. Six (two per chip) variable frequency high pass filters were cascaded in series. The variable frequency capacity was achieved by inputing a 100x clock frequency. This filter performed adequately, although the impurity of the reference signal produced a background and noise in the thermally modulated signal. Careful tuning brought this background to a minimum. A second design used a very sharp TTE active bandpass filter. The -36dB stopband width was 4.3% of the center frequency. This filter was not tunable; instead, the frequencies F and f were chosen to produce an appropriate sideband at the filter frequency (2 or 5-kHz). Tuning was then accomplished by making fine adjustments of the chopper frequency.
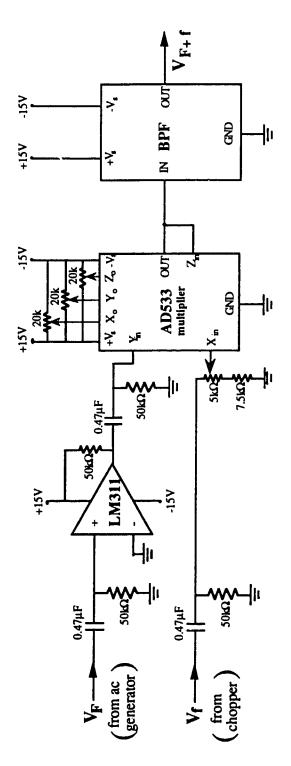
Figure 4.A Circuit used for generation of a reference signal at the sideband frequency, F+f or F-f.

CHAPTER 5

Pb AND Sb SUBSTITUTION IN

Bi-Sr-Ca-Cu-O HIGH TEMPERATURE

SUPERCONDUCTORS

5.1 INTRODUCTION

In the Bi-based class of high temperature superconductors, three phases are known to exist with the general formula, $Bi_2Sr_2Ca_{n-1}Cu_nO_{(2n+4)+y}$. The three phases with n=1, 2, and 3, known as the 2201, 2212, and 2223 phases for the Bi:Sr:Ca:Cu atom ratios, have transition temperatures of ~10-K [1], ~85-K [2] and ~110-K [3] respectively. Maeda [2] first discovered superconductivity above 100-K in this system in 1988 although he was unable to reach zero resistance above 85-K. Synthesis and isolation of predominantly 110-K phase samples with Tc > 100-K proved to be difficult. Attempts to obtain monophase 2223 samples inevitably resulted in a mixture of 2212 and 2223 phases.

The doping of a small amount of Pb to substitute for Bi in the mixtures, $Bi_{2-x}Pb_xSr_2Ca_2Cu_3O_{10+y}$, was found to enrich the 2223 phase in the sample [4-6]. This stabilization of the 2223 phase enabled routine preparation of samples with zero resistance at tempertatures greater than 100-K. But still, it was difficult to obtain zero resistance at 110-K in polycrystalline samples because of a resistive tail or 'foot' below the main transition temperature [6,7]. Substitution of Sb for Bi was also found to stabilize the 2223 phase [8-10]. In addition, several cases of superconductivity at 132-K in the Bi-Sb-Pb-Sr-Ca-Cu-O system were reported [11 13]. In a different report, a sample with Sb and Pb substitution showed signs of superconductivity at 140-K [14]. The sample contained the 2212 and 2223 phases and a new phase that was identified as a Pb,Sb substituted 4441 material by X-ray and electron diffraction. Many of these new transitions were unstable, disappearing after

one or a few thermal cyclings of the sample between 100-K and room temperature.

In this study, the possibility of transition temperatures greater than 130-K was investigated by solid state synthesis of Sb substituted 2223 phase polycrystalline samples. Photothermal conductivity modulation (PCM) and resistance measurements were used to search for such transitions. In addition, the source of the resistive 'tails' in the Bi-Pb-Sr-Ca-Cu-O system was investigated by resistance and PCM measurements, PCM imaging and scanning electron microscopy (SEM) of synthesized polycrystalline materials. Results are also presented that show evidence of heat capacity jumps at the main transition temperature in polycrystalline samples. Previously, heat capacity jumps have only been seen in predominantly single phase materials [15].

This study further characterizes PCM as a tool for the study of high-T_c superconductors. The details of this new photothermal method were outlined in Chapter 4. The measured signal is given by

$$\Delta V_{rms} = \frac{IR}{8v\rho} \frac{d\rho}{dT} \frac{P(1\text{-}r\ )}{fC_p}$$

(5.1)

where I is the current through the sample with bulk resistance R, v is the volume of sample between the inner leads, ρ is the resistivity of the sample within one thermal diffusion length (see Eq. 4.6) of the laser beam spot, P is the incident power, r is the reflectance from the surface and C_p is the heat capacity of the sample. This equation is valid for optically and thermally thick samples and high optical modulation frequencies, f.

5.2 EXPERIMENTAL

5.2.1 Superconductor Synthesis and Preparation

Samples were synthesized with the following general formulas, $Bi_{2-x}Pb_xSr_2Ca_2Cu_3O_{10}$ and $Bi_{2-y}Sb_ySr_2Ca_2Cu_3O_{10}$. The values of x were: 0, 0.1, 0.2, 0.3, 0.4, and 0.5 representing a range of 0 to 25% lead substitution for bismuth. The values of y were: 0, 0.04, 0.08, 0.12, 0.16, and 0.20 representing a range of 0 to 10% antimony substitution for bismuth. The raw materials were Bi_2O_3 (JMC puratronic, Hertfordshire, England), $SrCO_3$ (JMC), $CaCO_3$ (JMC), CuO (JMC), PbO (Fisher reagent, Fair Lawn, NJ.) and Sb_2O_3 (BDH reagent, Poole, England). The materials were weighed to give the appropriate metal atom ratios in ~10-g batches.

Table 5.1	Melting points of 2223 mixtures.
Mixture	**MP (°C)**
$Bi_2Sr_2Ca_2Cu_3O_{10}$	882 - 884
$Bi_{1.6}Pb_{0.4}Sr_2Ca_2Cu_3O_{10}$	877 - 879
$Bi_{1.8}Sb_{0.2}Sr_2Ca_2Cu_3O_{10}$	880 - 882

The mixtures were ground with mortar and pestle, homogenized on a tumbling mixer for a few hours, and calcined in air inside a muffle furnace for 24 to 72 hours at 840 - 850°C. A thermocouple was placed in the oven in contact with the crucible to monitor the temperature. The analog output from the thermocouple and a stripchart recorder were used to record the thermal history of the sample. After cooling, the mixture was again ground, homogenized, and pressed into pellets of 1-cm diameter and ~1-mm thickness. The pellets were annealed for 48 to 96 hours at 2 to 5 degrees below their melting points. The melting points of 3 mixtures,

Table 5.1, were measured in the muffle furnace before annealing. A slight melting point depression exists with Pb and Sb substituted mixtures compared to the mixture without substitution. After annealing, the samples were oven cooled to room temperature over a period of ~12 hours.

The ceramic pellets were cut into pieces of 7×2×1-mm dimensions. Electrical connections to the samples were made in a manner similar to that described in Chapter 4. Briefly, this involved sputtering gold contacts onto t͟ ͟ ͟ ͟ ͟ ͟ ͟ ͟ ͟ ͟ ͟ ͟ ͟ fixing thin wires to the contact with silver epoxy, and curing at 80 to ͟ ͟ ͟ ͟ ͟ ͟ 2 to 4 hours.

5.2.2 Measurements

A detailed description of the methods for making resistance and thermally modulated resistance measurements was given in Chapter 4. The resistance was recorded with a four-probe ac method. PCM signal amplitude measurements were made with either a 10-mW He-Cd laser or a 6-mW argon ion laser beam. PCM phase signals were recorded simultaneously with the amplitude signal and can, in principle, provide additional information about the thermal processes in the sample. In general, these signals were noisier and more difficult to interpret than the amplitude signal. The beam spot size for high resolution imaging was measured to be 15(2)-μm. All PCM measurements were made with ac currents of 5 to 10-mA rms unless otherwise specified.

A new image collection program (see Appendix C) was written for this study. IEEE interface is used for communication and data collection from the temperature controller, actuator controller and lock-in amplifiers. Data is collected with a comb scanning method [16]. With this method, data is

collected sequentially along an X-line. At the end of each line the 'y' actuator is incremented while the 'x' actuator is returned to the x=0 position. The data along an x-line is collected on the move, which simplifies the collection algorithm. The time constant of the lock-in was set to 300-msec or 1-sec for data collection rates of 1-Hz, 1/2-Hz or 1/3-Hz depending on the noise in the signal. Images were smoothed with an equal weighting 9-point matrix (3 points in x or y direction) method.

Scanning electron micrographs were collected on a Cambridge S250 system with 20-kV electron beam. The system had the capability of performing Energy Dispersive X-ray Analysis (EDXA) for heavy elements.

5.3 RESULTS AND DISCUSSION

5.3.1 Substitution Effects

Resistance and PCM signals were recorded for each sample. Currents of 1-mA were used to record the resistance. PCM measurements were made with a 1-mm spot size, 10-Hz modulated beam focused between the inner electrodes. Figure 5.1 and 5.2 show the temperature dependence of the resistance of samples with Pb and Sb substitution respectively. The absolute resistance of each sample depends on the details of the electrical contacts. To suppress this variation, the resistance was normalized at 300-K, allowing a better visual comparison of the effects of substitution. The absolute resistance of these samples was 20 to 100-mΩ at 300-K. Each resistance curve is labelled with the atomic percent substitution of Pb or Sb for Bi in the 2223 nominal formula.
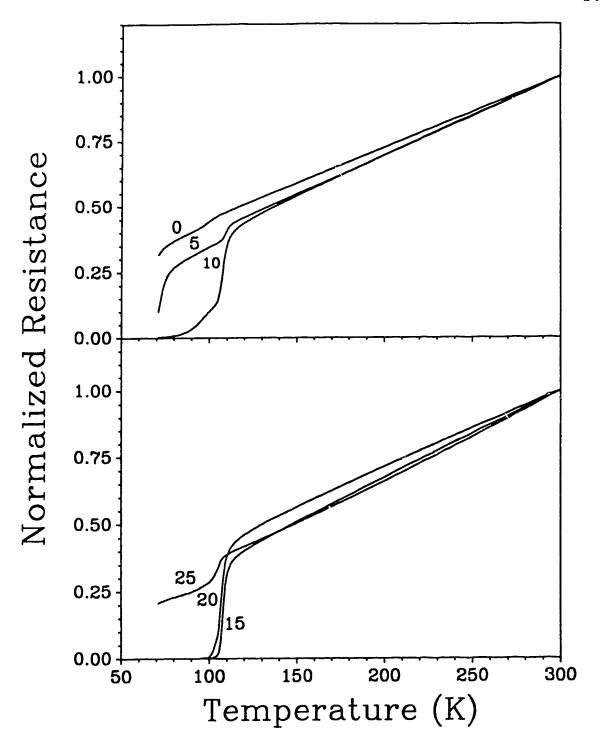
Figure 5.1 Temperature dependence of the resistance of bulk samples of $Bi_{2-x}Pb_xSr_2Ca_2Cu_3O_{10}$, for variable substitution of Pb for Bi (labelled as percent substitution).
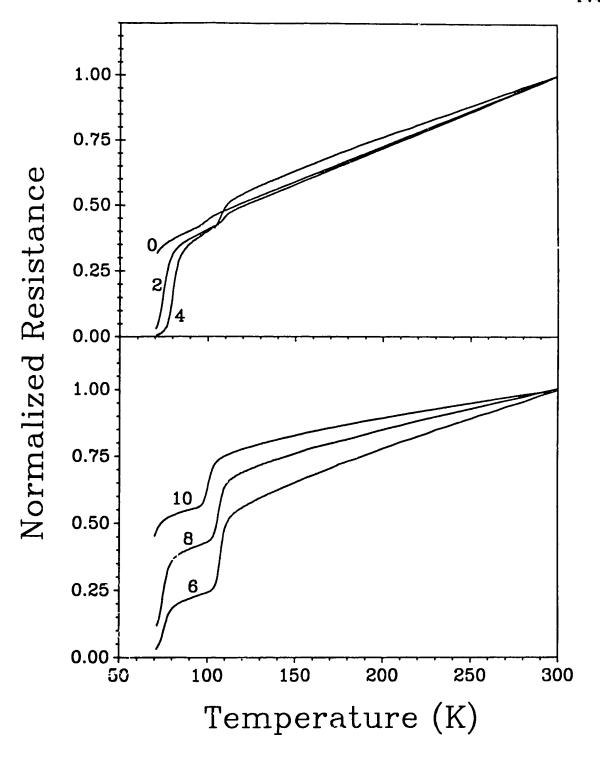
Figure 5.2 Temperature dependence of the resistance of bulk samples of $Bi_{2-x}Sb_xS_{x/2}Ca_2Cu_3O_{10}$, for variable substitution of Sb for Bi (labelled as percent substitution).
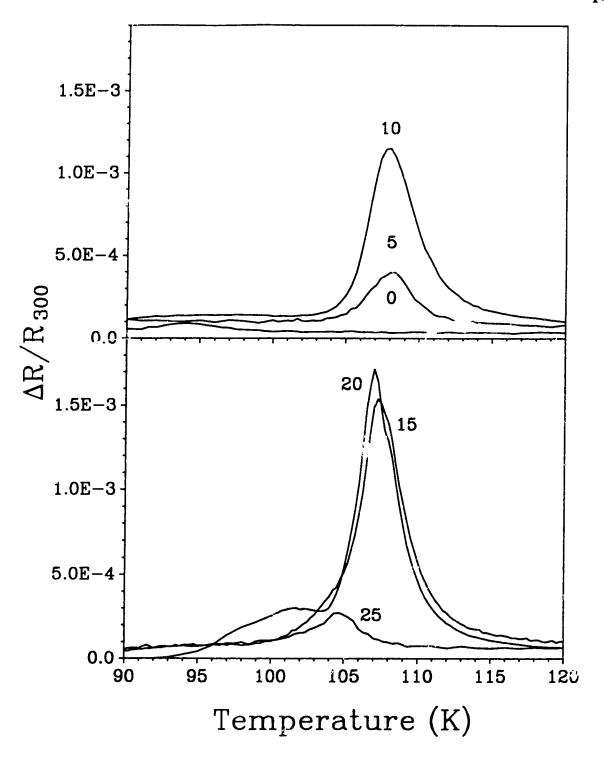
Figure 5.3 Temperature dependence of the PCM signal of bulk samples of $Bi_{2-x}Pb_xSr_2Ca_2Cu_3O_{10}$, for variable substitution of Pb for Bi (labelled as percent substitution). A 10-mW beam and 5 to 10-mA currents were used.
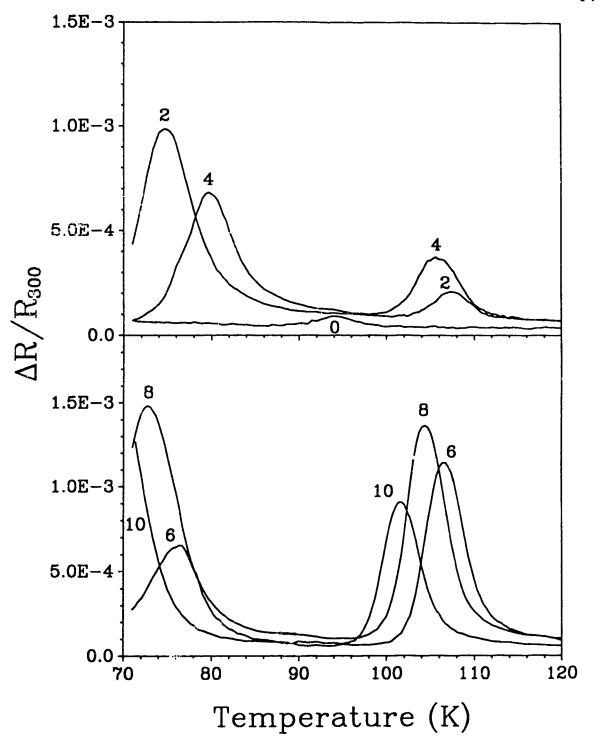
Figure 5.4 Temperature dependence of the PCM signal of bulk samples of $Bi_{2-x}Sb_xSr_2Ca_2Cu_3O_{10}$, for variable substitution of Sb for Bi (labelled as percent substitution). A 10-mW beam and 5 to 10-mA currents were used.

The temperature dependence of the PCM signal is presented in Figures 5.3 and 5.4 for samples with Pb and Sb substitution respectively. The modulated resistance signal amplitude is given by, $\Delta R_{(rms)} = \Delta V_{(rms)}/I$, where $\Delta V_{(rms)}$ is the measured voltage. This signal is normalized to the resistance at 300-K for th·· ne reasons mentioned above. The signal, $\Delta R/R_{300}$ represents the fractional modulation of the bulk resistance, referenced to 300-K.

The temperature dependence of the resistance and PCM signal for Pb substituted samples show metallic like behavior above the tr. nsition temperature for all levels of substitution. The Pb free sample shows a minor resistance transition centered at 94-K. The low temperature end of the transition ends at ~ 90 to 91K. This would suggest the prescence of some 2212 phase material. With 5% Pb substitution, a transition at 108-K becomes apparent. This transition becomes more pronounced with increased Pb substitution. The samples with 10, 15 and 20% substitution all show zero resistance above 70-K. With further increase in substitution to 25%, only a small transition is seen at 105-K and the material does not reach zero resistance above 70K. The highest temperature of zero resistance, 101-K, was obtained with 15% Pb substitution. Note that the PCM signal falls to zero when the resistance of the sample is zero. The large currents used for recording the PCM signals in Figure 5.3 prevent the signal from falling to zero above 100-K for the 15 and 20% samples. The current dependence of the resistance of these samples will be discussed later.

The optimum value of substitution is between 15 and 20%, which is in agreement with other studies [4-6, 17-19]. It is well known that Pb substitution for Bi increases the volume fraction of the 2223 phase in these materials. The

role that Pb plays in this respect is not completely understood. It is known that Pb does replace Bi in the unit cell of the 2223 phase [4].

The samples with Sb substitution (Figs. 5.2 & 5.4) show two transitions. The first transitions are seen between 100 to 110-K, a familiar range for the 2223 phase material. The second transitions are very broad with onsets between 85 to 90-K and midpoints in the 70 to 80-K range. These are characteristic of the 2212 phase. Only the 4% substituted sample reached zero resistance above 70-K. This substitution appears to be the optimum for this system. The resistance was monitored during the initial cooling and recorded on the first cycle of heating for each sample in this study to look for transitions that were reported in the 130 to 140K range. There was no evidence of any resistive transitions at T>110-K. The PCM signal was also monitored in the 130 to 170-K range. There was no evidence of signal above the noise in the baseline. After initial reports of superconductivity above 110-K with Sb substituition, other researchers also have failed to find either resistive or magnetic transitions in this system [8-10,20]. Reference 20 contains members of the group that originally reported superconductivity at 132-140K. They claim that their different preparation and sintering conditions are responsible for the absence of the new 130K-T_c phase in this new report. They did find an additional nonsuperconducting phase attributed to the Sb substitution. If transitions occur above 110-K in the Bi-Pb-Sb-Sr-Ca-Cu-O system, they are very sensitive to the processing conditions of the sample.

Table 5.2	Effect of Pb and Sb substitution on the transition temperature of the 2223 phase.		
% Pb	$T_{c,mid}$ (K) *	% Sb	$T_{c,mid}$ (K) *
5	108.2	2	107.5
10	107.8	4	105.8
15	107.3	6	106.5
20	106.9	8	104.3
25	104.6	10	101.5

* $T_{c,mid}$ is the temperature (K) at the midpoint of the transition identified by PCM signal measurements. The uncertainty is 0.2-K.

The temperature at the midpoint of the 2223 transition appears to decrease with increasing Pb and Sb substitution. This appears more clearly from the PCM spectra, which approximate dR/dT over the small temperature range of the transition. The midpoint transition temperatures are listed in Table 5.2. The lowering of the transition temperature may be due to a contraction of the c-axis in the crystal structure of the 2223 phase that has been reported for Pb and Sb substitution [10]. Alternatively, increased oxygen in the system may be responsible for this effect.

5.3.2 Current Dependence of the PCM Signal

The current dependence of the PCM signal was recorded for two of the samples with 15 and 20% Pb substitution. A signal representative of a large fraction of the sample between the electrodes was obtained by using a 1-mm spot size beam and a low 10-Hz optical modulation. The signal was recorded using a 100-Hz ac current and two-lock-in detection. The signal, $\Delta R = \Delta V / I$, is

presented in Figure 5.5 as a function of temperature for different applied currents.

The transition in the 20% Pb sample, Fig. 5.5a, appears to have two components. The first component is the main transition at 107-K, which is insensitive to current (in this range). The second component, the shoulder on the low temperature side of the main transition, is very sensitive to current. The result was the same for the 15% Pb sample, Fig. 5.5b, although the magnitude of the resistive 'tail' was much smaller. The sensitivity of the lock-in was increased to record the low temperature component of the tail in detail. The temperature at which the shoulder falls to zero signifies the temperature of zero resistance in these samples. Resistance measurements showed the same result as that seen in Figure 5.5a although the separation of the superconducting transition into two components, one current sensitive and the other current insensitive, is not as clear.

The possibility of heating at the contacts causing the current dependence of the resistive shoulder can be dismissed for two reasons. First, the observed shift does not correlate with I^2R heating and is much larger than would be expected for a 10-Ω contact. The cooling capacity of the refrigerator, 300-mW, greatly exceeds the 1-mW heat input that would result from the highest current. Second, the main transition component at 107-K does not shift temperature in the slightest at the highest current, which is unexpected if there were temperature gradients of 10-K in the sample.

The current dependence of the resistive tail in Fig. 5.5a suggests that extrapolation to zero current would give a transition that overlaps with the main transition at 107-K. Superconductors are known to have a critical
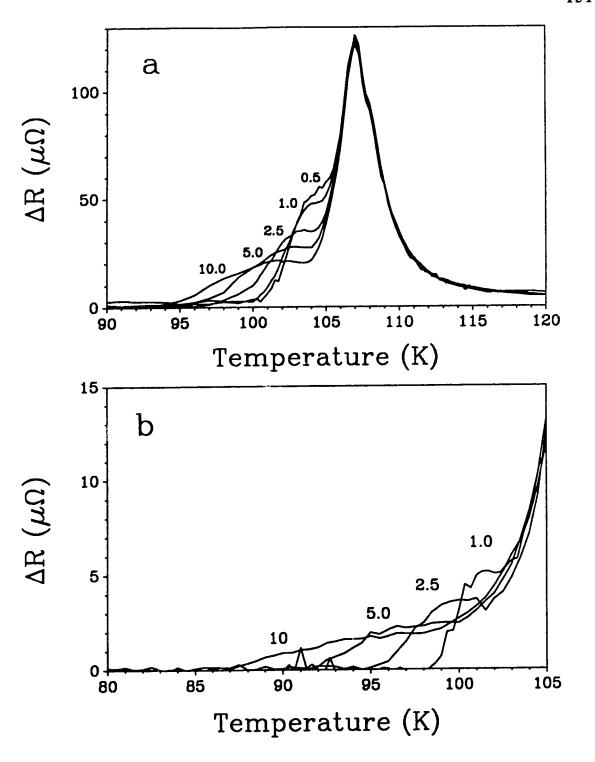
Figure 5.5   Current dependence of the PCM signal recorded for the 2223 superconducting transition for samples with (a) 20% and (b) 15% Pb substitution for Bi. The transitions are clearly separated into two components, one which is current sensitive and the other which is not.

current limit, J_c, above which the transition temperature begins to decline because of the increased magnetic fields induced by the current [26]. It is thus likely that the two components of the transition are both due to the 2223 phase. The main transition at 107K may arise from areas in the sample where J_c is not exceeded, such as in individual grains with well formed 2223 phase. The resistive tail would arise from areas in the sample where J_c is exceeded, such as those where the current is forced through small cross sectional areas. This would occur at grain boundaries. The limitation of critical current densities by grain boundaries in polycrystalline and thin film specimens has become clearer in the recent past [21-24]. Polycrystalline specimens generally show lower transport critical currents due to poor coupling between the grains. Repeated grindings and annealing will improve this coupling and increase the critical current [22].

Lead substitution increases the proportion of the 2223 phase in the material. Taracson et al made resistance measurements on single grains of a Bi-Sr-Ca-Cu-O sample [25] without Pb substitution. The 2223 transition in the sample was found to be current sensitive even at low currents of 0.6-mA. The grains were later characterized by electron diffraction and found to contain a 2212 core with a thin 2223 shell. The shell was described as cryptocrystalline. The thinness and cryptocrystalline nature of the 2223 shell would explain the low critical current in the grain. The addition of lead must improve the quality of the 2223 phase in grains, judging by the current independence of the main transition in Fig. 5.5a. A SEM micrograph of the 20% Pb substituted sample is shown in Plate 5.1. Most of the sample shows grain structure similar that shown in the micrograph. The grains are predominantly plate-like. The plate-like grains in the Bi-Sr-Ca-Cu-O system
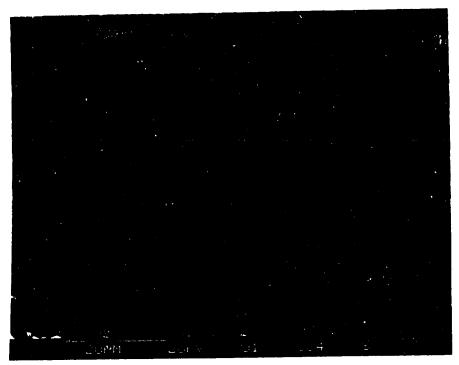
Plate 5.1   SEM micrograph of a $Bi_{1.6}Pb_{0.4}Sr_2Ca_2Cu_3O_{10+y}$ sample showing plate-like crystals, believed to contain both 2212 and 2223 superconducting phases.

Plate 5.2   SEM micrograph of a $Bi_{1.6}Pb_{0.4}Sr_2Ca_2Cu_3O_{10+y}$ sample. Areas enriched in Ca and Cu and deficient in Bi and Pb, exist in the sample.

have been found to contain both 2212 and 2223 phases in a stacked arrangement [27]. This type of stacking arrangement can also be seen in the grains of Plate 5.1.

Plate 5.2 shows the micrograph of another area on the same 20% Pb sample. A few islands with these rod-like crystals and spherical particles were found on the sample. EDXA imaging was done on a 100-μm area containing such an island, and surrounded by the plate-like crystals (Plate 5.1). Compared to the plate-like crystals, the central island contained larger amounts of Cu and Ca, very little Bi and Pb. and an equally dispersed concentration of Sr. Analysis on one of the small spherical particles showed that it contained a large amount of Ca. Based on these observations and reports in the literature, it is probable that the specimen contains Ca_2CuO_3 impurity phases. This impurity has been previously identified [19,25] and was found to appear at annealing temperatures greater than 865°C [19]. Areas containing large concentrations of this impurity would not generate a PCM signal due to the lack of superconductivity.

While Pb substitution increases the proportion of the 2223 phase, intergranular resistance still exists. The connection between these grains must be improved before these materials can be applied in bulk applications such as superconducting wires requiring large current densities. Processing techniques such as 'melt texturing' are currently finding success in this regard [28].
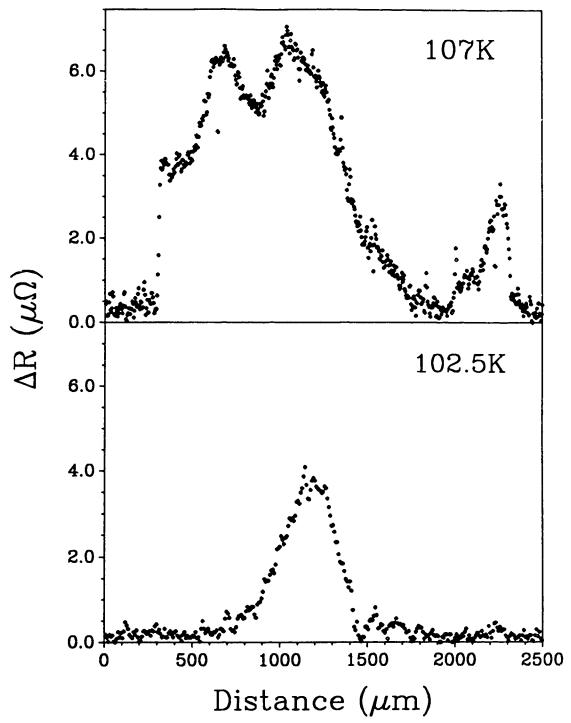
5.3.3 PCM Imaging

The appearance of two components in the 2223 transition of the Pb-substituted samples prompted the use of PCM imaging to spatially resolve

the different components. The 20% sample was chosen as a candidate sample because of its large amplitude resistive tail. One dimensional scans across the width of the sample between the inner leads were done using 50-Hz optical modulation and a 5-mA current. The PCM signal is plotted as a function of distance across the pellet at 107-K and 102.5-K in Figure 5.6. The plot can be thought of as a cross section of the sample with current travelling along the center of the sample perpendicular to the page. The edges of the sample are seen at ~300-µm and 2300-µm. A dramatic difference is seen for the signal generated at the two temperatures. At 107-K, signal is generated across the sample, apart from a hole at ~1900-µm. At 102.5-K, signal is only generated in a 500-µm wide section. The structure seen in the 107K scan was spatially resolved at f=50-Hz but not apparent at f=10-Hz. The peaks could signify areas in the sample where Pb substitution effectively gen???at?? a large proportion of the 2223 phase. Alternatively, the peaks could ind??u?e areas of high current density. Linear scans across the 15% Pb substituted sample showed similar structure with three maximums across the width of the sample.

At 102.5-K, the signal peak is directly in the middle of the sample along the direct line from one lead to the other. Current density would be expected to be highest there for closely spaced leads. The higher current density would lead to a reduction in $T_c(R=0)$ (Fig 5.5a) and an increase in the local PCM signal. Near the edges of the sample, the current density is lower and $T_c(R=0)$ is higher. These areas are either superconducting or very close to it at 102.5K. These results indicate that PCM can be used to spatially resolve regions of high current densities under some circumstances.

To generate a more uniform current density across the samples, a larger inner electrode spacing (4-mm) was used on new samples cut from the

Figure 5.6   PCM signal recorded across a sample, $Bi_{1.6}Pb_{0.4}Sr_2Ca_2Cu_3O_{10+}$,
107K and 102.5K. The lower temperature scan identifies areas of
high current density in association with poor grain coupling low \ ir\
transition temperature. High current density directly between the
electrodes generates the peak at 102.5K.

same 20% Pb pellet. An unfortunate but interesting mistake was made at this point. Whereas for all previous samples, contacts were consistently made on the top side of the pellet (the side in direct contact with air in the oven), contacts on these samples were made on the bottom side of the pellet (pellet was seated on an alumina crucible). The resistance of both samples did not reach zero above 70K, despite the fact they came from the same pellet as the sample in Fig. 5.1. The resistance and PCM signal of a sample with electrical contacts made on the bottom of the pellet are shown in Figure 5.7. Measurements made on the sample with contacts on the top side of the pellet are shown for comparison. The lack of exposure to the atmosphere is most likely responsible for the lack of superconductivity above 100-K on the bottom side of the pellet. The oxygen content of the sample has been shown to play a role in the transition temperatures of the 2212 and 2223 phases [19,29]. Decreased oxygen content is found to decrease the content of the 2223 (107K) phase and increase the content of the 2212 phase (-85K).

PCM imaging of one 'bottom side' sample was done using sideband detection at 100-Hz optical modulation, 5-mA ac current with 25-µm pixels. The estimated thermal diffusion length at this frequency is ~ 100-µm (se Chapter 4). The images, Figure 5.8, were collected at T = 108, 106, 104, 102, 10υ, and 85K. The images show a pronounced change from 108K, at a temperature just above the main transition, to 100K, where intergranular resistance of the 2223 phase is important. Dropping the temperature further to 85-K results in a significant loss in signal across much of the sample. A large peak remains in the top right corner of the image. The temperature dependence of the PCM signal was very current sensitive in this area, shifting by 10-K to lower
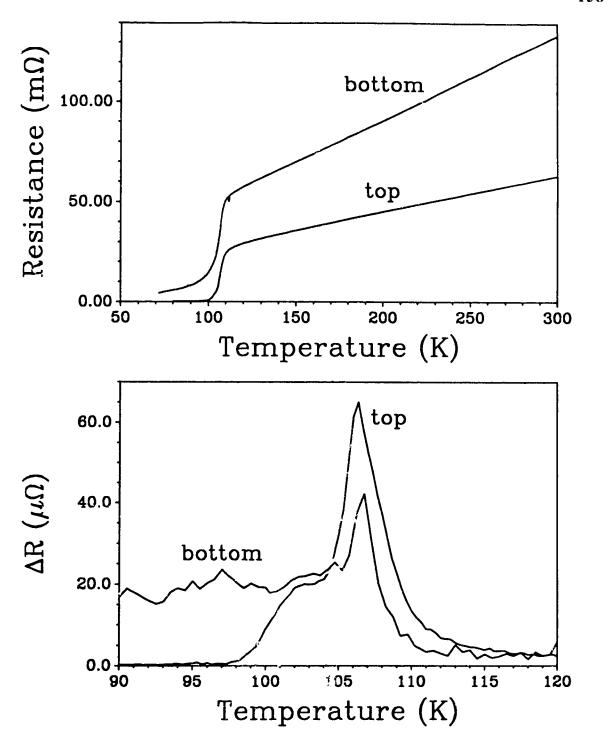
Figure 5.7 Temperature dependence of the resistance and PCM signal for the top side and bottom side of a pellet ,$Bi_{1.6}Pb_{0.4}Sr_2Ca_2Cu_3O_{10+y}$.
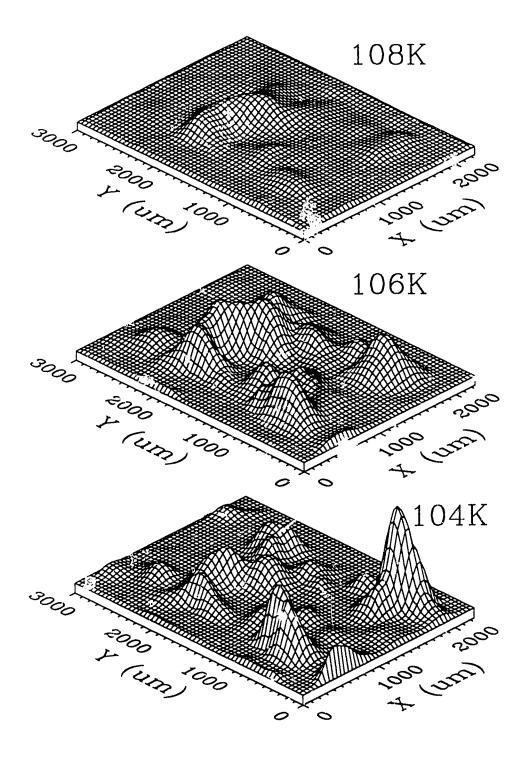
Figure 5.8 Images of the PCM signal (f=100-Hz) at different temperatures between the inner electrodes of a sample, $Bi_{1.6}Pb_{0.4}Sr_2Ca_2Cu_3O_{10+y}$. The images show regions undergoing resistivity transitions at each temperature.
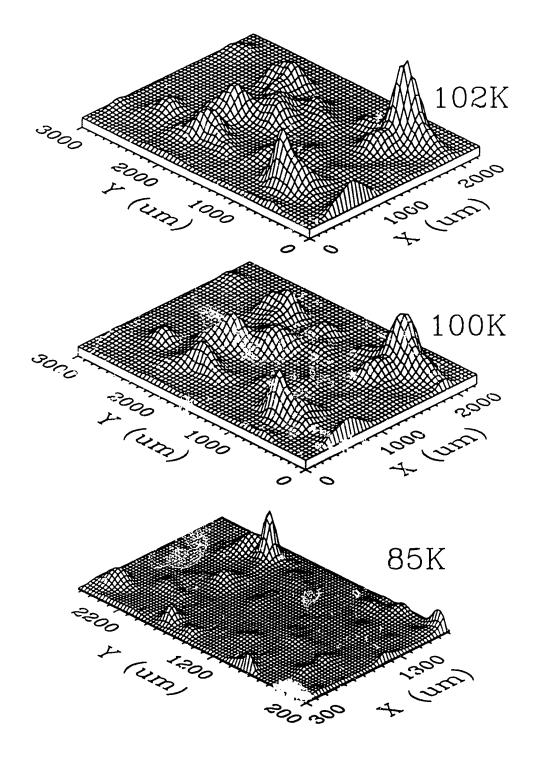
Figure 5.8 Images of the PCM signa (=100-Hz) at different temperatures between the inner electrodes of a sample,$Bi_{1.6}Pb_{0.4}Sr_2Ca_2Cu_3O_{10+y}$. The images show regions undergoing resistivity transitions a* each temperature.

temperature for an increase in current from 2.5-mA to 10-mA. The intergranular coupling must be very weak in this area.

Similar images were collected for a second bottom-side sample with f=200-Hz and I=10-mA, Figure 5.9. The estimated thermal diffusion length at this frequency is 75-μm. Again, the image changes when the temperature is reduced from 106K to 95K. From 95K to 75K, many areas stop generating signal, presumably having become superconducting. Only a few peaks remain at 75K. The temperature dependence of the PCM signal was measured in several locations on the sample as shown in Figure 5.10. All the areas show evidence of the 2223 phase because of signal at 105 to 110K. None of the areas show evidence of a transition that drops to zero above 90K, in contrast to the top of the pellet. Many areas (#1,#2,#3,#4) show a signal dropping to zero in the 80 to 85 K range, indicative of the 2212 phase transition. A few areas (#5) show significant signal still at 75-K. These areas presumably have poor grain connection. There are areas on the sample that do not generate a signal at all in this temperature range (#6). This may result if current does not probe the area due to unusually large resistance, or simply due to a lack of any superconducting phases. It is interesting to note that PCM spectra #2 and #5, which appear very different, were generated at locations separated by only 160-μm. The large peak at 70 to 80-K in spectra #5 is completely absent in spectra #2. This verifies that the thermal diffusion length must be less than 100-μm.

5.3.4 Evidence for Heat Capacity Jumps at T_c

Anomalies in the temperature dependence of the PCM signals were noticed at higher optical modulation frequencies for a number of these
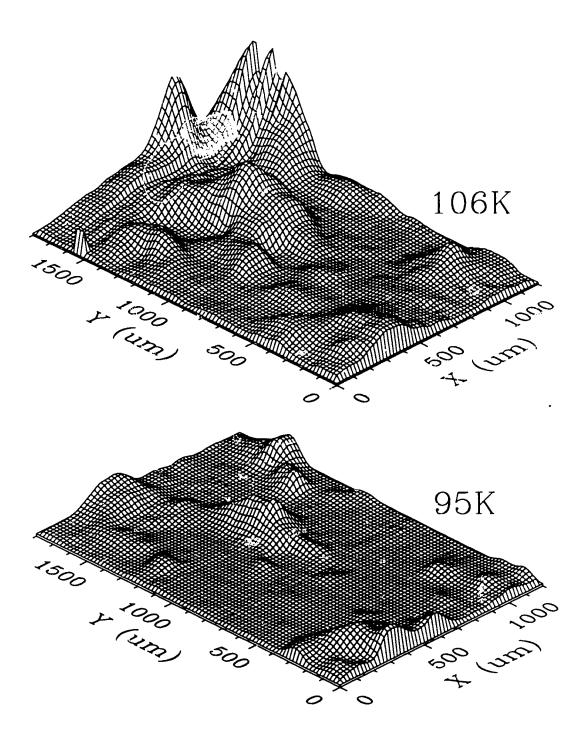
Figure 5.9 Images of the PCM signal (f=200-Hz) at different temperatures between the inner electrodes of a second sample with 20% Pb substitution.
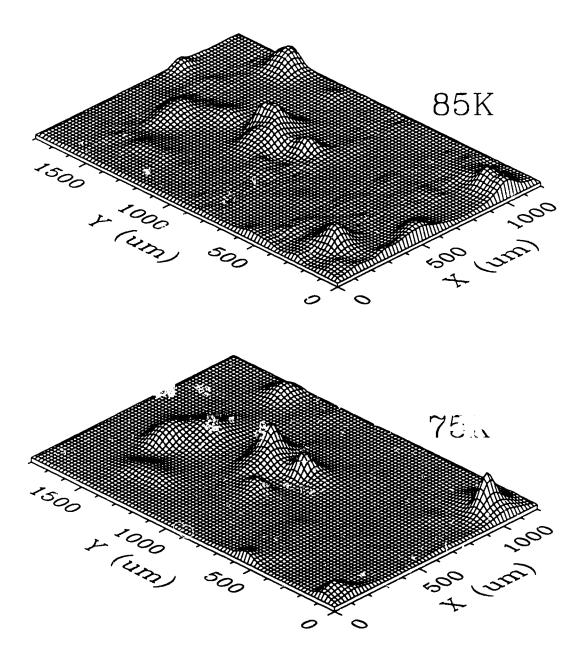
Figure 5.9 Images of the PCM signal (f=200-Hz) at different temperatures between the inner electrodes of a second sample with 20% Pb substitution.
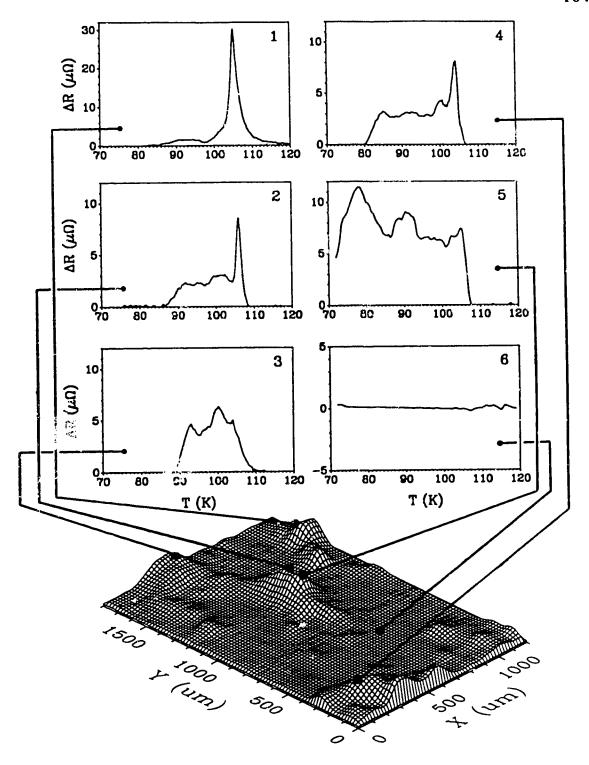
Figure 5.10 Local temperature dependences of the differential resistivity of the sample imaged in Fig. 5.9. Regions of enriched 2223 phase and 2212 phase can be identified.

samples. The anomalies went unnoticed for some time because low optical frequencies were used to record the PCM spectra for new samples such as the type in Figures 5.3 and 5.4. At higher modulation frequencies, it was anticipated that better thermal resolution would be obtained due to a decrease in the thermal diffusion length. This can be explained as follows. With a smaller thermal diffusion length, the signal is generated in a smaller region of the sample centered around the beam center. The decreased area has a smaller laser induced temperature gradient associated with it. The smaller temperature gradient at higher optical frequencies results in increased thermal resolution.

Figure 5.11 shows the PCM signal for 10-Hz and 50-Hz modulation frequencies on a 15% Pb substituted sample. This sample had a transition midpoint of 107.3K and zero resistance at 101K with low currents. A 10-mA current was used to record these spectra. An anomaly at 108-K appears on the high temperature side of the main transition peak at the higher modulation frequency. This anomoly was very reproducible, being measured at a number of frequencies and with both large and small spot sizes. To test whether this anomaly appears in the resistance of the sample, the resistance was measured as a function of T with increased averaging, and was then numerically differentiated. The differentiated spectrum, Figure 5.12, does not show such an anomaly.

The PCM signal is inversely proportional to the heat capacity of the material, Eq. 5.1. The heat capacity of superconductors are known to have a discontinuity at the transition temperature [26]. This discontinuity is large for low temperature superconductors. The elementary BCS theory predicts a jump of 143% in C_p when cooling the sample through the transition
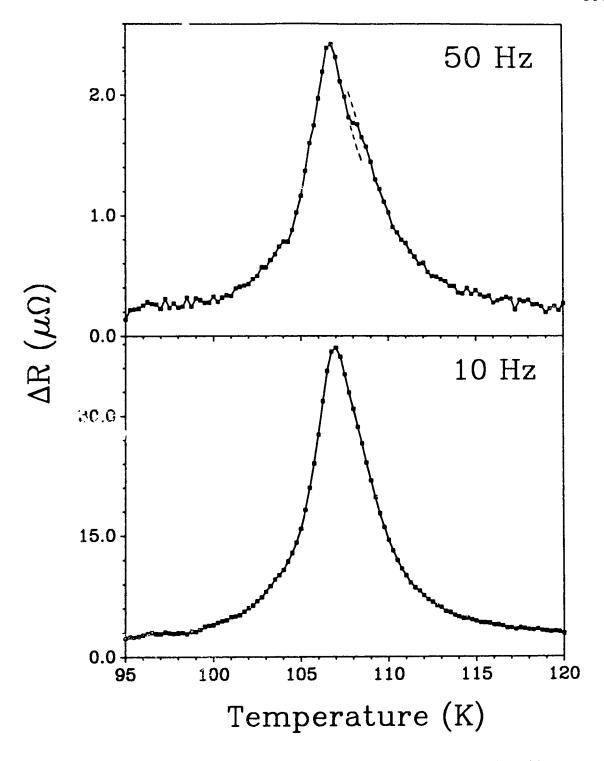
Figure 5.11 PCM signal of a 15% Pb substituted 2223 sample, recorded with I=10-mA , and f=10-Hz or 50-Hz optical modulation. At higher frequency, the increased thermal resolution reveals an anomaly in the peak, attributed to a heat capacity jump at T_c.
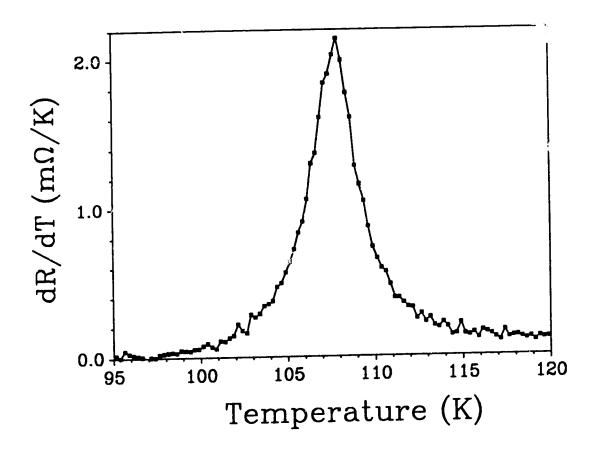
Figure 5.12 Numerically derivatized resistance of the 15% Pb substituted 2223 sample. There is no evidence of an anomoly in the resistance transition, such as that which appears in Fig. 5.11.

temperature. Transition met. elemental superconductors show jumps very close to this value [26]. Heat capacity measurements showing the anomaly at T_c in the Bi-Sr-Ca-Cu-O system have been somewhat slow in coming due to the requirement of a pure phase material to adequately see the jump. Before 1990, only a change in slope, dC_p/dT, was seen in mixed phase materials [30]. Recently, several measurements of the C_p anomaly in predominantly single phase high-T_c superconductors have been published [15,31-33]. The heat capacity jump upon cooling the sample is between 1.9% and 4% at T_c for the 123, 2212 and 2223 materials studied in those reports.

Lines drawn through the signal peak close to 108-K in Figure 5.11 show that the observed anomaly is consistent with a small jump in heat capacity, remembering the inverse relationship between PCM signal and C_p (Eq. 5.1). Quantifying the magnitude of the jump would require higher resolution spectra and a consideration of the effect of the peak shape on the measurement.

Figure 5.13 shows PCM spectra at two optical frequencies for an 8% Sb substituted sample that exhibits two resistive transitions, 2212 and 2223, clearly indicating that it is multiphase. An anomaly here appears on the lower transition at ~72-K, again on the high temperature side of the peak. A similar result was found on a 6% Sb substituted sample. There does not appear to be an anomaly on the 2223 transition peak at ~106-K.

Previous heat capacity measurements on mixed phase materials have only shown a change in slope at the transition temperature [30]. A recent report though, describes heat capacity anomalies at both 82K and 108K in a mixed phase material, 30% 2212 and 70% 2223 phase [34]. The difficulty in
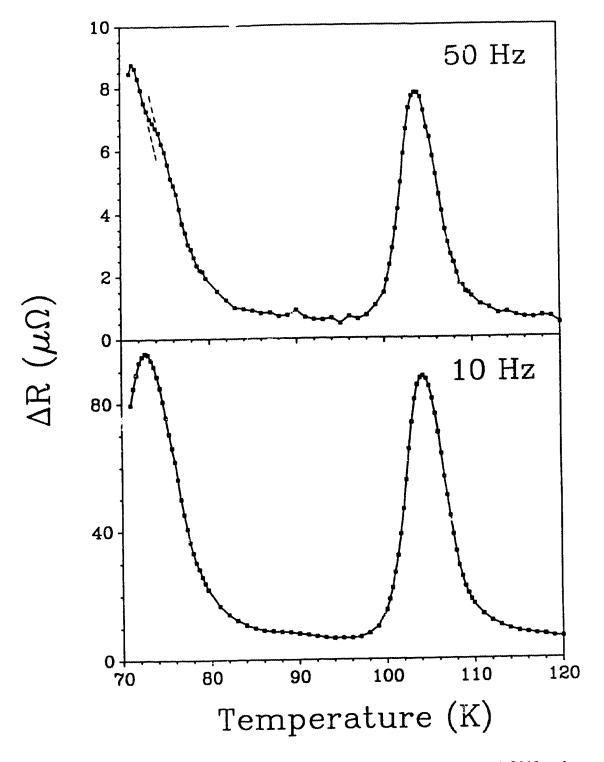
Figure 5.13 PCM signal of an 8% Sb substituted 2223 sample, with both 2212 and 2223 transitions. At the higher modulation frequency, an anomaly appears in the 2212 resistive transition, suggesting a heat capacity jump during the final transition to the bulk superconducting state.

seeing anomalies at both temperatures could be attributed to the nature of the heat capacity measurement, which is a bulk measurement. The magnitude of the jump would be reduced or smeared by the presence of other components in the sample. The PCM signal, on the other hand, does not generate signal from the full sample. Signal is only generated from material that is undergoing a resistance transition at the particular temperature of the measurement. Measurements made at 107-K are specific to the 22..., phase material only, not the 2212 phase material or other impurities in the sample. This may explain why the heat capacity jump is seen in these multiphase materials by PCM, whereas it is difficult to see with a bulk heat capacity measurement.

5.4 CONCLUSIONS

In studying the effects of Sb and Pb substitution for Bi, Pb substitution alone was found to be superior to Sb substitution for increasing the content of the 2223 phase and achieving zero resistance states above 100-K in the Bi-Sr-Ca-Cu-O superconducting system. There was no evidence of resistive transitions above 110-K for Sb substituted samples. The midpoints of the 2223 resistive transitions, identified by PCM temperature spectra, decreased with increasing substitution for both Pb and Sb substitution. PCM measurements showed that the 2223 resistive transition in these polycrystalline sample could be divided into two components. One component was the sharp high temperature component at T_c that was current insensitive up to 10-mA. The second component was a tail on the low temperature side of the main transition. It shifted to lower temperatures with increasing current, consistent with a critical current effect in the sample. The two components can be attributed to: (1) resistivity transitions in grains with well formed 2223

phase and (2) resistivity transitions associated with grain coupling in the sample.

PCM imaging of several samples was done. The utility of this method for identifying localized regions where resistive transitions are occuring, and differentiating between those regions, has been demonstrated. Grain size resolution cannot be achieved on these polycrystalline samples due to insufficient sensitivity with large sample volumes, Eq. 5.1. The spatial resolution with a 200-Hz modulation frequency was estimated to be 75-μm.

There is evidence for heat capacity discontinuities in these polycrystalline materials close to the bulk superconducting temperature. This was detected indirectly in the PCM temperature spectra at higher modulation frequencies. It is believed that this heat capacity jump is observable in multiphase materials using PCM because the signal at a specific temperature only probes material that is undergoing a transition at that temperature. This is in contrast to a bulk heat capacity measurement that probes the total sample.

REFERENCES

(1) C. Michel, M. Hervieu, M.M. Borel, A. Grandin, F. Deslandes, J. Provost, and B. Raveau, Z. Phys. B. **68**, 421 (1987).

(2) H. Maeda, Y. Yoshiaki, M. Fukutomi, and T. Asano, Jpn. J. Appl. Phys. **27**, L209 (1988).

(3) J.M. Tarascon, Y. LePage, L.H. Greene, B.G. Bagley, P. Barboux, D.M. Hwang, G.W. Hull, W.R. McKinnon, and M. Giroud, Phys. Rev. B. **38**, 2504 (1988).

(4) R. Ramesh, G. Thomas, S.M. Green, C. Jiang, Y. Mei, H.L. Luo, and C. Politis, Phys. Rev. B. **38**, 5016 (1988).

(5) H.K. Liu, S.X. Dou, N. Savvides, J.P. Zhou, N.X. Tan, A.J. Bourdillon, M. Kviz and C.C. Sorrell, Physica C **157**, 93 (1989).

(6) M. Pissas, D. Niarchos, C. Christides and M. Anagnostou, Supercond. Sci. Technol. **3**, 128 (1990).

(7) J.L. Tallon, R.G. Buckley, P.W. Gilberd and M.R. Presland, Physica C **158**, 247 (1989).

(8) C.V. Tomy, R. Prasad, N.C. Soni, K. Adhikary, A. Gulnar and S.K. Malik, Physica C **162-164**, 925 (1989).

(9) B. Kabius, M.E. Gomez, P. Prieto, S. Thierfeldt and R.R. Arons, Physica C **162-164**, 635 (1989).

(10) W.N. Wang, H.S. Koo, R.S. Liu and P.T. Wu, Physica C **162-164**, 911 (1989).

(11) H. Liu, X. Zhan, Y. Chao, G. Zhou, Y. Ruan, Z. Chen and Y. Zhang, Physica C **156**, 804 (1988).

(12) H. Liu, L. Cao, L. Zhou, Z. Mao, X. Li, Z. Yu, B. Xue, X. Mao, G. Zhou, Y. Run, Z. Chen and Y. Zhang, Sol. State. Comm. **69**, 867 (1989).

(13) M.R. Chandrachood, I.S. Mulla and A.P.B. Sinha, Appl. Phys. Lett. **55**, 1472 (1989).

(14) T. Cheng, J. Lu, C. Fan, L. Yang, Y. Lei, G. Zhou, Z. Mao, H. Wang, Z. Chen and Y. Zhang, Supercond. Sci. Technol. **3**, 87 (1990).

(15) R. Jin, F. Shi, Q. Ran, N. Shi, Z. Shi and S Zhou, Physica C **158**, 255 (1988).

(16) D.S. Burgi, Ph.D. Dissertation, University of Wyoming (1987).

(17) O. Eibl, Physica C **168**, 215 (1990).

(18) B. Zhu, L. Lei, S.L. Yuan, S.B. Tang, W. Wang, G.G. Zheng, W.Y. Guan and J.Q. Zheng, *Physica C* **157**, 370 (1989).

(19) J.L. Tallon, R.G. Buckley, P.W. Gilberd and M.R. Presland, *Physica C* **158**, 247 (1989).

(20) Q. Xu, T. Cheng, X.G. Li, L. Yang, C. Fan, H. Wang, Z. Mao, D. Peng, Z. Chen and Y. Zhang, *Physica C* **168**, 489 (1990).

(21) P. Chaudhari, J. Mannhart, D. Dimos, C.C. Tsuei, J. Chi, M.M. Oprysko and M. Scheuermann, *Phys. Rev. Lett.* **60**, 1653 (1653).

(22) D.X. Chen, Y. Mei and H.L. Luo, *Physica C* **167**, 317 (1990).

(23) E.G. Zwartz, B.A. Judd, E. Batalla, L.S. Wright, W.D. MacDonald, A.J. Otto and H. Sang, *J. Low. Temp. Phys.* **74**, 277 (1989).

(24) N. Murayama, Y. Kodama, S. Sakaguchi, F. Wakai and Y. Torii, *Physica C* **174**, 335 (1991).

(25) J.M. Tarascon, Y. LePage, L.H. Greene, B.G. Bagley, P. Barboux, D.M. Hwang, G.W. Hull, W.R. McKinnon and M. Giroud, *Phys. Rev. B* **38**, 2504 (1988).

(27) W. Herkert, H.W. Neumueller and M. Wilhelm, *Sol. State. Comm.* **69**, 183 (1989).

(26) N.W. Ashcroft and N.D. Mermin, *"Solid State Physics"*, Saunders College, Philadelphia, (1976).

(28) D.P. Hamilton, *Science*, **250**, 374 (1990).

(29) J. Zhao, M. Wu, W. Abdul-Razzaq and M.S. Seehra, *Physica C* **165**, 135 (1990).

(30) S.L. Yuan, J.W. Li, W. Wang, Q.Z. Ran, G.G. Zeng, W.Y. Guan and J.Q. Zheng, *Mod. Phys. Lett. B* **2**, 885 (1988).

(31) W. Schnelle, E. Braun, H. Broicher, R. Dömel, S. Ruppel, W. Braunisch, J. Harnischmacher and D. Wohlleben, *Physica C* **168**, 465 (1990).

(32) A.K. Bandyopadhyay, P. Maruthikumar, G.L. Bhalla, S.K. Agarwal and A.V. Narlikar, *Physica C* **165**, 29 (1990).

(33) Y. Gao, J.E. Crow, G.H. Myer, P. Schlottmann and J. Schwegler, *Physica C* **165**, 340 (1990).

(34) M.K. Yu, J.P. Franck and S. Gygax, *Physica B* **165**, 1339 (1990).

CHAPTER 6

IMAGING OF A THIN FILM

SUPERCONDUCTOR BY PHOTOTHERMAL

CONDUCTIVITY MODULATION

*"May not bodies receive much of their activity from the particles
of light which enter into their composition?"*

— Isaac Newton, 'Opticks', (1730)

6.1 INTRODUCTION

The discovery of superconductors with $T_c > 77K$ [1] immediately led to suggestions of many practical applications of these new materials: superconducting power lines, magnetically levitated trains, fast computers, etc. While interest in these futuristic applications has lowered considerably, superconducting thin films are now showing the most promise for immediate commercialization. Potential applications of thin films include IR detectors and bolometers [2], electronic components and communications systems [3].

An important parameter of a thin film is its current carrying ability, which is characterized by the critical current density, J_c. As the current increases and exceeds J_c, the film no longer carries current without loss. Electronics applications require critical current densities of 10^5-$10^6 A/cm^2$. Such densities require high quality films, which can be manufactured using both physical and chemical deposition methods. To date, the *in situ* physical deposition methods such as laser ablation, electron beam evaporation and molecular beam epitaxy have been the most successful [4]. Also, of the three classes of high-T_c superconductors, $YBa_2Cu_3O_{7-y}$ is considered the most promising for applications. Difficulties in obtaining pure phase films in the Bi and Th based superconductors are a current problem.

The electrical conductivity of the cuprate superconductors is highly anisotropic, being lowest in the c direction of the crystal structure. True epitaxial structure, with the c axis aligned perpendicular to the substrate and alignment of the a and b axes across the whole film, is required for high quality films. Several anomalous features in superconducting films have

been reported including stacking defects [5], grain boundaries [6] and spirals [7,8]. The last of these are believed to be responsible for magnetic flux pinning in the $YBa_2Cu_3O_{7-y}$ superconductors, necessary for high critical current densities. Other types of defects can be detrimental to the film.

In this Chapter, photothermal conductivity modulation (PCM) is used for imaging the resistive properties of a $YBa_2Cu_3O_{7-y}$ thin film deposited *in situ* on MgO by laser ablation. PCM is used to make spatial measurements of the differential resistivity, $d\rho/dT$, of the sample. It thus can be used for identifying transition temperatures at different locations in the film and imaging inhomogeneities of this parameter.

6.2 EXPERIMENTAL

A thin film high-T_c superconductor was characterized by resistance measurements, PCM and SEM. The material is $YBa_2Cu_3O_{7-x}$, deposited on MgO substrate by laser ablation with an approximate thickness of 0.30-μm and a 10-mm$\times$11-mm area[1]. The optical density of the film was estimated to be greater than 3.0. The film is mainly c-axis oriented with a J_c of about $6\times10^4/cm^2$ at 77K. The contacts on the corners are indium. Thin copper leads (135-μm diameter) were attached to the contacts with silver epoxy.

A rectangular 4-probe arrangement, Figure 6.1, was used for ac resistance measurements. In this arrangement, current passes through two adjacent leads while the voltage is measured across the opposite leads. The resistivity, ρ, can be calculated from the following equation [9],

---
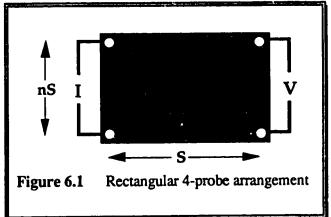
1   This film was manufactured at the National Research Council of Canada and was supplied by Dr. Peter Grant.

$$\rho = \frac{2\pi S}{2 - \left(\frac{2}{\sqrt{1 + n^2}}\right)} \frac{V}{I}$$

(6.1)

where n and S are identified in the figure, V is the measured voltage, and I is the current. With this arrangement, the voltage was found to be 90° out of phase with the current.

The instrumentation for PCM measurements and image collection has been described in Chapters 4 and 5. A 20-mW argon-ion laser beam with 15-μm spot size was used for all measurements unless otherwise specified. Sideband detection for optical modulation frequencies of 0.5 - 3.5-kHz was used for image collection while a two lock-in detection system was used for lower optical frequencies. Typically, 10-mA rms currents were used for image collection. The ac current frequency was 1 to 8-kHz for image collection, dependent on the optical frequency used. SEM images were collected on a Cambridge S250 system with 20-kV electron beam.

Figure 6.1   Rectangular 4-probe arrangement

6.3   RESULTS AND DISCUSSION

The temperature dependence of the resistance of the film, Figure 6.2, is typical of a high quality material. The resistivity above the transition is linear with temperature, with an extended y-axis intercept of ~ -20K. The expansion of the transition area in Figure 6.3b shows a 3.5K wide resistive transition (0-90%). The PCM amplitude in Figure 6.3a was recorded with 10-Hz optical
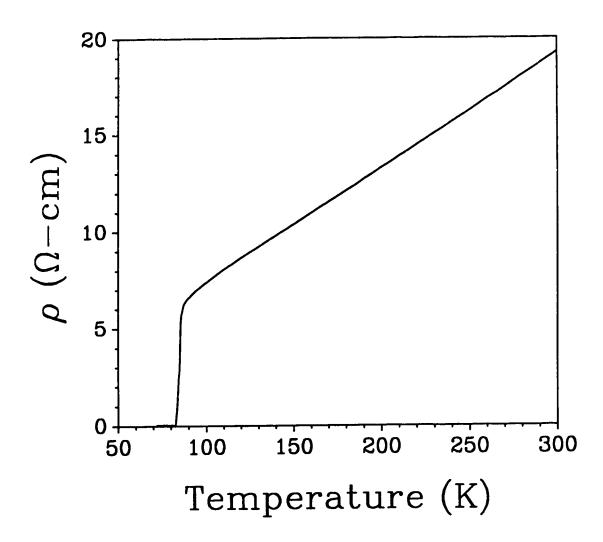
Figure 6.2 Temperature dependence of the resistivity of a $YBa_2Cu_3O_{7-y}$ thin film deposited on MgO by laser ablation.
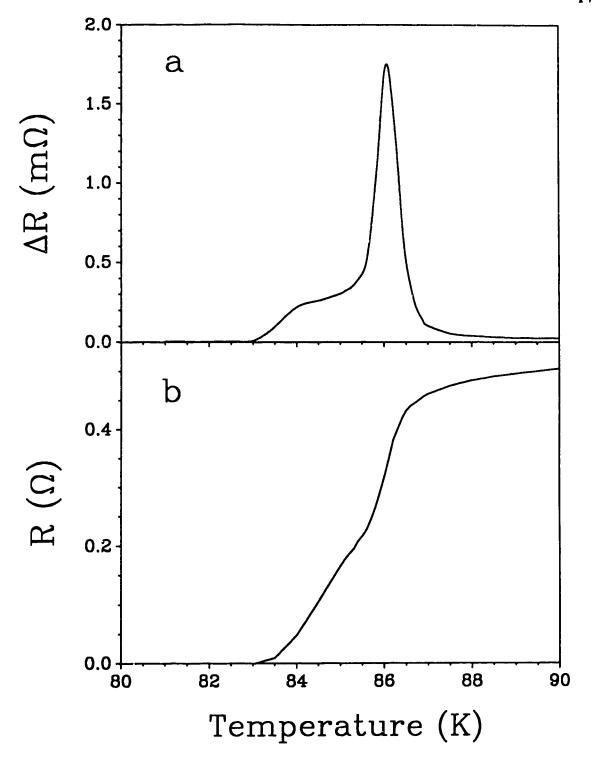
Figure 6.3 Temperature dependence of the PCM amplitude (a) and resistance (b) of a $YBa_2Cu_3O_{7-y}$ thin film superconductor. Two components to the transition can be seen in each figure. PCM conditions: P=6-mW beam (488-nm), I=10-mA rms and f=10-Hz optical modulation.

modulation, 6-mW beam and a 2-mm spot size on the center of the film. The rms amplitude, ΔR, is given by $\Delta R = \Delta V / I$, where ΔV is the rms voltage measured by the lock-in amplifier and I is the current. One clearly sees the derivatized nature of this signal, which is proportional to dR/dT of the bulk material. There appear to be two components to the amplitude, a very sharp peak at 86K and a broad tail extending to zero at the transition temperature, 83K. Unlike results from the previous work on polycrystalline $Bi_{2-x}Pb_xSr_2Ca_2Cu_3O_{10+y}$ samples, the tail in this peak was insensitive to current in the range 0.2 to 11-mA. This observation suggests that the source of the tail is not a critical current effect. This is not surprising. The estimated J_c from the supplier is $6 \times 10^4 A/cm^2$ at 77K. A 10-mA current through this sample would produce a current density of only $300 \ A/cm^2$.

Figure 6.4 shows two images of the PCM amplitude (z) as a function of position (x,y) on the thin film. Shorthand notation, (x-mm,y-mm), will be used to discuss the x and y coordinates of the film. The images were collected at 86K, the temperature of the main transition, and 85K, the temperature of the resistive tail. The first observation is that there are very strong signals associated with certain areas on the film. Secondly, the area of peak signal changes with temperature, indicating that the film may have variations in its composition. In Figure 6.5, images collected at different temperatures have been converted to contour plots. The contour intervals are evenly spaced at 200-nV intervals. The four temperatures are all within the 3 to 4K window of the resistive transition. The resistance of the film at temperatures very close to T_c seems to be associated with the lower right quadrant of the film. Visual observation of the film in the lower right quadrant reveals two main cleavage lines running diagonally across the sample, whose approximate location has
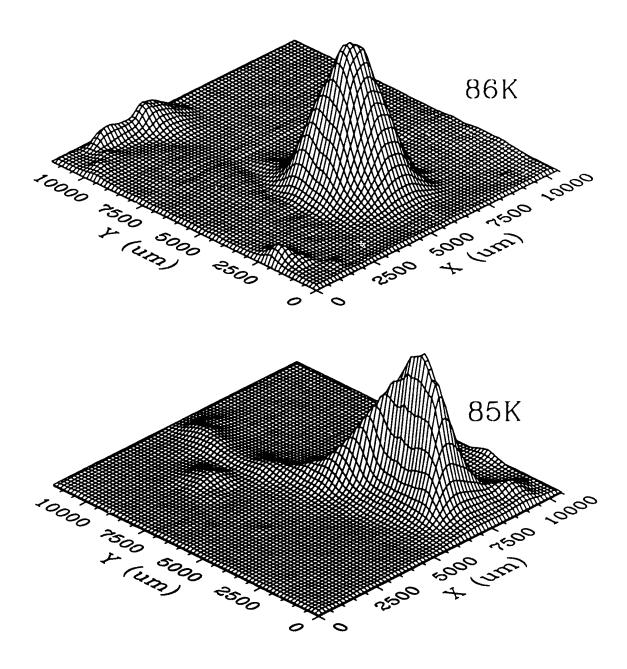
Figure 6.4   PCM images of the thin film superconductor recorded with 500-Hz optical modulation and 150-μm pixels. The images, collected at 86-K and 85-K, identify regions on the film with different transition temperatures.
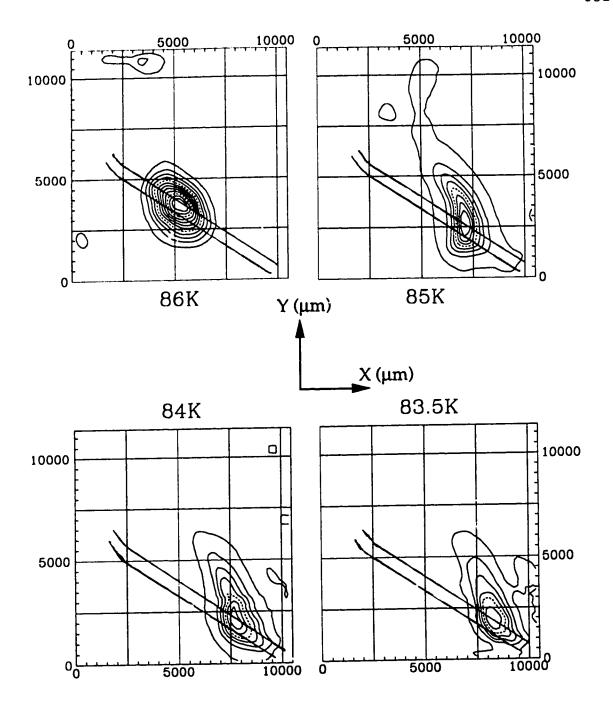
Figure 6.5 Contour plots of the PCM images recorded with f=500-Hz. The location of cleavage lines in the sample are drawn. The indicated temperatures are all within the 4K temperature range of the bulk resistance transition. Contours are evenly spaced at 200-nV intervals.

been drawn in Fig. 6.5. An SEM micrograph of one of the cleavage lines, Plate 6.1, reveals a double step in the substrate. The small balls scattered on the surface were found to be enriched with Y by energy dispersive X-ray analysis. There is evidence from electron diffraction analysis that the balls are actually Y_2BaCuO_y, formed during the laser ablation deposition process [10].

Higher resolution PCM images of the areas associated with the cleavage lines are presented in Figure 6.6 for three different temperatures. The x and y offsets are indicated on the axes. All three images show evidence of the diagonal cleavage lines, shown by arrows, running through the area of maximum intensity. Also seen in the 85.8K and 84.8K images are curious periodicities running at a 45° degree angle in the film, roughly perpendicular to the cleavage lines. The spacing of this periodicity has been estimated from these and other images to be 170±20μm.

The temperature dependence of the PCM amplitude was recorded at different locations on the film using an optical frequency of 1-kHz, Figure 6.7. The transition occurs at different temperatures, but all within the 4K window of the bulk resistance transition. The transition is as narrow as 0.55K (FWHM) or ~ 1-K (95% area) at the position of maximum signal in the 86K image. The occurrence of peaks at different temperatures suggests compositional inhomogeneity in the film. There was some question as to the centering of the substrate with respect to the laser plume at the time of the manufacturing of this film [10].

Several experiments were done to test for artifacts in the image. To test the effect of a change in current path, the current leads were rotated 180° from the (0,10); (10,10) positions to the (0,0); (10,0) positions. The voltage leads were
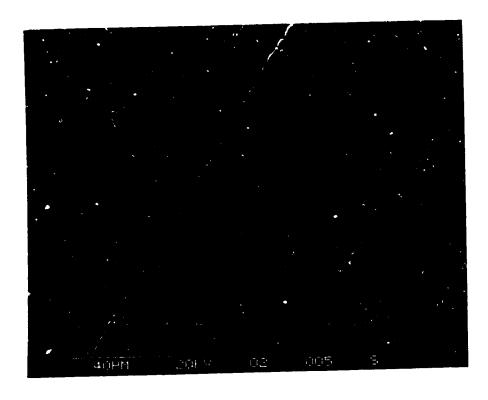
Plate 6.1 SEM micrograph of one cleavage line of the MgO substrate, onto which the thin film superconductor, YBa2Cu3O7-y, is deposited. The cleavage line is actually seen as two steps in the substrate. The small balls, artifacts of the laser ablation deposition process, are rich in Y.
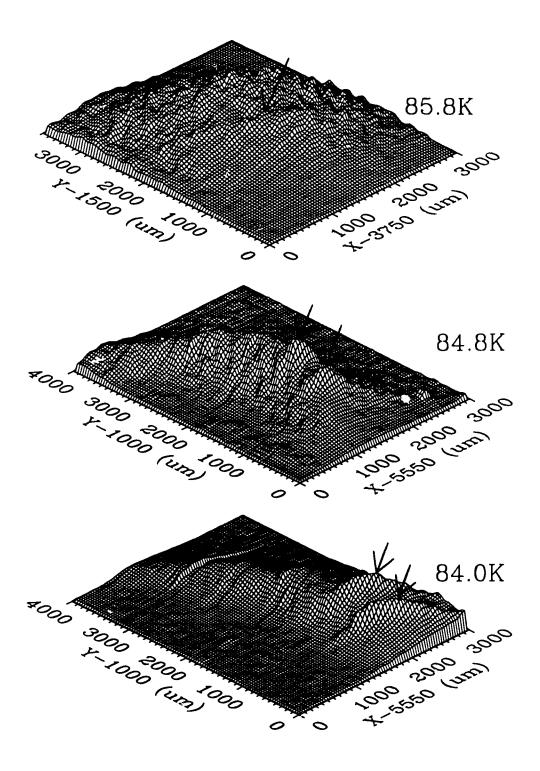
Figure 6.6   PCM images of the thin film with 1-kHz optical modulation and 40-μm pixels. Positional offsets are indicated. Two diagonal cleavage lines traverse the main signal areas of the 84.8K and 84.0K images. Periodicity is seen perpendicular to these lines with 170-μm spacing.
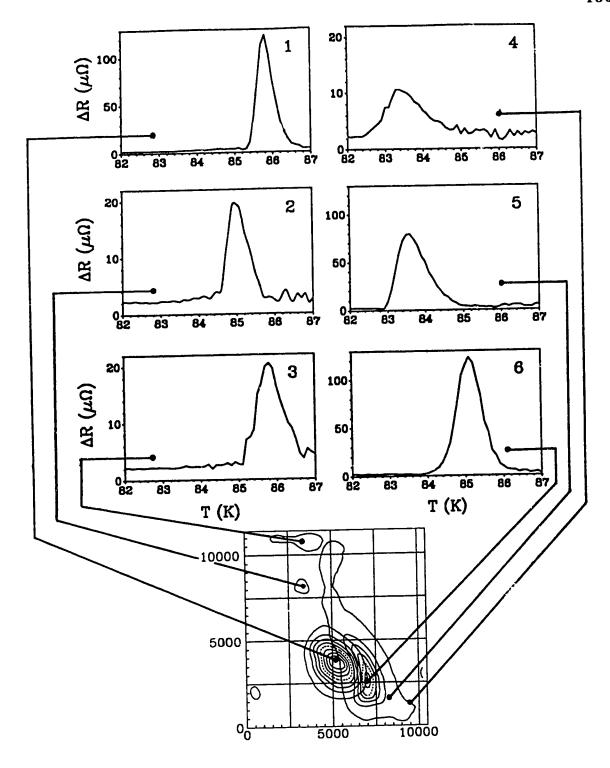
Figure 6.7 Temperature dependence of the PCM amplitude recorded at different locations on the thin film superconductor with f=1-kHz. The transition is as narrow as 0.55-K (FWHM) at position #1.

also switched accordingly. Images were collected at 86 and 85K. The contour plots were almost identical with those of Figure 6.5 with signal maximizing in the same position at the two temperatures. Another possible phenomena that could cause artifacts is a temperature gradient in the film or substrate. For example, one might question the magnitude of heat input into the film from connecting wires. In this type of system, the heat input from a single wire of the dimensions used is ~ 30-mW [11]. To test the effect of such a heat source on the film, the temperature dependence of the PCM amplitude was collected at locations #1 and #6 (see Figure 6.6) for laser powers from 5 to 30-mW. There was no observable shift of the peaks within the ±0.2K temperature uncertainty. A shift would be expected if a 30-mW heat source was capable of heating the film. Such shifts, on the order of 1K, were seen for measurements on the bulk polycrystalline samples of Chapters 4 and 5. The thermal diffusivity of the MgO substrate, 79.9 cm^2sec^{-1} at 20°C [12], is orders of magnitude larger than that of a polycrystalline material of the types used in those studies, 0.019cm^2sec^{-1} at room temperature [13] or 0.030cm^2sec^{-1} at 72K [14]. It appears that temperature gradients in the film do not arise from heat input or poor thermal coupling of the sample to the refrigerator cold finger.

The last possible mechanism for a temperature gradient in the sample would be if the cold finger itself were not isothermal. This was easily tested by rotating the film by 180°. Images were again collected and are presented in Figure 6.8. The features at ~ 86K and 84.5K also appear to be rotated 180° with respect to Figure 6.5. Based on these observations, it is believed that temperature gradients in the film are insignificant. To test the current dependence of the observed features, images were collected at 84.5K with currents of 1-mA and 4-mA, lower than the 10-mA used for all other images.

The features were not dependent on this parameter. The above tests are taken as strong evidence that the features in these images arise from properties of the film, and are not an artifact.

Figure 6.8 also shows the location of two high resolution images, a and b, which are presented in Figure 6.9. Optical modulation of 3-kHz was used at 84.5K to collect these images. Figure 6.9a reveals one of the cleavage lines. Enhanced signal is seen at the cleavage line. Figure 6.9b was taken in an area away from the cleavage line. A rippling effect is seen in this image with lines running roughly parallel to the main cleavage lines with a regular spacing of 21 ± 1-um.

It is seen from Figures 6.5, 6.6, 6.8 and 6.9 that the location of maximum signal originates on the cleavage lines. Just above $T_c(R=0)$, the signal first appears in the (10,0) corner of the film in Figure 6.5, on and around the cleavage line. This would suggest that this is the location of poorest material in the film. As the temperature increases the voltage peak slides along the cleavage lines as other points in the film weaken. Coincidentally, there is a shift in transition temperature, suggesting the possibility of inhomogeneity in the film.

The maximizing of signal along the cleavage line is most likely associated with a discontinuity in the epitaxial film structure, much like a grain boundary. The limitation of critical current densities in thin films by grain boundaries has been well documented [15,16]. In one study on thin films by low-temperature scanning electron microscopy (LTSEM) [17], it was found that the critical current density in $YBa_2Cu_3O_{7-y}$ thin films can be highly inhomogeneous. It was suggested that substrate imperfections or precipitates in the film could be responsible for this.
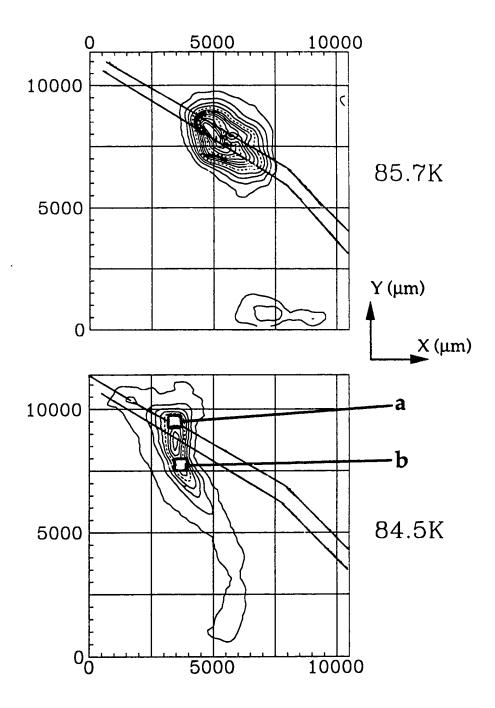
Figure 6.8   Contour plots of the PCM images recorded with 3-kHz optical frequency.after rotation of the film by 180°. Approximate location of two main cleavage lines are shown. Areas of maximum signal are associated with the cleavage lines.Contours are evenly spaced at 100-nV intervals. Areas of high resolution images, Fig. 6.9, are indicated.
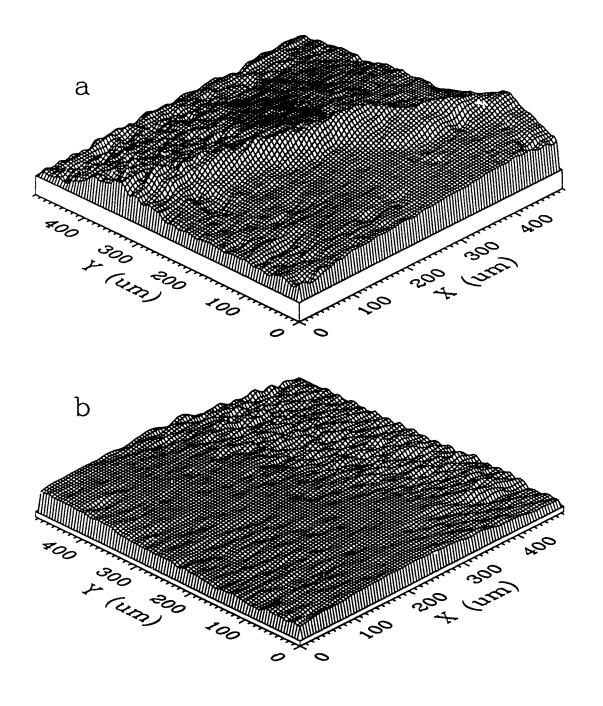
Figure 6.9   High resolution images of the areas on the thin film superconductor
indicated in Figure 6.8. (a) a cleavage line can be seen (b) an
unidentified periodicity with spacing of 21-μm is seen running parallel
to the main cleavage lines. T=84.5K, f=3-kHz.

The source of the resistive tail in Figure 6.3a is not believed to be a critical current effect, but rather, a shift in T_c due to some other inhomogeneity. This inhomogeneity is likely related to the laser ablation process. For example, Singh et al reported Ba/Y ratios that varied by 5% across a 2-cm×2-cm film of the same material and substrate as the one used in this study [18]. Such a variation could easily account for a variation in T_c of 4K. The enhancement of the signal at the cleavage lines might be a critical current effect. If the material at the cleavage line has a smaller J_c than the material around it, a slight shift in transition temperature will result when the current is greater than zero. Another possible source for this enhancement is a variation in the chemical stoichiometry at the cleavage line [19].

The strange periodicities of 21-μm and 170-μm observed in these images are unexplained. They are much too large to be associated with crystal structure of the substrate. They are also much larger than expected flux pinning structures, which are a micrometer or less [7,8,20,21]. Flux pinning structure would only be expected in the presence of large magnetic fields in any event. The periodicities that run parallel to the main cleavage lines may be a result of other smaller cleavage lines in the film. Some of these were seen visually.

A measurement of the critical current density in thin films is usually done by measuring I-V curves, a transport method, or by magnetic measurements that do not require conduction through the whole sample. A measurement of the bulk films critical current density by transport phenomena reflects the weakest link in the film. This is not so for magnetic

measurements. Inhomogeneities in J_c across films are expected to account for differences in the measurement of this parameter by the two methods [22]. Another method for measurement of J_c is LTSEM [23]. Unlike the other methods, LTSEM allows spatial imaging of the critical current density in thin films. Locations of a weak link can be identified as well as locations of higher J_c. In LTSEM, high currents are employed at temperatures well below the transition temperature. Thermal modulation of the sample by the electron beam results in a modulation of the I-V characteristics of the sample. Below the critical current, no voltage is observed. At the lowest critical current in the film, I_c, a voltage signal appears somewhere in the film. With an increase in the current, other regions of higher J_c are identified. In this way, LTSEM can probe the superconducting phase boundary of materials in the film by an increase in the current.

To contrast this, the PCM method presented here allows a probing of the superconducting phase boundary at low magnetic field by imaging of the film as a function of temperature. In this way, the low magnetic field transition temperatures of the material are imaged. Both types of measurements, low current PCM and high current LTSEM, will be useful in characterization of thin films.

6.4 CONCLUSIONS

Inhomogeneities in a thin film superconductor have been imaged by photothermal conductivity modulation. Spatial measurements of the transition temperature of the material across the film have been made. There are locations on the film where the transition is very sharp, ~1K for a 95% transition, and a transition temperature 2K higher than the bulk. Regions of

lower transition temperature appear to be associated with one quadrant of the film that may reflect a misalignment in the deposition process. Enhancement of signal is seen at cleavage lines in the substrate where disturbance of the epitaxial film structure is expected to occur. It is suggested that this enhancement may be a critical current effect.

PCM could well be applied to critical current imaging in thin films, much like what has been done with LTSEM [15,23]. A cryogenic system with increased cooling will be needed for this type of experiment, to counteract resistive heating at the contacts. Ideally, a complete characterization of thin films would involve probing of the superconducting phase boundary at a number of locations. This could be done by imaging the film as a function of temperature as the current is increased, or visa-versa.

The spatial resolution of PCM in this study is ~20-μm, at 3.0-kHz modulation frequency. The variation in signal with optical modulation frequency is shown in Figure 6.10. The signal presented in the graph is the maximum signal in the temperature dependent PCM amplitude peak recorded as a function of chopping frequency at position #1 on the film. The logarithmic fit to the data showed a signal dependence of the following form

$$\Delta V_{rms} = C \, f^{-0.44} \qquad (6.2)$$

where ΔV_{rms} is the measured voltage signal, C is a constant and f is the optical frequency. This rate of signal decrease with modulation frequency, close to an inverse square, is much slower than seen for bulk samples. S/N ratios should decrease even slower due to lower environmental noise at higher frequencies. This slow frequency dependence should permit the use of higher modulation frequencies quite readily to attain improved spatial

resolution. Acousto-optic modulation might be be used for this purpose. Improved optical design would also be needed to obtain a smaller spot size on the sample surface within the cryogenic system. Such steps will improve this technique for better characterization of superconducting thin films.
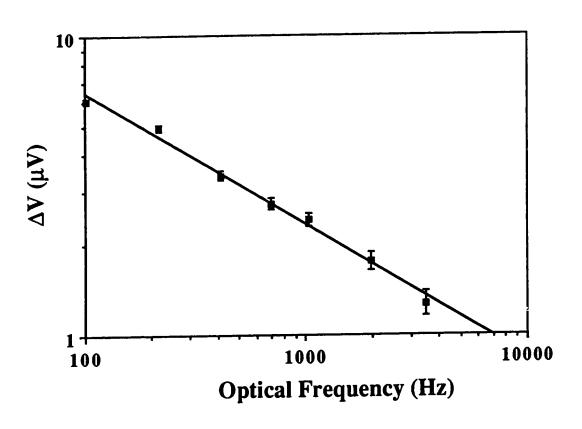
Figure 6.10 Optical frequency dependence of the PCM amplitude signal recorded at position #1 on the film. The least squares fit to the data was $\Delta V = 49.9 \mu V * f^{-0.442}$.

REFERENCES

(1) M.K. Wu, O. Wang, J.R. Ashburn, C.J. Toring, R.H. Hor, R.L. Meng, L. Gao, Z.J. Huang, *Phys. Rev. Lett.* **58**, 908 (1987).

(2) A.R. Tebo, *Las. Foc.World.* **27**, A37 (1991).

(3) I. Imato, *Science* **251**, 1564 (1991).

(4) M. Schieber, *J. Crys. Grow.* **109**, 401 (1991).

(5) R. Ramesh et al., *Science* **247**, 57 (1990).

(6) M.F. Chisholm and S.J. Pennycook, *Nature* **351**, 47 (1991).

(7) M. Hawley, I.D. Raistrick, J.B. Beery and R.J. Houlton, *Science* **251**, 1587 (1991).

(8) C. Gerber, D. Anselmetti, J.D. Bednorz, J. Mannhart and D.G. Schlom, *Nature* **350**, 279 (1991).

(9) W.R. Runyan, *"Semiconductor Measurements and Instrumentation"*, Texas Instruments Electronic Series, McGraw-Hill, New York (1975).

(10) private communication, P. Grant, Science Affairs Office, NRC, Ottawa.

(11) "MMR User Manual", MMR Technologies Inc., Mountain View, CA.

(12) N.J. Dovichi, *CRC Crit. Rev. Anal. Chem.* **17**, 357 (1987).

(13) J.T. Fanton, D.B. Mitzi, A. Kapitulnik, B.T. Khuri-Yakub, G.S. Kino, D. Gazit and R.S. Feigelson, *Appl. Phys. Lett.* **55**, 598 (1989).

(14) R. McLaren and N.J. Dovichi, *J. Appl. Phys.* **68**, 4882 (1990).

(15) J.Mannhart, R. Gross, K. Hipler, R.P. Huebener, C.C. Tsuei, D. Dimos and P. Chaudhari, *Science* **245**, 839 (1989).

(16) P. Chaudhari, J. Mannhart, D. Dimos, C.C. Tsuei, J. Chi, M.M. Oprysko and M. Scheuermann, *Phys. Rev. Lett.* **60**, 1653 (1653).

(17) R. Gross, K. Hipler, J. Mannhart, R.P. Huebener, P. Chaudhari, D. Dimos, C.C. Tsuei, J. Schubert and U. Poppe, *Appl. Phys. Lett.* **55**, 2132 (1989).

(18) R.K. Singh, N. Biunno and J. Narayan, *Appl. Phys. Lett.* **53**, 1013 (1988).

(19) S.E. Babcock and D.C. Larbalestier, *Appl. Phys. Lett.* **55**, 393 (1989).

(20) N.W. Ashcroft, N.D. Mermin, *"Solid State Physics"*, Saunders College, Philadelphia (1976) pg. 733.

(21) P.H. Kes, *Nature*, **350**, 192 (1991).

(22) E.G. Swartz, B.A. Judd, E. Batalla, L.S. Wright, W.D. MacDonald, A.J. Otto and H. Sang, *J. Low Temp. Phys.* ,**74**, 277 (1989).

(23) R.P. Huebener in *Advances in Electronics and Electron Physics* 70, P.W.Hawkes, Ed., 1 (Academic, New York, 1988).

CHAPTER 7

CONCLUSIONS

AND

FUTURE DIRECTIONS

In this thesis, Photothermal Conductivity Modulation (PCM) has been applied both for absorbance measurements in solution and for characterization of high temperature superconductors (HTS). Like other photothermal methods, PCM has the capability of obtaining information about the absorptivity and thermal properties of the sample. In addition to this, PCM can be used to measure electrical properties of the sample.

Absorbance measurements are a traditional area of photothermal methods. Because nonradiative relaxation and heat generation follow directly from absorbance, photothermal methods in principle represent a more direct method of measuring absorbance than conventional measurements. Absorbance measurements in solution by TMEC were discussed in Chapters 2 and 3. The sensitivity of the measurement in this application is a function of the temperature coefficient of viscosity of the solvent. Because this parameter is very high for water, 2.5%/$^{\circ}$C, sensitive absorbance measurements in volumes less than a nanoliter could be made. To attest to this sensitivity, the absorbance of distilled water was measured with a small 5-mW helium neon laser in a volume of only 230-pL. The future application of this method is thus clearly designed for microanalysis. A future application of the method would be absorbance detection in capillaries with on column conductivity detection [1] combined with electrophoretic separation.

Absorptivity information was not obtained in the application of PCM to high-T_c superconductors. Because all the samples were opaque, the full laser power was absorbed, allowing no mechanism for absorptivity differentiation. This could change with the processing of thinner

superconducting films. For example, 50-μm thin film bolometers of $YBa_2Cu_3O_{7-y}$ material are presently being made for radiation detection beyond 20-μm [2]. The optical density of this film would be expected to be about 0.5, 30% transmission. If one were to characterize such a film by PCM, variations in the absorptivity of the film would generate variations in the signal. With advance imaging of the film in a transmission mode, a correlation between absorptivity and PCM images at different temperatures might be made. Both resistive properties and absorptivity would have to be taken into account for interpretation of the results.

Thermal property measurements were also demonstrated in this thesis. In Chapter 3, the solvent constant of absorbance sensitivity, K_s, was measured in different solvents. This parameter was shown in Eq. 3.29 to be related to the heat capacity and viscous activation energy of the solvent, E^*. Water was found to have an unusually high sensitivity in TMEC, which contrasted to other photothermal methods that show a poorer sensitivity in water compared to organic solvents. The reason for the difference here is the dependence of the TMEC signal on E^*, which is large in water compared to other solvents. It was also shown in Chapter 3 that a significant increase in sensitivity can be achieved in mixed solvents due to an increase in E^*.

Other thermal property measurements were made in the high temperature superconductor work. In Chapter 4, the thermal diffusivity of a BiSrCaCuO polycrystalline material was estimated by measurement of the frequency dependence of heat flow to a defect in the sample. In Chapter 5, the possibility of measuring heat capacity discontinuities at the transition temperature of bulk superconductors was discussed after presentation of preliminary data which showed evidence for such an effect. Such

measurements could only be made on bulk samples where the signal is directly related to the heat capacity. One would not expect to see such effects on thin film samples, for example, where the signal is only related to the thermal properties of the substrate and the thermal coupling of the film to the substrate. Indeed, observation of the high frequency temperature spectra of a thin film in Figure 6.7 reveals no discontinuities in the peaks such as those seen in Chapter 5 with bulk samples. Measurement of the heat capacity jump at T_c by PCM is an area that could be pursued in the future since this parameter reveals clues to the superconductive mechanism [3]

The ability to measure electrical properties by PCM extends the application of photothermal methods to new areas of analysis. In solution, electric property measurement was first touched upon in Chapter 3. There, it was shown that the spatially resolved TMEC signal between the electrodes reflected the magnitude of the electric field, and hence the current density at the point of the measurement. In Chapters 4, 5 and 6, electrical property measurements of superconductors were dealt with almost exclusively. In this application, the signal is proportional to the differential resistivity of the material. At the transition temperature, large signals are generated. Collection of this signal as a function of the beam position formed the basis for a new imaging method. The somewhat large volumes of the bulk polycrystalline samples of Chapters 4 and 5 limited the sensitivity of this type of measurement. The low sensitivity, in turn, limited the spatial resolution by requiring that low optical modulation frequencies be used (10-400-Hz). The decreased volume of a thin film superconductor in Chapter 6 gave much improved signal to noise ratios. Optical modulation of a few kilohertz was possible and spatial resolution of ~20-μm was obtained. Increases in

resolution can be obtained by going to higher optical modulation frequencies and smaller laser beam spot sizes. Acousto-optic modulation might be used for this purpose. Improved optical design would also be needed to obtain a smaller spot size on the sample surface within the cryogenic system.

PCM could well be applied to critical current imaging in thin films in the future. This type of measurement is currently done with low temperature scanning electron microscopy [4,5]. The reduced cost of a laser system for this type of measurement would make it more available to researchers wanting to characterize thin films. The critical current imaging could be combined with low-current T_c-imaging, of the type presented in Chapter 6, to fully characterize the thin film with respect to the superconducting phase boundary. While $YBa_2Cu_3O_{7-y}$ thin films are becoming well developed, the Bi and Th superconducting thin film systems are slightly behind [6]. The increased transition temperature of these systems will eventually encourage their development. PCM would be an excellent tool for characterizing these new systems. In doing this type of work though, one would have to keep in mind the superconducting researcher's code of success . . . always follow the path of least resistance!

REFERENCES

(1) X.H. Huang, T.K. Pang, M.J. Gordon and R.N. Zare, *Anal. Chem.* **59**, 2747 (1987).

(2) A.R. Tebo, *Las. Foc.World.* **27**, A37 (1991).

(3) R. Jin, F. Shi, Q. Ran, N. Shi, Z. Shi and S. Zhou, *Physica C* **158**, 255 (1988).

(4) J.Mannhart, R. Gross, K. Hipler, R.P. Huebener, C.C. Tsuei, D. Dimos and P. Chaudhari, *Science* **245**, 839 (1989).

(5) R. Gross, K. Hipler, J. Mannhart, R.P. Huebener, P. Chaudhari, D. Dimos, C.C. Tsuei, J. Schubert and U. Poppe, *Appl. Phys. Lett.* **55**, 2132 (1989).

(6) M. Schieber, *J. Crys. Grow.* **109**, 401 (1991).

APPENDIX C

COMPUTER PROGRAMS

PROGRAMS

Several programs written by the author are presented in this section. It is not intended to be a complete listing of all programs used in this work. Instead, a few sample programs are included. All programs were written in BASIC on an 80286-PC computer. An IEEE-488 interface was used for control and data collection from the various pieces of electronic equipment. The interface consisted of a GP488A interface board and Driver488 software, both parts of the Personal488 system available from IOtech, Inc. The driver commands used in the programs can be found in the Personal488 User's Manual. Mnemonic commands for communication with the lab equipment: Newport Model 855 Programmable Controller, MMR Inc. Model K-20 Temperature Controller, Ithaco Model 3961 Lock-in Amplifiers, and a Keithley Model 195 Digital Multimeter, can be found in the appropriate manuals.

Three programs used for theoretical calculations are presented: PULSE, STEP, and TRAIN. These programs were used for generation of the impulse response functions, step response functions and square wave response functions respectively in Chapter 3. The derivations of the mathematical equations are given in that Chapter.

Two data collection programs are presented, MODULAT3 and SBSCAN. The first program was used for collection of thermal modulation amplitude and phase spectra with a two-lock-in detection scheme, Chapters 4 & 5. The latter program was used to collect the data, with single sideband detection, for the amplitude and phase images presented in Chapters 5 & 6.

Program PULSE

```
10 'PROGRAM PULSE
20 '
30 W = .000013                              'spot size in meters
40 L = .00005                               'electrode separation
50 R = .000038                              'electrode radius
60 EC = .001                                'absorp-conc product in inverse meters
70 FILE$ = "JAN2390.D1"                     'output data file name
80 TTCMAX = 50                              'maximum t/tc ratio
90 TTCDEL = .1                              'point separation
100 '
110 TTC = 0                                 'initialize t/tc value
120 OPEN "O",#1,FILE$                       'open data file
130 '
140 K = 2*R^2/W^2/(1+2*TTC)                 'calculate K
150 Z = L/W/SQR(2*(1+2*TTC))                'calculate Z
160 '
170 GOSUB 2000                              'ERF(Z) SUBROUTINE
180 '
190 GOSUB 3000                              'F(1/2,2;-K) SUBROUTINE
200 '
210 '      next calculate DELI = (delta I)/EI
220 DELI = 1.07679E-08*EC/W/L/SQR(1+2*TTC)*ERF*HYP
230 '
240 PRINT #1,USING"##.##";TTC;:PRINT #1," ";DELI  'print result to file
250 PRINT USING "##.##";TTC; : PRINT " ";DELI     'print to screen
260 '
270 IF TTC < TTCMAX THEN TTC = TTC+TTCDEL : GOTO 130
280 END
2000 '-------2000-----SUBROUTINE ERF(Z)-------------------------------------
2010 '
2020 IF Z > 2.7 THEN ERF = 1 : GOTO 2160          'close enough
2030 IF Z <-2.7 THEN ERF =-1 : GOTO 2160          'close enough for Rock'n Roll
2040 SUM = Z
2050 N = 1
2060 '
2070 FACT2N = 1
2080 FOR J = 1 TO 2*N+1 STEP 2
2090 FACT2N = FACT2N*J
2100 I = I+1
2110 NEXT J
2120 SUMN = 2^N * Z^(2*N+1) / FACT2N
2130 SUM = SUM + SUMN
2140 IF ABS(SUMN) > .00001 THEN N=N+1 : GOTO 2060
2150 ERF = 1.128379*EXP(-1*(Z^2))*SUM
2160 RETURN
3000 '-----3000------SUBROUTINE HYPER(K)------------------------------------
3010 ER = .0001                             'convergence tolerance
3020 HYP = 1                                'initialize sum and sum index
3030 N=1
3040 '
3050 GOTO 3180                              'N! SUBROUTINE
```

Program PULSE - continued

```
3060 '
3070 GOTO 3330                         '(2n-1)!! SUBROUTINE
3080 '
3090 GOTO 3480                         '(K/2)^2 SUBROUTINE
3100 'calculate sum element OF123 & OF456 are overflow buffers
3110 SUM1 = (-1)^N*FACT2N/FACTN*POW/FACTN/(N+1)      'calculate sum element
3120 OF123 = OF2N1/OFN1*OF2N2/OFN2*OF2N3/OFN3*OFP1/OFN1*OFP2/OFN2-
     *OFP3/OFN3
3130 OF456 = OF2N4/OFN4*OF2N5/OFN5*OF2N6/OFN6*OFP4/OFN4*OFP5/OFN5-
     *OFP6/OFN6
3140 SUMN = SUM1*OF123*OF456
3150 HYP = HYP + SUMN                  'recalculate sum
3160 IF ABS(SUMN) > ER THEN N=N+1 : GOTO 3040   'calculate next element
3170 RETURN                            'finished
3180 '--------------------N! sub-SUBROUTINE
3190 FACTN = 1                         'initialize factorial product
3200 OFN1 = 1 : OFN4 = 1               'initialize overflow buffers
3210 OFN2 = 1 : OFN5 = 1
3220 OFN3 = 1 : OFN6 = 1
3230 FOR J=1 TO N
3240 FACTN = FACTN*J
3250 IF FACTN > 1.01E+25 THEN FACTN = FACTN*.00001 : OFN1 =
     OFN1*100000!
3260 IF OFN1 > 1.01E+25 THEN OFN1 = OFN1*.00001 : OFN2 = OFN2*100000!
3270 IF OFN2 > 1.01E+25 THEN OFN2 = OFN2*.00001 : OFN3 = OFN3*100000!
3280 IF OFN3 > 1.01E+25 THEN OFN3 = OFN3*.00001 : OFN4 = OFN4*100000!
3290 IF OFN4 > 1.01E+25 THEN OFN4 = OFN4*.00001 : OFN5 = OFN5*100000!
3300 IF OFN5 > 1.01E+25 THEN OFN5 = OFN5*.00001 : OFN6 = OFN6*100000!
3310 NEXT J
3320 GOTO 3060
3330 '---------2N-1!! SUB-SUBROUTINE
3340 FACT2N = 1                        'initialize factorial product
3350 OF2N1 = 1 : OF2N4 = 1             'initialize overflow buffers
3360 OF2N2 = 1 : OF2N5 = 1
3370 OF2N3 = 1 : OF2N6 = 1
3380 FOR J=1 TO 2*N-1 STEP 2
3390 FACT2N = FACT2N*J
3400 IF FACT2N > 1.01E+25 THEN FACT2N=FACT2N*.00001 : OF2N1 =
     OF2N1*100000!
3410 IF OF2N1 > 1.01E+25 THEN OF2N1 = OF2N1*.00001 : OF2N2 =
     OF2N2*100000!
3420 IF OF2N2 > 1.01E+25 THEN OF2N2 = OF2N2*.00001 : OF2N3 =
     OF2N3*100000!
3430 IF OF2N3 > 1.01E+25 THEN OF2N3 = OF2N3*.00001 : OF2N4 =
     OF2N4*100000!
3440 IF OF2N4 > 1.01E+25 THEN OF2N4 = OF2N4*.00001 : OF2N5 =
     OF2N5*100000!
3450 IF OF2N5 > 1.01E+25 THEN OF2N5 = OF2N5*.00001 : OF2N6 =
     OF2N6*100000!
3460 NEXT J
3470 GOTO 3080
```

Program PULSE - continued

```
3480 '----------(K/2)^N SUB-SUBROUTINE
3490 POW = 1
3500 OFP1 = 1 : OFP4 = 1
3510 OFP2 = 1 : OFP5 = 1
3520 OFP3 = 1 : OFF6 = 1
3530 FOR J=1 TO N
3540 POW = POW*K/2
3550 IF POW > 1.01E+25 THEN POW = POW*.00001 : OFP1 = OFP1*100000!
3560 IF OFP1 > 1.01E+25 THEN OFP1 = OFP1*.00001 : OFP2 = OFP2*100000!
3570 IF OFP2 > 1.01E+25 THEN OFP2 = OFP2*.00001 : OFP3 = OFP3*100000!
3580 IF OFP3 > 1.01E+25 THEN OFP3 = OFP3*.00001 : OFP4 = OFP4*100000!
3590 IF OFP4 > 1.01E+25 THEN OFP4 = OFP4*.00001 : OFP5 = OFP5*100000!
3600 IF OFP5 > 1.01E+25 THEN OFP5 = OFP5*.00001 : OFP6 = OFP6*100000!
3610 NEXT J
3620 GOTO 3100
```

Program STEP

```
10 'PROGRAM STEP
20 '
30 W = .000015                              'spot size in meters
40 L = .00005                               'electrode separation
50 R = .000038                              'electrode radius
60 EC = 1                                   'absorp-conc product in inverse meters
70 FILE$ = "G"                              'output data file name
80 TTCMAX = 100                             'maximum t/tc ratio
90 TTCDEL = .2                              'integration period
100 MM% = 5                                 'number of integrations per printout
110 '
120 TC = 1756300!*W^2                       'time constant for water (20 C)
130 DELT = TC*TTCDEL                        'time of an integration period(sec)
140 '
150 TTC = 0                                 'initialize t/tc value
160 INTEG = 0                               'integration sum
170 OPEN "O",#1,FILE$                       'open data file
180 '
190 K = 2*R^2/W^2/(1+2*TTC)                 'calculate K
200 Z = L/W/SQR(2*(1+2*TTC))                'calculate Z
210 '
220 GOSUB 2000                              'ERF(Z) SUBROUTINE
230 '
240 GOSUB 3000                              'F(1/2,2;-K) SUBROUTINE
250 '
260 'next calculate initial DELI(t=0) = (delta I)/(I*P)
270 DELI = 1.07679E-08*EC/W/L/SQR(1+2*TTC)*ERF*HYP
280 '
290 PRINT #1,USING"##.##";TTC;:PRINT #1," ";INTEG        'print to file
300 PRINT USING "##.##";TTC; : PRINT " ";INTEG           'print to screen
310 DELIM1 = DELI                           'initial Fn-1
320 '
330 M% = 1                                  'print index - up to MM
340 '
350 TTC = TTC + TTCDEL                       'increase t/tc
360 '
370 K = 2*R^2/W^2/(1+2*TTC)                 'calculate K
380 Z = L/W/SQR(2*(1+2*TTC))                'calculate Z
390 '
400 GOSUB 2000                              'ERF(Z) SUBROUTINE
410 '
420 GOSUB 3000                              'F(1/2,2;-K) SUBROUTINE
430 '
440 '     next calculate DELIN = (delta I)/(I*P)
450 DELIN = 1.07679E-08*EC/W/L/SQR(1+2*TTC)*ERF*HYP
460 INTN = (DELIN+DELINM1)/2*DELT  'individual area element
470 INTEG = INTEG + INTN           'add area to total integral
480 '
490 IF M%<>MM% THEN M% = M%+1 : DELINM1 = DELIN : GOTO 350 'continue
        integration
```

Program Step - continued

```
500 '
510 PRINT #1,USING"##.##";TTC;:PRINT #1," ";INTEG          'print to file
520 PRINT USING "##.##";TTC; : PRINT " ";INTEG             'print to screen
530 '
540 IF TTC >= TTCMAX THEN END      'FINISHED !!
550 '
560 DELINM1 = DELIN                          'shift integration to right one pixel
570 GOTO 330                                 'continue integration with M=1
2000 '-------2000-----SUBROUTINE ERF(Z)-----------------------------------
2010 '
2020 IF Z > 2.7 THEN ERF = 1 : GOTO 2160     'close enough
2030 IF Z <-2.7 THEN ERF =-1 : GOTO 2160     'close enough for Rock'n Roll
2040 SUM = Z
2050 N = 1
2060 '
2070 FACT2N = 1
2080 FOR J = 1 TO 2*N+1 STEP 2
2090 FACT2N = FACT2N*J
2100 I = I+1
2110 NEXT J
2120 SUMN = 2^N * Z^(2*N+1) / FACT2N
2130 SUM = SUM + SUMN
2140 IF ABS(SUMN) > .00001 THEN N=N+1 : GOTO 2060
2150 ERF = 1.128379*EXP(-1*(Z^2))*SUM
2160 RETURN
3000 '-----3000------SUBROUTINE HYPER(K)----------------------------------
3010 ER = .0001                              'convergence tolerance
3020 HYP = 1                                 'initialize sum and sum index
3030 N=1
3040 '
3050 GOTO 3180                               'N! SUBROUTINE
3060 '
3070 GOTO 3330                               '(2n-1)!! SUBROUTINE
3080 '
3090 GOTO 3480                               '(K/2)^2 SUBROUTINE
3100 'calculate sum element OF123 & OF456 are overflow buffers
3110 SUM1 = (-1)^N*FACT2N/FACTN*POW/FACTN/(N+1) 'calculate sum element
3120 OF123 =
     OF2N1/OFN1*OF2N2/OFN2*OF2N3/OFN3*OFP1/OFN1*OFP2/OFN2*OFP3/OF
     N3
3130 OF456 =
     OF2N4/OFN4*OF2N5/OFN5*OF2N6/OFN6*OFP4/OFN4*OFP5/OFN5*OFP6/OF
     N6
3140 SUMN = SUM1*OF123*OF456
3150 HYP = HYP + SUMN                        'recalculate sum
3160 IF ABS(SUMN) > ER THEN N=N+1 : GOTO 3040   'calculate next element
3170 RETURN                                  'finished
3180 '--------------------N! sub-SUBROUTINE
3190 FACTN = 1                               'initialize factorial product
3200 OFN1 = 1 : OFN4 = 1                      'initialize overflow buffers
3210 OFN2 = 1 : OFN5 = 1
```

Program STEP - continued

```
3220 OFN3 = 1 : OFN6 = 1
3230 FOR J=1 TO N
3240 FACTN = FACTN*J
3250 IF FACTN > 1.01E+25 THEN FACTN = FACTN*.00001 : OFN1 =
     OFN1*100000!
3260 IF OFN1 > 1.01E+25 THEN OFN1 = OFN1*.00001 : OFN2 = OFN2*100000!
3270 IF OFN2 > 1.01E+25 THEN OFN2 = OFN2*.00001 : OFN3 = OFN3*100000!
3280 IF OFN3 > 1.01E+25 THEN OFN3 = OFN3*.00001 : OFN4 = OFN4*100000!
3290 IF OFN4 > 1.01E+25 THEN OFN4 = OFN4*.00001 : OFN5 = OFN5*100000!
3300 IF OFN5 > 1.01E+25 THEN OFN5 = OFN5*.00001 : OFN6 = OFN6*100000!
3310 NEXT J
3320 GOTO 3060
3330 '---------2N-1!! SUB-SUBROUTINE
3340 FACT2N = 1                          'initialize factorial product
3350 OF2N1 = 1 : OF2N4 = 1               'initialize overflow buffers
3360 OF2N2 = 1 : OF2N5 = 1
3370 OF2N3 = 1 : OF2N6 = 1
3380 FOR J=1 TO 2*N-1 STEP 2
3390 FACT2N = FACT2N*J
3400 IF FACT2N > 1.01E+25 THEN FACT2N=FACT2N*.00001 : OF2N1 =
     OF2N1*100000!
3410 IF OF2N1 > 1.01E+25 THEN OF2N1 = OF2N1*.00001 : OF2N2 =
     OF2N2*100000!
3420 IF OF2N2 > 1.01E+25 THEN OF2N2 = OF2N2*.00001 : OF2N3 =
     OF2N3*100000!
3430 IF OF2N3 > 1.01E+25 THEN OF2N3 = OF2N3*.00001 : OF2N4 =
     OF2N4*100000!
3440 IF OF2N4 > 1.01E+25 THEN OF2N4 = OF2N4*.00001 : OF2N5 =
     OF2N5*100000!
3450 IF OF2N5 > 1.01E+25 THEN OF2N5 = OF2N5*.00001 : OF2N6 =
     OF2N6*100000!
3460 NEXT J
3470 GOTO 3080
3480 '----------(K/2)^N SUB-SUBROUTINE
3490 POW = 1
3500 OFP1 = 1 : OFP4 = 1
3510 OFP2 = 1 : OFP5 = 1
3520 OFP3 = 1 : OFP6 = 1
3530 FOR J=1 TO N
3540 POW = POW*K/2
3550 IF POW > 1.01E+25 THEN POW = POW*.00001 : OFP1 = OFP1*100000!
3560 IF OFP1 > 1.01E+25 THEN OFP1 = OFP1*.00001 : OFP2 = OFP2*100000!
3570 IF OFP2 > 1.01E+25 THEN OFP2 = OFP2*.00001 : OFP3 = OFP3*100000!
3580 IF OFP3 > 1.01E+25 THEN OFP3 = OFP3*.00001 : OFP4 = OFP4*100000!
3590 IF OFP4 > 1.01E+25 THEN OFP4 = OFP4*.00001 : OFP5 = OFP5*100000!
3600 IF OFP5 > 1.01E+25 THEN OFP5 = OFP5*.00001 : OFP6 = OFP6*100000!
3610 NEXT J
3620 GOTO 3100
```

Program TRAIN

```
10 'PROGRAM TRAIN
20 '
30 W = .000013                              'spot size in meters
40 L = .00005                               'electrode separation
50 R = .000038                              'electrode radius
60 EC = 1                                   'absorp-conc product in inverse meters
70 FILE$ = "JAN3191.D5"                     'output data file name
80 TTCDEL = .15                             'integration period
90 MM = 11                                  'number of integrations per printout
100 BB = 40                                 'number of printouts per 1/2 cycle
110 AA = 30   'EVEN NUMBER !!               'number of 1/2 cycles
120 DIM STEPF (AA,BB+1)                      'array to hold step function values
125 DIM TRAIN (2*BB+1)               'array to hold final infinite square wave response
130 '
140 TC = 1756300!*W^2                       'time constant for water (20 C)
150 DELT = TC*TTCDEL                         'time of an integration period(sec)
160 '
170 PRINT CHR$(12)                          'clear screen
180 PRINT ,,"PROGRAM TRAIN"
190 PRINT ,,"-------------"
200 PRINT
210 PRINT "SPOT SIZE        =";W;"m",
220 PRINT "ELECTRODE RADIUS =";R;"m"
230 PRINT
240 PRINT "ELECTRODE SEPARATION =";L;"m",
250 PRINT "ABSORPTIVITY     =";EC;"m-1"
260 PRINT
270 PRINT "FREQUENCY        =";1/(2*BB*MM*TTCDEL*TC),
280 PRINT "# of CYCLES     =";AA/2
290 PRINT : PRINT
300 PRINT " A"," B","STEP FUNCTION"," t/tc"
310 PRINT "---","---","-------------","------"
320 '
330 TTC = 0                                 'initialize t/tc value
340 INTEG = 0                               'integration sum
350 OPEN "O",#1,FILE$                        'open data file
360 '
370 K = 2*R^2/W^2/(1+2*TTC)                 'calculate K
380 Z = L/W/SQR(2*(1+2*TTC))                'calculate Z
390 GOSUB 2000                              'ERF(Z) SUBROUTINE
400 '
410 GOSUB 3000                              'F(1/2,2;-K) SUBROUTINE
420 '
430 'next calculate initial DELI(t=0) = (delta I)/(I*P)
440 DELI = 1.07679E-08*EC/W/L/SQR(1+2*TTC)*ERF*HYP
450 '
460 LOCATE 14,1 : PRINT " 0"," 0"," 0","  0"       'print to screen
470 DELIM1 = DELI                           'initial Fn-1
480 '
490 FOR A = 1 TO AA
```

Program TRAIN - continued

```
500 STEPF(A,0) = INTEG              'STEPF(A,0)=STEPF(A-1,BB)
510 FOR B = 1 TO BB
520 FOR M = 1 TO MM
530 '
540 TTC=((A-1)*BB*MM+(B-1)*MM+M)*TTCDEL 'calculate new t/tc
550 K = 2*R^2/W^2/(1+2*TTC)         'calculate K
560 Z = L/W/SQR(2*(1+2*TTC))        'calculate Z
570 '
580 GOSUB 2000                      'ERF(Z) SUBROUTINE
590 '
600 GOSUB 3000                      'F(1/2,2;-K) SUBROUTINE
610 '
620 '    next calculate DELIN = (delta I)/(I*P)
630 DELIN = 1.07679E-08*EC/W/L/SQR(1+2*TTC)*ERF*HYP
640 INTN = (DELIN+DELINM1)/2*DELT   'individual area element
650 INTEG = INTEG + INTN            'add area to total integral
660 DELINM1 = DELIN                 'shift integration to right one pixel
670 NEXT M
680 STEPF(A,B) = INTEG              'store present integral to array
690 LOCATE 14,1 : PRINT A,B,: PRINT USING "##.####^^^^";INTEG,: PRINT
      USING "####.###";TTC          'print to screen
700 NEXT P
710 NEXT A
720 '                               'step function is finished!!
730 '                               'now calculate infinite square wave response
740 TRAINOFF = 0                    'initialize LASER-OFF sum
750 '
760 FOR J = 0 TO BB
770 TRAINON = 0                     'initialize LASER-ON sum
780 FOR N = 1 TO AA-1
790 TRAINON = TRAINON + (-1)^(N+1)*STEPF(N,J)  'adds all previous cycles
800 NEXT N
810 TIME = J*MM*TTCDEL*TC*1000      'time in miliseconds
820 PRINT #1,TIME;" ";TRAINON       'print time(msec),response
830 LOCATE 16,1 : PRINT TIME,TRAINON
835 TRAIN(J) = TRAINON              'put answer into array
840 NEXT J
850 '
860 FOR J = 0 TO BB
870 TRAINOFF= 0                     'initialize LASER-OFF sum
880 FOR N = 1 TO AA
890 TRAINOFF= TRAINOFF+ (-1)^N*STEPF(N,J)      'adds all previous cycles
900 NEXT N
910 TIME = (BB+J)*MM*TTCDEL*TC*1000 'time in miliseconds
920 PRINT #1,TIME;" ";TRAINOFF      'print time(msec),response
930 LOCATE 18,1 : PRINT TIME,TRAINOFF
935 TRAIN(BB+J) = TRAINOFF          'put answer into array
940 NEXT J
950 PRINT
960 PRINT "Peak to peak amplitude :";TRAIN(BB)-(TRAIN(0)+TRAIN(2*BB))/2
970 END
```

Program TRAIN - continued

```
2000 '-------2000-----SUBROUTINE ERF(Z)--------------------------------
2010 '
2020 IF Z > 2.7 THEN ERF = 1 : GOTO 2160        'close enough
2030 IF Z <-2.7 THEN ERF =-1 : GOTO 2160        'close enough for Rock'n Roll
2040 SUM = Z
2050 N = 1
2060 '
2070 FACT2N = 1
2080 FOR J = 1 TO 2*N+1 STEP 2
2090 FACT2N = FACT2N*J
2100 I = I+1
2110 NEXT J
2120 SUMN = 2^N * Z^(2*N+1) / FACT2N
2130 SUM = SUM + SUMN
2140 IF ABS(SUMN) > .00001 THEN N=N+1 : GOTO 2060
2150 ERF = 1.128379*EXP(-1*(Z^2))*SUM
2160 RETURN
3000 '-----3000------SUBROUTINE HYPER(K)--------------------------------
3010 ER = .0001                                 'convergence tolerance
3020 HYP = 1                                     'initialize sum and sum index
3030 N=1
3040 '
3050 GOTO 3170                                   'N! SUBROUTINE
3060 '
3070 GOTO 3290                                   '(2n-1)!! SUBROUTINE
3080 '
3090 GOTO 3410                                   '(K/2)^2 SUBROUTINE
3100 'calculate sum element OF123 & OF456 are overflow buffers
3110 SUM1 = (-1)^N*FACT2N/FACTN*POW/FACTN/(N+1) 'calculate sum element
3120 OF123 = OF2N1/OFN1*OF2N2/OFN2*OF2N3/OFN3*OFP1/OFN1*OFP2/OFN2-
       *OFP3/OFN3
3130 SUMN = SUM1*OF123
3140 HYP = HYP + SUMN                            'recalculate sum
3150 IF ABS(SUMN) > ER THEN N=N+1 : GOTO 3040   'calculate next element
3160 RETURN                                      'finished
3170 '-------------------N! sub-SUBROUTINE
3180 FACTN = 1                                   'initialize factorial product
3190 OFN1 = 1                                    'initialize overflow buffers
3200 OFN2 = 1
3210 OFN3 = 1
3220 FOR J=1 TO N
3230 FACTN = FACTN*J
3240 IF FACTN > 1.01E+25 THEN FACTN = FACTN*.00001 : OFN1 =
       OFN1*100000!
3250 IF OFN1 > 1.01E+25 THEN OFN1 = OFN1*.00001 : OFN2 = OFN2*100000!
3260 IF OFN2 > 1.01E+25 THEN OFN2 = OFN2*.00001 : OFN3 = OFN3*100000!
3270 NEXT J
3280 GOTO 3060
3290 '---------2N-1!! SUB-SUBROUTINE
3300 FACT2N = 1                                  'initialize factorial product
3310 OF2N1 = 1                                   'initialize overflow buffers
```

Program TRAIN - continued

```
3320 OF2N2 = 1
3330 OF2N3 = 1
3340 FOR J=1 TO 2*N-1 STEP 2
3350 FACT2N = FACT2N*J
3360 IF FACT2N > 1.01E+25 THEN FACT2N=FACT2N*.00001 : OF2N1 =
       OF2N1*100000!
3370 IF OF2N1 > 1.01E+25 THEN OF2N1 = OF2N1*.00001 : OF2N2 =
       OF2N2*100000!
3380 IF OF2N2 > 1.01E+25 THEN OF2N2 = OF2N2*.00001 : OF2N3 =
       OF2N3*100000!
3390 NEXT J
3400 GOTO 3080
3410 '----------(K/2)^N SUB-SUBROUTINE
3420 POW = 1
3430 OFP1 = 1
3440 OFP2 = 1
3450 OFP3 = 1
3460 FOR J=1 TO N
3470 POW = POW*K/2
3480 IF POW > 1.01E+25 THEN POW = POW*.00001 : OFP1 = OFP1*100000!
3490 IF OFP1 > 1.01E+25 THEN OFP1 = OFP1*.00001 : OFP2 = OFP2*100000!
3500 IF OFP2 > 1.01E+25 THEN OFP2 = OFP2*.00001 : OFP3 = OFP3*100000!
3510 NEXT J
3520 GOTO 3100
```

Program MODULAT3

```
10 'PROGRAM MODULAT3
20 '
30 KEY OFF
40 OPEN "\DEV\IEEEOUT" FOR OUTPUT AS #1   'open ieee488 driver files
50 IOCTL #1,"BREAK"
60 PRINT #1,"RESET"
70 OPEN "\DEV\IEEEIN" FOR INPUT AS #2
80 DIM SETK(500)                          'dimension K20 temperature array to be input
90 PRINT CHR$(1
100 PRINT #1,"HELLO"                       'test communication with driver
110 INPUT #2,ID$
120 PRINT "DRIVER TEST": PRINT "----------"
130 PRINT "CONTROLLER   : ";ID$
140 PRINT ""
150 PRINT #1,"OUTPUT K20;TE"               'send command for temperature
160 PRINT #1,"ENTER K20"                   'tell K20 to talk
170 INPUT #2,TEMP$                         'input temperature data
180 PRINT "K20 TEST" : PRINT "--------"
190 PRINT "TEMPERATURE  : ";TEMP$:PRINT "":PRINT ""
200 PRINT "LOCK-IN AMP #1 TEST" : PRINT "-------------------"
210 PRINT #1,"OUTPUT LOCKIN1;HDR0"         'turns the header off for lockin output
220 PRINT #1,"OUTPUT LOCKIN1;?IDX"         'ask lockin for its ID number
230 PRINT #1,"ENTER LOCKIN1"
240 INPUT #2,ID1$
250 PRINT "MODEL NUMBER : ";ID1$
260 PRINT
270 PRINT "LOCK-IN AMP #2 TEST" : PRINT "-------------------"
280 PRINT #1,"OUTPUT LOCKIN2;HDR0"
290 PRINT #1,"OUTPUT LOCKIN2;?IDX"
300 PRINT #1,"ENTER LOCKIN2"
310 INPUT #2,ID2$
320 PRINT "MODEL NUMBER : ";ID2$
330 FOR I = 1 TO 10000                     'delay
340 NEXT I
350 PRINT CHR$(12)
360 PRINT "                 PROGRAM MODULAT3"
370 PRINT "                 ----------------"
380 PRINT ""
390 PRINT "   This program can be used for recording lock-in data (ITHACO 3961)"
400 PRINT "as a function of temperature in a series-type two lockin experiment."
410 PRINT "   The temperature is controlled by the K-20 Temperature Controller"
420 PRINT "One must input the K-20 temperature range and divisions to be used"
430 PRINT "aswell as the name of the output file which can include path."
440 PRINT "A 4 column ASCII file is written which includes in order:"
450 PRINT "temperature (K) and three choices of data from the second lock-in."
460 PRINT "   The address of lockin #1 should be set to 4 and that of lockin #2"
470 PRINT "should be set to 5. The 'X' analog output of lockin #1 should feed"
480 PRINT "the 'A' input of lockin #2. One can also use output 1 of lockin#1"
490 PRINT "when display 1 is set to X to feed EXT DC of lockin#2. Then, one chooses"
500 PRINT "the EXT DC as a data choice from lockin #2,the magnitude of which is"
```

Program MODULAT3 - continued

```
510 PRINT "simply X of lockin #1 amplified by the factor of 10V/Sensitivity #1"
520 PRINT ""
530 INPUT "ENTER TO CONTINUE",G$
540 PRINT CHR$(12)
1000 '-------1000----------------user--input--------------------------------
1010 INPUT "Output data file name : ",FILE$
1020 PRINT ""
1030 PRINT "The maximum # of temperature readings is 500.  Input min and max"
1040 PRINT "temperatures(K) for each temperature range with different divisions"
1050 PRINT ""
1060 I=0 : TMIN = 0 : TMAX = 0 : FT=0          'I is the index of the temperature array
1070 INPUT "Input Tmin : ",TMIN                'input data for temperature range
1075 IF FT=0 THEN TMIN0=TMIN                   'TMIN0 is used for plotting
1080 PRINT ""
1090 IF TMIN<=TMAX THEN PRINT "This is less than or equal to TMAX of the
       previous range"     : PRINT ""                              :
       GOTO 1070
1100 ELSE
1110 INPUT "Input Tmax : ",TMAX
1120 IF TMAX > 350 THEN PRINT "The controller will be damaged for T > 350K!"
       : GOTO 1110
1130 PRINT ""
1140 INPUT "Divisions in K : ",DIV
1150 T = TMIN
1160 SETK(I) = T                               'write data to temperature array
1170 I = I+1                                    'I indexes temperature array
1180 IF I>499 GOTO 1330                         'dimension of T array is 500
1190 T = T+DIV                                  'increment T
1200 IF T <= TMAX GOTO 1160                     'else ask if there is more temperature ranges
1205 IMAX = I-1                                 'maximum index of temperature array
1210 PRINT "":PRINT ""
1220 INPUT "Another temperature range ? (y/n) : ",R$
1230 PRINT ""
1240 IF R$ = "y" OR R$ = "Y" THEN FT=1 : GOTO 1070 'input data for next T range
1250 PRINT "For data aquisition, averaging is done on data which is sampled"
1260 PRINT "from the lock-in at intervals CTIME.  The time allowed for thermal"
1270 PRINT "equilibrium at each temperature step is 2*CTIME."
1280 PRINT "Input CTIME and the number of averages."
1290 PRINT ""
1300 INPUT "CTIME,# of averages (n,m): ",CTIME,NAV
1320 GOTO 1350
1330 PRINT CHR$(12)
1340 PRINT "You have chosen greater than 500 points. SOORRY! TRY AGAIN":END
1350 PRINT CHR$(12)
1360 PRINT "               LOCK-IN INPUT"
1370 PRINT "               -------------"
1380 PRINT ""
1390 PRINT "Set all parameters on the lockin amplifiers now such as :
1400 PRINT ""
1410 PRINT "  SENSITIVITY","TIME CONSTANT",,"Q and FILTER"
1420 PRINT "  AVERAGING ?","SAMPLING"
```

.

Program MODULAT3 - continued

```
1430 PRINT "   TIMES",,"dB/oct." : PRINT ""
1440 PRINT "Three types of data from lockin #2 can be recorded simultaneously."
1450 PRINT "Enter the data codes separated by commas in the column order in"
1460 PRINT "which you would like them to appear in the output ASCII file."
1470 PRINT "The first data chosen will be plotted in real time." :PRINT
1480 PRINT ,"0 :","No data"
1490 PRINT ,"1 :","A Amplitude"
1500 PRINT ,"2 :","A (dB) Amplidude"
1510 PRINT ,"3 :","X (A cosO)"
1520 PRINT ,"4 :","O Phase"
1530 PRINT ,"5 :","Y (A sinO)"
1540 PRINT ,"6 :","ED External DC"
1550 PRINT ,"7 :","RT Ratio"
1560 PRINT ,"8 :","RF Reference Frequency"
1570 PRINT ""
1580 INPUT "Enter your choice of data (d1,d2,d3):",D1$,D2$,D3$
1590 IF VAL(D1$)<0 OR VAL(D1$)>8 OR VAL(D2$)<0 OR VAL(D2$)>8 OR
     VAL(D3$)<0 OR VAL(D3$)>8 THEN PRINT "" : PRINT "TRY AGAIN!" : GOTO
     1580
1600 PRINT CHR$(12)
610 PRINT "ENTER when ready to set controller to base temperature of";SETK(0);"K"
1620 INPUT " ",G$
2000 '----------2000---------------cool down--------------------------------
2010 KEY(1)ON   'enables event trapping with key F1
2020 ON KEY(1) GOSUB 3000                       'start data collection
2030 SK$ = "SK "+STR$(SETK(0))                  'SK$ is command string to K20
2040 PRINT #1,"OUTPUT K20;";SK$                 'send base temp to K20
2050 PRINT #1,"OUTPUT K20;TE"                   'send request for T measurement
2060 PRINT #1,"ENTER K20"                        'ask K20 for result of measurement
2070 INPUT #2,TEMP$                             'input response into program from driver
2080 PRINT #1,"OUTPUT K20;WK"                   'ask K20 for its current 'set' temperature
2090 PRINT #1,"ENTER K20"
2100 INPUT #2,WK$
2110 PRINT CHR$(12)
2120 PRINT "CURRENT TEMPERATURE : ";TEMP$;     'display while cooling
2130 PRINT "" :PRINT ""
2140 PRINT "  BASE TEMPERATURE : ";WK$
2150 PRINT "":PRINT "":PRINT ""
2160 PRINT "F1 to continue !"
2170 FOR T = 1 TO 10000                          '2 second delay loop
2180 NEXT T
2190 GOTO 2050                                   'return for another temperature measurement
3000 '----3000----------display experimental conditions--------------------
3010 PRINT CHR$(12)
3020 PRINT ,"PROGRAM MODULAT3 : EXPERIMENTAL CONDITIONS"
3030 PRINT ,"-------------------------------------------" : PRINT ""
3040 PRINT "Output file : ";FILE$,"Time : ";TIME$,"Date : ";DATE$ :PRINT ""
3050 PRINT #1,"OUTPUT LOCKIN1;?BSS"             'ask for sensitivity
3060 PRINT #1,"ENTER LOCKIN1"
3070 INPUT #2,BSS1$
3080 PRINT #1,"OUTPUT LOCKIN2;?BSS"
```

Program MODULAT3 - continued

```
3090 PRINT #1,"ENTER LOCKIN2"
3100 INPUT #2,BSS2$
3110 PRINT #1,"OUTPUT LOCKIN1;?BTC"        'ask for time constant
3120 PRINT #1,"ENTER LOCKIN1"
3130 INPUT #2,BTC1$
3140 PRINT #1,"OUTPUT LOCKIN2;?BTC"
3150 PRINT #1,"ENTER LOCKIN2"
3160 INPUT #2,BTC2$
3170 PRINT #1,"OUTPUT LOCKIN1;?AVM"        'ask for averaging mode
3180 PRINT #1,"ENTER LOCKIN1"
3190 INPUT #2,AVM1$
3200 PRINT #1,"OUTPUT LOCKIN2;?AVM"
3210 PRINT #1,"ENTER LOCKIN2"
3220 INPUT #2,AVM2$
3230 PRINT #1,"OUTPUT LOCKIN1;?AVT"        'ask for averaging TIMES
3240 PRINT #1,"ENTER LOCKIN1"
3250 INPUT #2,AVT1$
3260 PRINT #1,"OUTPUT LOCKIN2;?AVT"
3270 PRINT #1,"ENTER LOCKIN2"
3280 INPUT #2,AVT2$
3290 PRINT #1,"OUTPUT LOCKIN1;?SSA"        'ask for digital and sampling interval
3300 PRINT #1,"ENTER LOCKIN1"
3310 INPUT #2,SSA1$,SSA2$
3320 PRINT #1,"OUTPUT LOCKIN2;?SSA"
3330 PRINT #1,"ENTER LOCKIN2"
3340 INPUT #2,SSA3$,SSA4$
3350 PRINT #1,"OUTPUT LOCKIN1;ODS8000"     'set data select for frequency output
3360 PRINT #1,"OUTPUT LOCKIN1;?ODT"        'ask for data
3370 PRINT #1,"ENTER LOCKIN1"
3380 INPUT #2,FREQ1$,SHIT$,SHIT$           'pay attention just to frequency data
3390 PRINT #1,"OUTPUT LOCKIN2;ODS8000"
3400 PRINT #1,"OUTPUT LOCKIN2;?ODT"
3410 PRINT #1,"ENTER LOCKIN2"
3420 INPUT #2,FREQ2$,SHIT$,SHIT$
3430 '              now set data select for chosen experimental data
3440 PRINT #1,"OUTPUT LOCKIN2;ODS"+D1$+D2$+D3$'tell lockin of data se    tion
3450 '
3460 PRINT #1,"OUTPUT LOCKIN2;?ODS"        'ask for output data select
3470 PRINT #1,"ENTER LOCKIN2"
3480 INPUT #2,ODS2$
3490 PRINT CHR$(12)
3500 PRINT ,"PROGRAM MODULAT3 : EXPERIMENTAL CONDITIONS"
3510 PRINT ,"------------------------------------------"
3520 PRINT "Output file : ";FILE$,"Time : ";TIME$,"Date : ";DATE$ :PRINT ""
3530 PRINT ,"    LOCK-IN # 1" : PRINT ,"    -----------"
3540 PRINT "Sensitivity  : ";BSS1$,"Time Constant    : ";BTC1$        'display values
3550 PRINT "Sampling Intv.: ";SSA2$,"Output 2^n    : ";SSA1$
3560 PRINT "Averaging    : ";AVM1$,"Times      : ";AVT1$
3570 PRINT ,"    LOCK-IN # 2" : PRINT ,"    -----------"
3580 PRINT "Sensitivity  : ";BSS2$,"Time Constant    : ";BTC2$
3590 PRINT "Sampling Intv.: ";SSA4$,"Output 2^n    : ";SSA3$
```

Program MODULAT3 - continued

```
3600 PRINT "Averaging    : ";AVM2$,"Times          : ";AVT2$ :PRINT
3610 PRINT "K-20 Temp Range  : ";SETK(0);" to ";SETK(IMAX);"K"
3620 PRINT "# of Averages    : ";NAV;" sec","Cycle time        : ";CTIME;"sec"
3630 PRINT "Carrier Frequency  : ";FREQ1$;" Hz","Modulation Frequency: ";FREQ2$;"
     Hz"
3640 PRINT "Output Data Select : ";ODS2$
3650 INPUT "Sample current (mA) : ",ISAMP :PRINT ""
3660 INPUT "Comments : ",G$ : PRINT ""
3670 INPUT "Are the Temp range and averaging parameters OK?(y/n) :",Y$ :PRINT ""
3680 IF Y$ = "n" OR Y$ = "N" THEN PRINT CHR$(12) : GOTO 1000
3690 INPUT "Are the lock-in parameters OK ? (y/n) :",Y$ : PRINT ""
3700 IF Y$ = "N" OR Y$ = "n" THEN PRINT "Go to LOCAL on the lock-in front panel,
     change the necessary parameters and" : INPUT "ENTER",SHIT$ : GOTO 3000
3710 LPRINT ,"PROGRAM MODULAT3 : EXPERIMENTAL CONDITIONS" 'printer
3720 LPRINT ,"------------------------------------------"
3730 LPRINT "Output file : ";FILE$,"Time : ";TIME$;"   Date : ";DATE$:LPRINT ""
3740 LPRINT ,"    LOCK-IN # 1" : LPRINT ,"    -----------"
3750 LPRINT "Sensitivity  : ";BSS1$,"Time Constant    : ";BTC1$        'display vals
3760 LPRINT "Sampling Intv.: ";SSA2$,"Output 2^n      : ";SSA1$
3770 LPRINT "Averaging    : ";AVM1$,"Times          : ";AVT1$ :LPRINT ""
3780 LPRINT ,"    LOCK-IN # 2" : LPRINT ,"    -----------"
3790 LPRINT "Sensitivity  : ";BSS2$,"Time Constant    : ";BTC2$
3800 LPRINT "Sampling Intv.: ";SSA4$,"Output 2^n      : ";SSA3$
3810 LPRINT "Averaging    : ";AVM2$,"Times          : ";AVT2$ :LPRINT ""
3820 LPRINT "K-20 Temp Range   : ";SETK(0);" to ";SETK(IMAX);"K"
3830 LPRINT "# of Averages    : ";NAV;" sec","Cycle Time        : ";CTIME;" sec"
3840 LPRINT "Carrier Frequency  : ";FREQ1$;" Hz","Modulation Frequency:
     ";FREQ2$;" Hz"
3850 LPRINT "Output Data Select : ";ODS2$
3860 LPRINT "Sample current (mA) : ";ISAMP : LPRINT ""
3870 LPRINT "Comments : ",G$ : LPRINT "" :LPRINT
3880 PRINT CHR$(12)
3890 INPUT "Input full scale voltage (or phase) for plotting : ",FULLSC
3900 PRINT
3910 INPUT "Enter to start collecting data! ",G$
4000 '---------4000-------draw plot-----------------------------------------
4010 KEY OFF                                    'make room for plotting
4020 SCREEN 2                                    'enter graphics mode 640*200
4030 DELTEMP = TMAX - TMIN0
4040 WY0 = -.3266667*FULLSC                      'set up coordinates for plotting
4050 WY1 = FULLSC
4060 WX0 = TMIN0 - .05*DELTEMP
4070 WX1 = TMAX + 5.172414E-02*DELTEMP
4080 DRAW "BM29,0NL5D30NL5D30NL5D30NL5D30NL5D30NL5" 'draw left side
     axis with ticks
4090 DRAW
     "ND4R58ND2R58ND4R58ND2R58ND4R58ND2R58ND4R58ND2R58ND4R58N
     D2R58ND4"'bottom axis
4100 DRAW "U150L580"                             'right and top axis line
4110 DRAW "BM29,173R120D12L120U12"               'temperature box
4120 DRAW "BM490,173R120D12L120U12"              'power box
```

Program MODULAT3 - continued

```
4130 LOCATE 21,2 : PRINT TMIN0
4140 LOCATE 21,17 : PRINT TMIN0 + DELTEMP/5
4150 LOCATE 21,31 : PRINT TMIN0 + 2*DELTEMP/5
4160 LOCATE 21,46 : PRINT TMIN0 + 3*DELTEMP/5
4170 LOCATE 21,60 : PRINT TMIN0 + 4*DELTEMP/5
4180 LOCATE 21,75 : PRINT TMAX
4190 LOCATE 23,34 : PRINT "TEMPERATURE (K)"
4200 LOCATE 1,1 : PRINT "FS."
4205 LOCATE 19,1 : PRINT "0"
4210 LOCATE 23,6:PRINT "T =":LOCATE 23,64:PRINT "P =":LOCATE 2,6:PRINT
     "D1 ="
4220 WINDOW (WX0,WY0)-(WX1,WY1)          'define window for plotting
5000 '------------5000-------data collection----------------------------
5010 IN = 0 : N = 0 'zero index for temperature array and averaging
5020 D1SUM = 0 : D2SUM = 0 : D3SUM = 0     'initialize sums to 0
5030 OPEN "O",#3,FILE$
5040 TIMER ON
5050 ON TIMER(CTIME) GOSUB 5080           'CTIME is the sampling time
5060 '
5070 GOTO 5060                             'infinite loop
5080 IF N<>0 OR IN=0 THEN 5095     'else determine length of equilibrium cycle
5085 DELSET = SETK(IN)-SETK(IN-1)
5090 IF DELSET>CTIME THEN TIMER OFF : FOR J=1 TO DELSET*5600 : NEXT J :
     TIMER ON
5095 IF N=0 THEN N=N+1 : RETURN
5100 PRINT #1,"OUTPUT K20;TE"            'first check if temperature is OK
5110 PRINT #1,"ENTER K20"
5120 INPUT #2,TEMP$
5130 IF (VAL(TEMP$) - SETK(IN)) > 1! GOTO 6000     'exit for temperature check
5140 PRINT #1,"OUTPUT K20;PO"             'ask for power
5150 PRINT #1,"ENTER K20"
5160 INPUT #2,POW$
5170 LOCATE 23,11:PRINT TEMP$:LOCATE 23,69:PRINT POW$'screen print T and P
5180 IF F = 1 THEN RETURN          'data collection is finished; monitoring mode
5190 PRINT #1,"OUTPUT LOCKIN2;?ODT"      'ask lockin for data
5200 PRINT #1,"ENTER LOCKIN2"             'tell lockin to send data
5210 INPUT #2,DS1,DS2,DS3,SHIT,SHIT      'input chosen data,ignore display data
5220 D1SUM = D1SUM + DS1                  'sums for lockin data
5230 D2SUM = D2SUM + DS2
5240 D3SUM = D3SUM + DS3
5250 LOCATE 2,11 : PRINT DS1              'screen print newest value of data 1
5260 IF N<NAV THEN N=N+1 : RETURN        'averaging has not finished so return
5270 DATA1 = D1SUM/NAV                    'averages for lockin data
5280 DATA2 = D2SUM/NAV
5290 DATA3 = D3SUM/NAV
5300 PRINT #3,SETK(IN);" ";DATA1;" ";DATA2;" ";DATA3       'print to file
5310 PRESET (SETK(IN),DATA1),1            'plot data point
5320 N = 0                                'reset averaging index to 0
5330 D1SUM = 0 : D2SUM = 0 : D3SUM = 0    'initialize sums to 0 for next point
5340 'next if max temp is not reached,increase temperature and return
```

Program MODULAT3 - continued

```
5350 IF IN<IMAX THEN IN=IN+1:SK$="SK"+STR$(SETK(IN)):PRINT
     #1,"OUTPUT K20;";SK$ :RETURN
5360 CLOSE #3   'close data file
5370 LOCATE 2,6 : PRINT "FINISHED ! " : KEY ON
5380 F = 1 : N = 1         'set flags so that continuous T monitoring can be done
5390 RETURN
6000 '--------6000-----------------blockage check----------------------------
6010 FOR L = 1 TO 3        'check temp 3 times before shutting down
6020 PRINT #1,"OUTPUT K20;TE"
6030 PRINT #1,"ENTER K20"
6040 INPUT #2,TEMP$
6050 IF (VAL(TEMP$) - SETK(IN)) < 1! GOTO 6000      'temp is OK, so return
6060   FOR M = 1 TO 2000                        '1 sec delay
6070   NEXT M
6080 BEEP
6090 NEXT L
6100                'capillaries must be blocked or gas has run out--SHUT DOWN
6110 SCREEN 0                                'return to text mode
6120 PRINT #1,"OUTPUT K20;SK 325"   'increase to room temp to thaw capillaries
6130 PRINT "":PRINT "":PRINT "":PRINT ""
6140 PRINT ,"   PLEASE   SHUT   OFF   THE   GAS !!"
6150 PRINT "":PRINT "":PRINT "":PRINT "":PRINT ""
6160 PRINT ,"Use   Ctrl-Break   to   stop   that   awful   noise"
6170 CLOSE                                'close all open files
6180 SOUND RND*1000+37,1                  'continuous noise
6190 GOTO 6180
```

Program SBSCAN

```
10 SCREEN 0,0,0
20 'PROGRAM SBSCAN
30 '
40 KEY OFF
50 OPEN "\DEV\IEEEOUT" FOR OUTPUT AS #1    'open ieee488 driver files
60 IOCTL #1,"BREAK"
70 PRINT #1,"RESET"
80 OPEN "\DEV\IEEEIN" FOR INPUT AS #2
90 PRINT CHR$(12)
100 PRINT ,,"DEVICE COMMUNICATION TESTS" : PRINT ,,"-------------------------"
110 PRINT "DRIVER TEST": PRINT "-----------"
120 PRINT #1,"HELLO"                        'test communication with driver
130 INPUT #2,ID$
140 PRINT "Controller   : ";ID$
150 PRINT #1,"TIME OUT 10"                  'set 5 sec delay for timeout error
160 PRINT
170 PRINT "NEWPORT 855C TEST" : PRINT "----------------"
180 PRINT #1,"OUTPUT N855;Q2"               'specify IEEE communications to 855
190 PRINT #1,"ENTER N855"                   'if thats OK with you?
200 INPUT #2,R1$
210 PRINT #1,"ENTER N855"
220 INPUT #2,R2$
230 PRINT #1,"ENTER N855"
240 INPUT #2,R3$
250 PRINT #1,"OUTPUT N855;!"                specify echo supress for 855C
260 PRINT #1,"ENTER N855"
270 INPUT #2,R$
280 PRINT #1,"OUTPUT N855;.1"               'query for drive 1 status
290 PRINT #1,"OUTPUT N855;.2"               'query for drive 2 status
30C PRINT #1,"ENTER N855"
310 INPUT #2,D1$
320 PRINT #1,"ENTER N855"
330 INPUT #2,D2$
340 PRINT R2$;" ";R3$," Drive #1: ";D1$;" Drive #2: ";D2$
350 PRINT
360 PRINT "K20 TEST" : PRINT "--------"
370 PRINT #1,"OUTPUT K20;TE"                'ask for current temperature
380 PRINT #1,"ENTER K20"
390 INPUT #2,T$
400 PRINT "Refridgerator temperature : ";T$
410 PRINT
420 PRINT "LOCK-IN AMP #1 TEST" : PRINT "-----------------"
430 PRINT #1,"OUTPUT LOCKIN1;HDR0"          'turns off header for input
440 PRINT #1,"OUTPUT LOCKIN1;?IDX"          'ask for model identification
450 PRINT #1,"ENTER LOCKIN1"
460 INPUT #2,ID$
470 PRINT "Model # : ";ID$
480 PRINT #1,"OUTPUT LOCKIN1;DFI1"          'set panel 1 for A
490 PRINT #1,"OUTPUT LOCKIN1;SBP1"          'turn error beeper on
500 PRINT #1,"OUTPUT LOCKIN1;SSA0,2"        '300 ms measurement interval
```

Program SBSCAN - continued

```
510 PRINT
520 FOR I = 1 TO 15000                                  'time loop
530 NEXT I
540 PRINT #1,"TIME OUT 50"                              'set 50 sec delay for timeout error
550 PRINT CHR$(12)
560 PRINT ,,"User Input"
570 PRINT ,,"----------"
580 PRINT
590 INPUT "Output file          : ",FILE$
600 PRINT
610 INPUT "Temperature (0-350K)      : ",TEMP
620 IF TEMP>350 OR TEMP<0 THEN 610
630 PRINT
640 INPUT "Seconds/scan point (integer) : ",TIME
650 IF (INT(TIME)-TIME) <>0 THEN 640
660 PRINT
670 INPUT "Scan Velocity (0-4000um/sec) : ",V1
680 IF V1>4000 OR V1<0 THEN 670
690 PRINT
700 INPUT "X x Y Scan size (n,m)     : ",NPIX,MPIX
710 PIXEL=TIME*V1                                       'pixel size in um
715 RETRIEVE = INT(NPIX*PIXEL/400 +10)                  'time for laser line return
720 YPIXEL = PIXEL                                      'for square pixels
730 V1$ =MID$(STR$(V1*10),2)                            'spaceless string for 855
740 DIST$=MID$(STR$(10*PIXEL*NPIX),2)                   'in .1um units
741 F1$ = ".4"                                          'fast mode return velocity
742 IF VAL(DIST$)<5000 THEN F1$ = ".1"                  'reduce fast mode return velocity
743 IF VAL(DIST$)<2000 THEN F1$ = ".04"                 'reduce fast mode return vel. more
750 YSTEP$=MID$(STR$(YPIXEL*10),2)                       'spaceless string for 855
760 PRINT
770 INPUT "Square Pixels (y/n) ?     : ",Y$
780 PRINT
790 IF Y$="y" OR Y$="Y" THEN 820                        'skip ahead
800 PRINT "X-Pixel :";PIXEL;"(um)";                     'else input y-pixel size
810 INPUT "  Y-Pixel ? : ",YPIXEL
820 YSTEP$=MID$(STR$(YPIXEL*10),2)                       'spaceless string for 855
1000 '----------1000----------CoooooL-Dooowwnn--------------------------
1010 SCREEN 9                                           'enter graphics mode for plotting
1020 KEY OFF
1030 WY0 = -.25*350                                     'set up window coordinates
1040 WY1 = 350
1050 WX0 = -.146296*1200
1060 WX1 = 1.037037*1200
1070 DRAW"BM79,0NL4D40NL8D40NL4D40NL8D40NL4D40NL8D40NL4D40NL8"
1080 DRAW"ND10R27ND5R27ND5R27ND5R27ND5R27ND10R27ND5R27ND5R27-
     ND5R27ND5R27ND10R27ND5R27ND5R27ND5R27ND5R27ND10R27ND5R27
     ND5R27ND5R27ND5R27ND10"                            'bottom axis
1090 DRAW "U280L540"                                    'side and top axis
1100 LOCATE 3,5 : PRINT "300"
1110 LOCATE 9,5 : PRINT "200"
1120 LOCATE 15,5 : PRINT "100"
```

Program SBSCAN - continued

```
1130 LOCATE 20,5 : PRINT "  0"
1140 LOCATE 22,10 : PRINT "0"
1150 LOCATE 22,27 : PRINT "5"
1160 LOCATE 22,44 : PRINT "10"
1170 LOCATE 22,60 : PRINT "15"
1180 LOCATE 22,77 : PRINT "20"
1190 LOCATE 23,37 : PRINT "Time (minutes)"
1200 LOCATE 12,1  : PRINT "Temp (K)"
1210 LOCATE 2,65 : PRINT "T ="
1220 LOCATE 4,65 : PRINT "P ="
1230 LOCATE 6,63 : PRINT "F1 to continue!"
1240 DRAW "BM500,10D22R110U22L110"        'box for temperature display
1250 DRAW "BM500,38D22R110U22L110"        'box for power display
1260 WINDOW (WX0,WY0)-(WX1,WY1)           'define plotting window
1270 KEY(1)ON                             'enables event trap with F1
1280 ON KEY(1) GOSUB 1480                 'exit cool down
1290 SEC=0                                 'time index in seconds
1300 TIMER ON                             'enables event trap with clock
1310 ON TIMER(2) GOSUB 1350               'goto temp collect every 2 sec
1320 PRINT #1,"OUTPUT K20;SK"+STR$(TEMP)      'set base temperature on K20
1330 '                                    'dummy line
1340 GOTO 1330                            'infinite loop, wait for traps!
1350 'SUBROUTINE TEMPERATURE COLLECT
1360 SEC = SEC + 2                        'add 2 seconds to time
1370 PRINT #1,"OUTPUT K20;TE"             'ask for temperature
1380 PRINT #1,"ENTER K20"
1390 INPUT #2,T$
1400 PRINT #1,"OUTPUT K20;PO"             'ask for power
1410 PRINT #1,"ENTER K20"
1420 INPUT #2,P$
1430 LOCATE 2,69 : PRINT T$               'display temperature
1440 LOCATE 4,69 : PRINT P$               'display Power
1450 PRESET (SEC,VAL(T$)),7               'plot temp vs time
1460 IF SEC>1200 THEN TIMER OFF : RETURN 1000   'do another 20 min plot
1470 RETURN
1480 TIMER OFF                            'stop temperature measurement
1490 SCREEN 0                             'return to normal graphics
1500 INPUT "Change Temperature (Y/N) ? : ",Y$
1510 IF Y$<>"Y" AND Y$<>"y" THEN 1560     'go ahead
1520 PRINT
1530 INPUT "Temperature (0-350K)    :",TEMP    'input new temp
1540 PRINT
1550 RETURN 1000                          'go back to graphics monitor T and P change
1560 '                                    'finished temperature cool down
2000 '----------2000----------LOCK-IN INPUT--------------------------------
2010 PRINT CHR$(12)
2020 PRINT ,,"LOCK-IN INPUT"
2030 PRINT ,,"-------------"
2040 PRINT
2050 PRINT "Set all parameters on the lockin amplifier now such as :
2060 PRINT ""
```

Program SBSCAN - continued

```
2070 PRINT "   SENSITIVITY","TIME CONSTANT",,"Q and FILTER"
2080 PRINT "   AVERAGING ?","SAMPLING"
2090 PRINT "   TIMES",,"dB/oct." : PRINT
2100 PRINT "Three types of data from the lockin can be recorded simultaneously."
2110 PRINT "Enter the data codes separated by commas in the column order in"
2120 PRINT "which you would like them to appear in the output ASCII file."
2130 PRINT
2140 PRINT ,"1 :","A Amplitude"
2150 PRINT ,"2 :","A (dB) Amplidude"
2160 PRINT ,"3 :","X (A cosO)"
2170 PRINT ,"4 :","O Phase"
2180 PRINT ,"5 :","Y (A sinO)"
2190 PRINT ,"6 :","ED External DC"
2200 PRINT ,"7 :","RT Ratio"
2210 PRINT ,"8 :","RF Reference Frequency"
2220 PRINT
2230 INPUT "Enter your choice of data (d1,d2,d3):",D1,D2,D3
2240 IF D1<1 OR D1>8 OR D2<1 OR D2>8 OR D3<1 OR D3>8 THEN 2230
2250 CHECK(1)=D1 : CHECK(2)=D2 : CHECK(3)=D3'used for checking data selections
2260 FOR I=1 TO 3
2270 IF CHECK(I)=1 THEN SIG$(I)=" AMP "
2280 IF CHECK(I)=2 THEN SIG$(I)="AMPdB"
2290 IF CHECK(I)=3 THEN SIG$(I)="  X  "
2300 IF CHECK(I)=4 THEN SIG$(I)="PHASE"
2310 IF CHECK(I)=5 THEN SIG$(I)="  Y  "
2320 IF CHECK(I)=6 THEN SIG$(I)="EXTDC"
2330 IF CHECK(I)=7 THEN SIG$(I)="RATIO"
2340 IF CHECK(I)=8 THEN SIG$(I)="REF F"
2350 NEXT I
3000 '----3000-----------DISPLAY EXPERIMENTAL CONDITIONS--------------------
3010 PRINT CHR$(12)
3020 PRINT ,"PROGRAM MODULAT3 : EXPERIMENTAL CONDITIONS"
3030 PRINT ,"------------------------------------------"
3040 PRINT
3050 PRINT "Output file : ";FILE$,"Time : ";TIME$,"Date : ";DATE$:PRINT
3060 PRINT #1,"OUTPUT LOCKIN1;?BSS"      'ask for sensitivity
3070 PRINT #1,"ENTER LOCKIN1"
3080 INPUT #2,BSS1$
3090 PRINT #1,"OUTPUT LOCKIN1;?BTC"      'ask for time constant
3100 PRINT #1,"ENTER LOCKIN1"
3110 INPUT #2,BTC1$
3120 PRINT #1,"OUTPUT LOCKIN1;?AVM"      'ask for averaging mode
3130 PRINT #1,"ENTER LOCKIN1"
3140 INPUT #2,AVM1$
3150 PRINT #1,"OUTPUT LOCKIN1;?AVT"      'ask for averaging TIMES
3160 PRINT #1,"ENTER LOCKIN1"
3170 INPUT #2,AVT1$
3180 PRINT #1,"OUTPUT LOCKIN1;?SSA"      'ask for digital and sampling interval
3190 PRINT #1,"ENTER LOCKIN1"
3200 INPUT #2,SSA1$,SSA2$
3210 PRINT #1,"OUTPUT LOCKIN1;ODS8000"   'set data select for frequency output
```

Program SBSCAN - continued

```
3220 PRINT #1,"OUTPUT LOCKIN1;?ODT"        'ask for data
3230 PRINT #1,"ENTER LOCKIN1"
3240 INPUT #2,FREQ1$,SHIT$,SHIT$                'pay attention just to frequency data
3250 PRINT #1,"OUTPUT LOCKIN1;ODS"+STR$(D1)+STR$(D2)+STR$(D3) 'ODS
       command
3260 PRINT #1,"OUTPUT LOCKIN1;?ODS"       'ask for output data select
3270 PRINT #1,"ENTER LOCKIN1"
3280 INPUT #2,ODS1$
3290 PRINT CHR$(12)
3300 PRINT ,"PROGRAM SBSCAN : EXPERIMENTAL CONDITIONS"
3310 PRINT ,"----------------------------------------"
3320 PRINT "Output file : ";FILE$,"Time : ";TIME$,"Date : ";DATE$
3330 PRINT ,,"      LOCK-IN # 1" : PRINT ,," -----------"
3340 PRINT "Sensitivity  : ";BSS1$,"Time Constant     : ";BTC1$'display values
3350 PRINT "Sampling Intv.: ";SSA2$,"Output 2^n      : ";SSA1$
3360 PRINT "Averaging    : ";AVM1$,"Times           : ";AVT1$
3370 PRINT "Sideband Freq : ";FREQ1$;" Hz";
3380 INPUT " Modulation Freq    : ",FREQ2$
3390 PRINT "Output Data Select : ";ODS1$
3400 PRINT "Temperature       : ";TEMP;" K"
3410 INPUT "Sample current (mA) :  ",ISAMP
3420 PRINT "Scan Velocity :";V1;"um/sec","Seconds/point     : ";TIME
3430 PRINT "Scan Size  :";NPIX*PIXEL;"x";MPIX*YPIXEL;"um",
3440 PRINT "Data Size  :";NPIX+1;"x";MPIX+1
3450 PRINT "Pixel Size :";PIXEL;"x";YPIXEL;"um"
3460 INPUT "Comments : ",G$ : PRINT
3470 INPUT "Are the lock-in parameters OK ? (y/n) :",Y$ : PRINT
3480 IF Y$ = "N" OR Y$ = "n" THEN PRINT "Go to LOCAL on the lock-in front panel,
       change the necessary parameters and" : INPUT "ENTER",SHIT$ : GOTO 3000
3490 LPRINT ,"PROGRAM SBSCAN : EXPERIMENTAL CONDITIONS"
3500 LPRINT ,"----------------------------------------"
3510 LPRINT "Output file : ";FILE$,"Time : ";TIME$;"  Date : ";DATE$
3520 LPRINT ,,"      LOCK-IN # 1" : LPRINT ,," -----------"
3530 LPRINT "Sensitivity  : ";BSS1$,"Time Constant     : ";BTC1$
3540 LPRINT "Sampling Intv.: ";SSA2$,"Output 2^n      : ";SSA1$
3550 LPRINT "Averaging    : ";AVM1$,"Times           : ";AVT1$
3560 LPRINT "Sideband Freq : ";FREQ1$;" Hz","Modulation Freq    : ";FREQ2$
3570 LPRINT "Output Data Select : ";ODS1$
3580 LPRINT "Temperature       : ";TEMP;" K"
3590 LPRINT "Sample current (mA) :  ";ISAMP
3600 LPRINT "Scan Velocity :";V1;"um/sec","Seconds/point     : ";TIME
3610 LPRINT "Scan Size  :";NPIX*PIXEL;"x";MPIX*YPIXEL;"um",
3620 LPRINT "Data Size  :";NPIX+1;"x";MPIX+1
3630 LPRINT "Pixel Size :";PIXEL;"x";YPIXEL;"um"
3640 LPRINT "Comments : ",G$
3650 LPRINT
3660 PRINT CHR$(12)
3670 PRINT:PRINT:PRINT:PRINT:PRINT:PRINT
3680 INPUT "            ENTER TO START SCAN !!",G$
5000 '-----------5000------SCAN-------------------------------------------
5010 OPEN "O",3,FILE$                         'open data file for output
```

Program SBSCAN - continued

```
5020 PRINT #1,"OUTPUT N855;V2.4"            'set velocity 2
5030 PRINT #1,"OUTPUT N855;V1"+V1$          'set velocity 1
5040 PRINT #1,"OUTPUT N855;S2"+YSTEP$       'set step size 2
5050 PRINT #1,"OUTPUT N855;B1.0128"         'set backlash for drive1
5060 PRINT #1,"OUTPUT N855;B2.0128"         'set backlash for drive2
5070 ' displays
5080 SCREEN 9
5090 KEY OFF
5100 PRINT ,,"LASER SCAN IN PROGRESS !"
5110 PRINT:PRINT:PRINT:PRINT:PRINT:PRINT
5120 PRINT ,"        Current Coordinates (um)"
5130 PRINT
5140 PRINT ,,"X =","Y ="
5150 PRINT:PRINT
5160 PRINT ,,"     Signals"
5170 PRINT
5180 PRINT ,,SIG$(1);" = "                  'data 1 display title
5190 PRINT
5200 PRINT ,,SIG$(2);" = "                  'data 2 display title
5210 PRINT
5220 PRINT ,,SIG$(3);" = "                  'data 3 display title
5230 DRAW "C1BM210,15R210"                  'fancy title underline
5240 DRAW "C4BM210,20R210"
5250 DRAW "C5BM210,25R210"
5260 DRAW "C8BM210,30R210"
5270 DRAW "C6BM210,35R210"
5280 DRAW "C2BM210,40R210"
5290 DRAW "C3BM210,45R210"
5300 DRAW "C7BM210,50R210"
5310 DRAW "BM215,115R200"                   'coordinate underline
5320 DRAW "BM275,185R80"                     'signal underline
5330 LOCATE 2,65 : PRINT "T ="
5340 LOCATE 4,65 : PRINT "P ="
5350 DRAW "BM500,10D22R110U22L110"          'box for temperature display
5360 DRAW "BM500,4rD22R110U22L110"          'box for power display
5370 FOR M=0 TO MPIX                         'm is line index (y-axis)
5380 N=0                                     'initialize x-axis index
5390 PRINT #1,"OUTPUT LOCKIN1;?ODT"         'ask for n=0(x=0) data points
5400 PRINT #1,"ENTER LOCKIN1"
5410 INPUT #2,D1,D2,D3,G,G                   'input 3 of 5 pieces of data
5420 PRINT #3,N*PIXEL;" ";M*YPIXEL;" ";D1;" ";D2;" ";D3    'write to file
5430 LOCATE 10,33 : PRINT N*PIXEL           'print coordinates to screen
5440 LOCATE 10,47 : PRINT M*YPIXEL
5450 LOCATE 15,37 : PRINT D1                 'print data to screen
5460 LOCATE 17,37 : PRINT D2
5470 LOCATE 19,37 : PRINT D3
5480 TIMER ON
5485 ON ERROR GOTO 7000                      'Basic (I/O) error trapping
5490 ON TIMER(TIME) GOSUB 6080              'go to data collect every time
5500 'Next; send all commands to buffer of 855 sequentially to be excecuted
5510 'at its own pace. Timer command and move command are almost simultaneous.
```

Program SBSCAN - continued

```
5520 PRINT #1,"OUTPUT N855;M1"+DIST$        'move 1
5530 PRINT #1,"OUTPUT N855;W1"              'wait for 1 to finish
5540 PRINT #1,"OUTPUT N855;V1"+F1$          'set vel 1 to fast mode
5550 PRINT #1,"OUTPUT N855;I2"              'increment 2
5560 PRINT #1,"OUTPUT N855;H1"              'home 1
5570 '                                      'dummy line
5580 IF N=NPIX THEN 5600                    'line finished-get out of loop
5590 GOTO 5570                              'infinite loop to wait for time signal
5600 TIMER OFF                              'stop collecting data
5610 PRINT #1,"OUTPUT K20;TE"               'temperature check
5620 PRINT #1,"ENTER K20"
5630 INPUT #2,T$
5640 IF (VAL(T$)-TEMP)>1 THEN GOSUB 6200    'exit to blockage routine
5650 PRINT #1,"OUTPUT K20;PO"               'power measurement
5660 PRINT #1,"ENTER K20"
5670 INPUT #2,P$
5680 LOCATE 2,69 : PRINT T$                 'display temperature
5690 LOCATE 4,69 : PRINT P$                 'display power
5700 T0=TIMER
5710 T1=TIMER
5720 IF (T1-T0)<RETRIEVE THEN 5710
5730 PRINT #1,"OUTPUT N855;C1"              'ask for current position of 1
5740 PRINT #1,"ENTER N855"                  'input data
5750 INPUT #2,R$
5760 IF ABS(VAL(R$))<.0003 THEN 5810
5770 LPRINT "SLOW AT M = ";M;"C1 = ";R$;TIME$      'motor 1 has not got back yet
5775 PRINT #1,"OUTPUT N855;H1"              'tell it to get home again!
5780 FOR I=1 TO 25000!
5790 NEXT I
5800 GOTO 5730                              'try again. is it back yet?
5810 BEEP                                   'all is OK
5820 PRINT #1,"OUTPUT N855;V1"+V1$          'set velocity 1 to slow again
5830 FOR I=1 TO 1000                        'time loop for equilibration
5840 NEXT I
5850 NEXT M
6000 '--6000---------------------SCAN FINISHED---------------------------
6010 PRINT                    'Scan is finished!!!!!
6020 PRINT #1,"OUTPUT N855;H2"              'bring home y-axis
6030 SCREEN 0                               'return to normal graphics
6040 PRINT "Finished !"
6050 KEY ON
6060 PRINT #1,"TIME OUT 10"                 'reset timeout error, 10 sec
6070 END                                    'goodnight Irene!
6080 '                        --COLLECTION SUBROUTINE--
6090 N=N+1
6100 PRINT #1,"OUTPUT LOCKIN1;?ODT"         'ask for data points
6110 PRINT #1,"ENTER LOCKIN1"
6120 INPUT #2,D1,D2,D3,G,G                  'input 3 of 5 pieces of data
6130 PRINT #3,N*PIXEL;" ";M*YPIXEL;" ";D1;" ";D2;" ";D3     'write to file
6140 LOCATE 10,33 : PRINT N*PIXEL           'print coordinates to screen
6150 LOCATE 10,47 : PRINT M*YPIXEL
```

Program SBSCAN - continued

```
6160 LOCATE 15,37 : PRINT D1
6170 LOCATE 17,37 : PRINT D2
6180 LOCATE 19,37 : PRINT D3
6190 RETURN
6200 LOCATE 6,64 : PRINT "  BLOCKAGE!  "
6210 LOCATE 8,64 : PRINT "Turn off gas!"
6220 LOCATE 10,64 : PRINT " F1 to stop  "
6230 LOCATE 11,64 : PRINT " the noise!  "
6240 KEY(1)ON
6250 ON KEY(1) GOSUB 6300
6260 PRINT #1,"OUTPUT K20;SK 325"            'increase temp to thaw capillaries
6270 LOCATE 2,69 : PRINT " 325 K  "
6280 SOUND RND*1000+37,1                     'annoying noise
6290 GOTO 6280
6300 LOCATE 13,64 : PRINT " THANK-YOU!  "
6310 RETURN 6320                             'required return for event trap
6320 FOR I = 1 TO 60000!
6330 NEXT I
6340 LOCATE 15,62 : PRINT "ENTER to resume"
6350 LOCATE 16,62 : INPUT "cooling",G$
6360 LOCATE 18,62 : INPUT "SK TEMP?",G$
6370 PRINT #1,"OUTPUT K20;SK"+STR$(TEMP)      'resume cooling
6380 LOCATE 20,62 : PRINT "ENTER to resume"
6390 LOCATE 21,62 : INPUT "program",G$
6400 RETURN 5610                             'return from GOSUB 6000
7000 ER=ERR : EL=ERL                         'type of error and line #
7010 LPRINT "ERROR ";ER;" AT LINE ";EL;" ";TIME$
```